

Cross section measurements of neutron-induced reactions on ^{12}C
using a diamond detector

By
Andrew Wantz

A DISSERTATION

Submitted to
Michigan State University
in partial fulfillment of the requirements
for the degree of
Physics - Doctor of Philosophy
2025

July 1, 2025

Abstract

Background: Single-crystal chemical vapor deposited (sCVD) diamond detectors offer a unique method to study cross sections of reactions on carbon since they can be used as active targets. Previous studies analyzing neutrons on carbon using these detectors were primarily focused on lower energy neutrons and reactions, and some of these did not have sufficient energy resolution to isolate the contributions of reaction channels with similar Q values.

Purpose: This work extends neutron-induced reaction cross section measurements to higher energies, relevant to rare isotope facilities. These measurements can be used to inform and benchmark simulation of experiments that require neutron detection, particularly those utilizing organic scintillators. For some experiments, simulations are used to extract physics information from experimental data, reinforcing the need for accurate simulations.

Methods: Two sCVD diamond detectors were used as active targets at LANSCE, where neutrons up to 800 MeV are produced via spallation.

Results: Relative cross sections are reported from incident neutron (kinetic) energies $E_n = 12$ MeV up to 55 MeV for $^{12}\text{C}(n,\alpha_0)$, up to 46 MeV for $^{12}\text{C}(n,d_0)$, and up to 27 MeV for $^{12}\text{C}(n,p_0)$ and $^{12}\text{C}(n,p_1)$. These measurements extend these cross sections to higher energies than previous studies.

Conclusions: Good agreement is found between this work and recent experimental data from the EXFOR database in the neutron energies where the studies overlap. This work supports the need to update the ENDF evaluation for the (n,α_0) channel with more recent data, and provides data that could allow for an evaluation of the (n,p_0) , (n,p_1) , and (n,d_0) channels. These cross sections will increase the accuracy of simulations by extending the energy range for which empirical cross sections are available and including new reaction channels.

Acknowledgments

First and foremost, I would like to thank my parents for their contributions to get me to this point. My mom always likes to say that I grew up in a pro-reading environment. My dad often had me looking at math problems on napkins at the dinner table. Their constant support has helped me through difficult times.

Next, I would like to specially thank Warren Rogers for taking me on as a research student in 2017. I would not be here if not for you. I've learned so much from you, including physics, programming, and data analysis. You opened my eyes to the exciting world of nuclear physics. I would also like to thank Anthony Kuchera for all that he has done for me, from being co-PI for the LANSCE experiment that became my thesis experiment, to assisting with the data analysis, providing undergraduate student researchers, and helping to oversee my progress.

I would like to thank Paul Gueye for the personal support that he has provided. In addition to being the coolest advisor around, he is a man I respect. I would also like to thank Belen Monteagudo and Thomas Redpath for their help in mentoring me early in graduate school and helping get me started in MoNA research as a graduate student.

I would also like to thank the attendees of my analysis meetings: Anthony Kuchera, Warren Rogers, Thomas Baumann, Nathan Frank, Thomas Redpath, and Paul Gueye. These meetings were very beneficial, and helped keep the project moving forward.

I am also grateful to the undergraduate students who contributed to the project. Chief among them is Andrew LaRochelle, who fit most of the data, and worked to improve the R-matrix fits. Current MoNA graduate students have also contributed to my project and to my time at MSU, namely Georgia Votta and Nico Mendez. I have truly enjoyed our lunch talks, travel, and work on research and classes together.

I would also like to thank the LANSCE staff who provided the beam and kept everything running fairly smoothly. In particular, I would like to thank Sean Kuvin for lending us his diamond detector and providing key insight into the analysis at various crucial points. I would like to thank Keegan Kelly for providing the fission chamber data and excellent comments about the paper. I want to thank Matt Devlin for providing information about all things LANSCE, including flight path distances, flux simulation, collimation, beam image information, and many other things, too numerous to list here. His support was crucial at the beginning of the experiment, and he literally moved the beam line to help us get neutrons. Jack Winklebauer was also a great help during the experiment, lending us the computer, digitizer, high voltage modules, and helping us downscale the T0 signals.

I'd like to thank my committee members for their knowledge and support for the change in project: Paul Gueye, Calem Hoffman, Anthony Kuchera, Filomena Nunes, Kendall Mahn, Reinhard Schwienhorst.

Finally, I would like to acknowledge the federal funding that made this work possible. This work

was supported by the National Science Foundation, grant numbers PHY 2012040, PHY 2310078, PHY 2311125, PHY 2311126, and PHY 2011265, and the U.S. Department of Energy, Office of Science, Office of Nuclear Physics, Award Number DE-SC0022037.

Contents

1	BACKGROUND AND MOTIVATION	7
1.1	Introduction	7
1.1.1	The Chart of the Nuclides	7
1.1.2	Invariant Mass Spectroscopy	8
1.1.3	Cross Sections	11
1.1.4	Q value	11
1.1.5	Spin and Parity	12
1.2	Previous MoNA Experiments at LANSCE	12
1.2.1	Kohley et al. (2012)	12
1.2.2	LANSCE 1: Rogers et al. (2016)	13
1.2.3	LANSCE 2: Kuchera et al. (2019)	13
1.2.4	LANSCE 3: Kuchera et al. (2023)	14
1.3	Previous Cross section Measurements	15
1.4	Simulation tools	16
1.4.1	GEANT4	16
1.4.2	MENATE_R	16
1.4.3	MCNP	17
1.4.4	neuSIM4	18
1.4.5	TALYS	18
1.5	R-matrix Theory	18
2	EXPERIMENTAL TECHNIQUE	21
2.1	Beam Production	21
2.2	Collimation	22
2.3	Beam Alignment and Imaging	23
2.4	Fission Chamber	26
2.5	Diamond Detectors	26
2.5.1	Diamond Detector Position Optimization	27
2.6	MoNA	28
2.7	Electronics and DAQ	29

2.8	High Voltage	31
3	DATA ANALYSIS	32
3.1	Calibrations and Corrections	32
3.1.1	Diamonds	32
3.1.2	Fission Chamber	34
3.1.3	Beam Images	35
3.2	Event Selection	36
3.2.1	Q value calculation	36
3.3	Background subtraction	41
3.3.1	External sources of background	41
3.3.2	Internal sources of background	42
3.4	Modeling and Simulation	46
3.4.1	Charged Particle Detection Efficiency	46
3.4.2	Neutron attenuation in air	46
3.4.3	MCNP Flux	48
3.5	Cross section normalization	49
3.6	R matrix fits	51
4	RESULTS AND DISCUSSION	54
4.1	Cross sections	54
4.1.1	$^{12}\text{C}(n,\alpha)^9\text{Be}$	54
4.1.2	$^{12}\text{C}(n,p_0)^{12}\text{B}$	54
4.1.3	$^{12}\text{C}(n,p_1)^{12}\text{B}$	56
4.1.4	$^{12}\text{C}(n,d_0)^{11}\text{B}$	56
4.1.5	$^{12}\text{C}(n,d_0)^{11}\text{B} + ^{12}\text{C}(n,p_1)^{12}\text{B}$	57
4.1.6	Cross section uncertainties	58
4.1.7	Visualizing cross section uncertainties	61
4.2	R-matrix fits	71
4.2.1	$^{12}\text{C}(n,\alpha)^9\text{Be}$	71
4.2.2	$^{12}\text{C}(n,p_0)^{12}\text{B}$	72
4.2.3	$^{12}\text{C}(n,p_1)^{12}\text{B}$	73
4.2.4	$^{12}\text{C}(n,d_0)^{11}\text{B}$	74
4.3	MENATE_R Improvements	78
4.3.1	New Channels in MENATE_R	78
4.3.2	Cross section updates in MENATE_R	78
4.3.3	Potential Future Updates with MENATE_R	88

5 SUMMARY AND CONCLUSIONS	92
5.1 Implications	92
Appendices	103
A Cross section data tables	104
B digiTES configuration file	118

Chapter 1

BACKGROUND AND MOTIVATION

1.1 Introduction

99.9% of the visible universe by mass is made up of atomic nuclei [1]. Within the nucleus are nucleons, which include protons and neutrons. These nucleons populate energy levels in the nucleus, and the focus of nuclear structure is to study how nucleons arrange themselves in the nucleus. Another way of studying nuclei is through nuclear reactions. When two nuclei collide, a myriad of processes can occur, revealing key insights about the nuclei involved. The study of nuclear reactions is crucial for understanding stellar evolution, and numerous applications of nuclear science, including stockpile stewardship, nuclear power, and nuclear medicine also critically depend on understanding nuclear reactions [1]. This study is conducted within the subfields of nuclear structure and nuclear reactions.

1.1.1 The Chart of the Nuclides

A common way to view isotopes is in the chart of the nuclides, shown in Fig. 1.1, where each square corresponds to a given nuclide, uniquely defined by the number of protons and the number of neutrons. The nuclides in the chart are colored according to their decay mode: the black nuclides are stable, those in the pink region undergo beta-minus decay, the ones in the blue region undergo beta-plus decay, and the yellow and green regions correspond to alpha decay and spontaneous fission, respectively. Of particular relevance to this thesis are the nuclides colored in purple, located in the relatively low-mass, neutron-rich region of the chart. These nuclides decay by neutron emission, an exotic decay mode only possible for very neutron-rich isotopes. The orange boxes on the proton-rich (neutron-deficient) side correspond to isotopes that decay by proton emission. The blue outlined boxes correspond to magic numbers: nuclei with particular numbers of protons and/or neutrons (2, 8, 20, 28, 50, 82, and 126) exhibit enhanced stability due to closed shells. The limits of the chart, where no more neutrons can be added or removed to form a bound nucleus, are known as the neutron and proton driplines, respectively. The corresponding nuclei beyond these driplines are unbound.

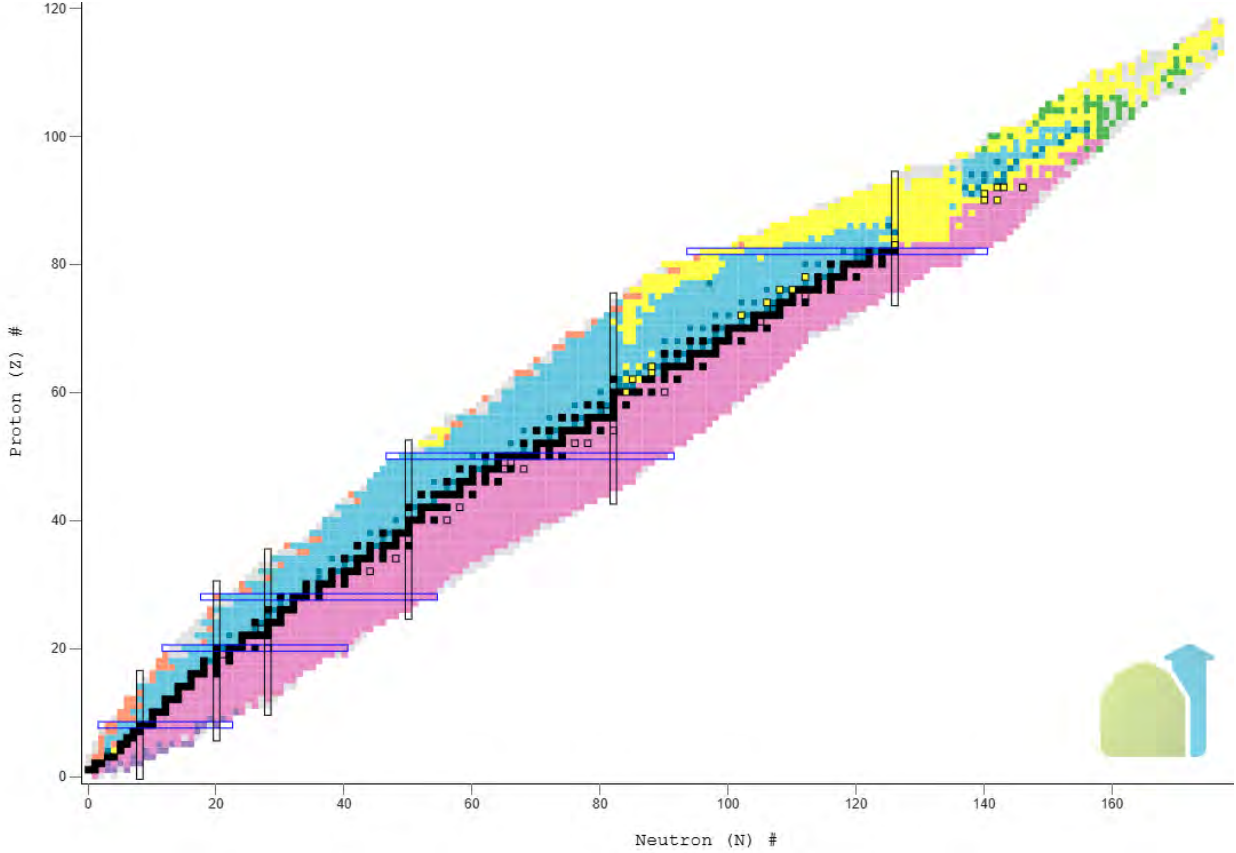


Figure 1.1: The chart of the nuclides, plotting the proton number vs. the neutron number for each isotope. The color of each nuclide is chosen by its decay mode. The chart was obtained from NNDC's NuDAT. [2].

1.1.2 Invariant Mass Spectroscopy

As previously mentioned, the structure of nuclei far from stability is an important testing ground for nuclear theory models. Notably, the study of nuclei around the neutron dripline can reveal interesting phenomena, including inverted level schemes [3, 4], multi-neutron emission [5, 6, 7], and halo nuclei [6, 7]. One way to study these nuclei is through invariant mass spectroscopy, which arises from the conservation of four-momentum. In this technique, rather than directly observing the very short-lived unbound nuclei, which have characteristic lifetimes of $\sim 10^{-21}$ s, the decay products are studied which include a charged fragment and one or more neutrons in our case.

Consider a binary decay of the form

$$A \rightarrow B + C \quad (1.1)$$

where A is the unbound nucleus. Conservation of four-momentum dictates that the initial and final four-momenta be equal, i.e.

$$p_A^\mu = p_B^\mu + p_C^\mu \quad (1.2)$$

p^μ is the four-momentum, given by

$$p^\mu = (p^0, p^1, p^2, p^3) = (E, p_x, p_y, p_z) \quad (1.3)$$

where E is the relativistic energy and $\mathbf{p} = (p_x, p_y, p_z)$ is the relativistic three-momentum. The four momentum is dependent on the reference frame, but the square of the four-momentum is not, and is thus Lorentz-invariant.

$$(p_A^\mu)^2 = (p_B^\mu + p_C^\mu)^2 = (p_B^\mu)^2 + (p_C^\mu)^2 + 2(p_B)^\mu (p_C)_\mu \quad (1.4)$$

When evaluated in their rest frame, $(p_A^\mu)^2$, $(p_B^\mu)^2$, and $(p_C^\mu)^2$ simplify to m_A^2 , m_B^2 , and m_C^2 , the square of their rest masses. Thus, Eq. 1.4 becomes

$$m_A^2 = m_B^2 + m_C^2 + 2(E_B E_C - \vec{p}_B \cdot \vec{p}_C) \quad (1.5)$$

The decay energy is defined as the difference between the initial and final masses in the decay:

$$E_{decay} = m_A - \sum_i m_i = m_A - (m_B + m_C) \quad (1.6)$$

Plugging Eq. 1.5 into Eq. 1.6, one obtains

$$E_{decay} = \sqrt{m_B^2 + m_C^2 + 2(E_B E_C - \vec{p}_B \cdot \vec{p}_C)} - (m_B + m_C) \quad (1.7)$$

This derivation uses natural units, with $c = \hbar = 1$, a convention that is followed throughout this chapter. A practical example is neutron-unbound ^{30}F , which decays into ^{29}F and a neutron. Denoting ^{29}F as “B” and the neutron as “C”, the decay energy of ^{30}F can be calculated with Eq. 1.7. A similar derivation can be followed in cases where the decaying nucleus is unbound to two (or more) neutron emission.

Typical setups for such invariant mass measurements feature a suite of detectors for detecting the charged fragments, and a large volume organic scintillator array for detecting the neutrons, such as MoNA [8], NEBULA [9], or NeuLAND [10]. Further discussion of the charged fragment detection is not relevant here, but details can be found in Ref. [11]. For an invariant mass measurement, the neutron detector must be able to measure the energy and momentum of the neutrons, typically by measuring their position and time of flight. These neutron detector arrays are typically designed to maximize the detection efficiency for fast neutrons.

Once the decay energy is determined from the experiment, it is fit with simulated lineshapes to aid in the determination of the angular momentum, resonance energy, and width of the state from which the neutrons were emitted. Furthermore, these simulations depend on accurate knowledge of the neutron interactions within organic scintillator, including reaction and decay dynamics as well as detector resolutions and efficiencies. Thus, the interpretation of experimental data is crucially dependent on the quality of the simulations.

Types of Nuclear Reactions in Organic Scintillator

The primary detection method for fast neutrons uses organic scintillator, which is composed of carbon and hydrogen atoms. Neutron interactions within organic scintillator can be broadly grouped into three categories: elastic scattering of neutrons off hydrogen nuclei, elastic scattering of neutrons off carbon nuclei, and inelastic reactions with carbon nuclei, which will be described briefly. For neutrons incident on organic scintillator, elastic scattering on carbon is $^{12}\text{C}(n, n)^{12}\text{C}$ and elastic scattering on hydrogen is $^1\text{H}(n, n)^1\text{H}$. In elastic reactions, the kinetic energy is conserved before and after the reaction; therefore, the target nucleus is not excited and remains in the same state as it was prior to the reaction. Many more inelastic reactions are possible than elastic. Here, the kinetic energy is not conserved, since some of the energy is used to excite the nucleus or to transmute a nucleus into a different one. The most basic inelastic reaction on ^{12}C is inelastic scattering, in which a neutron is scattered off ^{12}C , but also excites the ^{12}C nucleus to a higher energy state: $^{12}\text{C}(n, n' + \gamma)^{12}\text{C}^*$.

There are a number of reactions that include only charged particles in the exit channel. This includes the charge-exchange reaction, in which a neutron is in the entrance channel, while a proton is in the exit channel: $^{12}\text{C}(n, p)^{12}\text{B}$. In charge-exchange reactions, both energy and charge are exchanged between the projectile and the target. In nucleon transfer reactions, multiple nucleons are transferred between the target and the projectile. Examples of these reactions include $^{12}\text{C}(n, d)^{11}\text{B}$ and $^{12}\text{C}(n, \alpha)^9\text{Be}$. These reactions can also populate the daughter nucleus in an excited state.

Lastly, another type of inelastic reaction is a breakup reaction in which multiparticle emission occurs. An example of this is $^{12}\text{C}(n, n' + 3\alpha)$. Since there is only one bound state of ^9Be , this reaction is similar to $^{12}\text{C}(n, \alpha)^9\text{Be}$, except that an excited state of ^9Be is populated, which decays into a neutron and two additional alpha particles.

A more thorough list of possible $n + ^{12}\text{C} \rightarrow X$ reactions is included in Table 3.1 for channels with charged particles in the exit channel and in Table 3.3 for channels with neutrons in the exit channel. However, these tables are not meant to be exhaustive.

Light vs Dark Scattering in Organic Scintillator

Elastic collisions with hydrogen nuclei (protons) result in a larger momentum transfer, so the protons inherit a large fraction of the incident neutron kinetic energies. These protons produce light in the scintillator with high efficiency. On the other hand, carbon-elastic scattering produces very little light in the scintillator: the neutron trajectory is changed, and the interaction location cannot be measured directly. This introduces uncertainty into the neutron event reconstruction in large detector arrays like MoNA and is known as “dark scattering”. Any reaction channel with only a heavy ion and neutrons in the exit channel is expected to interact via such dark processes, including $^{12}\text{C}(n, 2n)^{11}\text{C}$. Other neutron-carbon interactions that produce light ions may or may not produce significant light in the scintillator because the momentum transfer from the incoming

neutron to the light-charged reaction products is less efficient than that of the neutron-hydrogen interactions.

1.1.3 Cross Sections

A cross section in nuclear physics is a measure of the effective area of interaction between the projectile and target, but is also analogous to the likelihood that a particular reaction will occur. It is generally defined as

$$\sigma = \frac{N}{N_{beam}\rho} \quad (1.8)$$

where σ is the cross section for a particular reaction, N is the number of those particular reactions, N_{beam} is the number of beam nuclei (time-integrated beam flux, Φ), and ρ is the density of target nuclei. An inclusive cross section can be thought of as the likelihood for a given type of reaction to occur without specifying the full products in the final state, such as proton production or alpha particle production. Inclusive reactions can be further divided into exclusive reactions, in which the final state is fully specified, including the state of the daughter nucleus. The total cross section is the sum of all the exclusive cross sections. For the case of neutrons incident on ^{12}C ,

$$\sigma_{total} = \sigma_{(n,n)} + \sigma_{(n,n'\gamma)} + \sigma_{(n,\alpha)} + \sigma_{(n,p_0)} + \sigma_{(n,p_1)} + \sigma_{(n,d_0)} + \sigma_{(n,d_1)} + \sigma_{(n,t_0)} + \dots \quad (1.9)$$

where p, d, and t represent protons, deuterons, and tritons, respectively. The subscript refers to the state of the daughter nucleus populated, with 0 for the ground state, 1 for the first excited state, and so on. This follows the convention used in recent literature [12, 13, 14, 15], with the benefit that the shorthand for the reaction uniquely identifies it: i.e. (n,d_0) refers to $^{12}\text{C}(n,d)^{11}\text{B}_0$ with ^{11}B in the ground state. This notation is consistently applied throughout.

Measuring the neutron flux Φ presents many challenges since neutrons often pass through materials without depositing any energy. When the number of incident particles cannot be determined directly, it can be helpful to extract the experimental cross section relative to a well-known reference reaction. In our study, cross section measurements were performed relative to previous $^{12}\text{C}(n,\alpha)^9\text{Be}$ cross section measurements [12, 16, 17, 18, 19].

1.1.4 Q value

The Q value is defined as the mass energy difference between the initial and the final states of a process:

$$Q = \sum_i m_i - \sum_f m_f \quad (1.10)$$

where $\sum_i m_i$ represents the sum over the masses in the initial state and $\sum_f m_f$ the sum over the masses in the final state. For instance, a decay process with a positive Q value is exothermic and

can occur spontaneously, while a decay with a negative Q value is endothermic and requires a net input of energy to occur. For a reaction, if the Q value is negative, there must also be a net input of energy for it to occur, known as the threshold energy, E_{th} . In the case of a binary reaction $A(a,b)B$, E_{th} depends on the Q value as follows:

$$E_{th} = \frac{-Q(m_a + m_A)}{m_A} \quad (1.11)$$

where m_a and m_A represent the masses of the incident and target nuclei, respectively. If the kinetic energy of the incident particle is less than the threshold ($E_a < E_{th}$), then the reaction cannot occur.

1.1.5 Spin and Parity

Every state of a nucleus is characterized by a spin and parity, commonly abbreviated as J^π , where J is the total angular momentum and π is the parity. The total angular momentum can take either only integer values, for a nucleus with an even number of nucleons, or only half-integer values, for a nucleus with an odd number of nucleons. The parity is either positive (+) or negative (-), depending on whether the state has even or odd parity, respectively. This depends on the parity of each individual nucleon: an odd parity for a nucleus arises from an odd number of nucleons with odd parity.

1.2 Previous MoNA Experiments at LANSCE

Four experiments have been performed that were designed to test and ultimately improve simulation of neutron interactions with organic scintillator, specifically with MoNA. The work described in this manuscript builds on previous experiments conducted by the MoNA Collaboration at the LANSCE facility.

1.2.1 Kohley et al. (2012)

The first MoNA experiment at LANSCE (LANSCE 1) was inspired by the work of Kohley *et al.* [20], which analyzed data from an NSCL experiment to study $^{16}\text{B} \rightarrow ^{15}\text{B} + n$, resulting in 55 MeV neutrons. These neutrons were detected in MoNA, and the experimental data were compared with simulations utilizing two different physics options: MENATE_R [21] and the stock GEometry ANd Tracking (GEANT4) [22, 23, 24] physics options. For the latter, there exist two distinct energy regimes: (i) $E_n < 20$ MeV, where G4NeutronHPElastic and G4NeutronHPInelastic are used and (ii) $E_n > 20$ MeV, where G4HadronElasticProcess and G4LElastic for elastic interactions and G4LENeutronInelastic and G4CascadeInterface for inelastic interactions. Above 20 MeV, G4Neutron-HPJENDLHEElasticData and G4NeutronHPJENDLHEInelasticData are used to implement neutron cross sections from the high-energy Japanese Evaluated Data Library (JENDL [25])). In this work, various observables were compared between experimental data and the two

simulation packages. In particular, the experimental hit-multiplicity distribution and energy deposition agreed much better with `MENATE_R` than with the stock `GEANT4` physics list. However, since experiments at FRIB can produce neutrons up to 200 MeV, further study was needed.

1.2.2 LANSCE 1: Rogers et al. (2016)

The LANSCE 1 experiment followed up on that work, making similar comparisons over a much larger incident neutron energy range, from 20-200 MeV. This experiment used 16 MoNA bars in a 2×8 array (two rows of eight bars), with the neutron beam impinging on the front bar of the top row. Rogers *et al.* presented neutron scattering observations, including hit-multiplicity distributions, beam attenuation depth, cross-talk events, scattering angle distributions, attenuation depth between hits, and dark scattering of neutrons from carbon nuclei, all as a function of incident neutron energy [26]. These observables were compared between experimental data and two simulation packages: one using `MENATE_R` and the other using `GEANT4` physics lists. Unlike the work from Kohley *et al.* [20], in which a general recommendation could be made for the use of `MENATE_R` rather than the `GEANT4` physics lists for their energy window, Rogers *et al.* could not make such a recommendation. Instead, it was found that certain observables in certain energy ranges showed better agreement with one simulation package or the other. This suggested that further work was needed with both `MENATE_R` and `GEANT4` physics lists to improve their agreement with experimental data.

Additionally, the LANSCE 1 experimental setup was not optimized for a rigorous exploration of dark scattering and the angular distributions of dark-scattered neutrons. Dark scattering in organic scintillator is primarily observed by detecting a neutron’s first interaction at a location where the neutron beam cannot reach- thus, a neutron must have scattered previously but not triggered the detector to reach that location and have it register as the first interaction. Due to the compact design of the 2×8 setup, used because of its similarity to the setup of MoNA experiments at NSCL/FRIB, neutrons detected first in the bottom layer of the array were easily ascribed to dark scattering. However, there was significant ambiguity in the location of the initial dark scattering. For example, a dark scattered neutron detected in the furthest back bar in the bottom layer could have been scattered from any bar in the top or could have dark scattered multiple times, once in the top layer and one or more times in the bottom layer to reach the point where it was eventually detected.

1.2.3 LANSCE 2: Kuchera et al. (2019)

The ambiguity of LANSCE 1 regarding the dark scattering location inspired the second MoNA experiment at LANSCE (LANSCE 2), in which the same 16 MoNA bars were used, but in a different configuration. One MoNA bar was used as a target, and the other 15 bars were placed in a stair-step design, thereby eliminating the ambiguity in the dark scattering location. Furthermore, the longer path length between the target bar and the stair-step bars (about 2 m compared to 0.1

m during LANSCE 1) increases the angular resolution. This configuration also enabled the study of light scattering with an air gap between bars, a setup sometimes used by MoNA to better identify two neutron events [27]. The analysis of this experiment is still ongoing. Two primary issues have complicated this analysis. First, the key signature of dark-scattering events, a first interaction in the detector in a location which could not have been possible without previous scattering, removes the coincidence requirement, making background much more of an issue. Second, “halo” neutrons that originate from scattering within the collimator can behave like scattered neutrons, since their angular distributions are much larger than the divergence of the primary neutron beam neutrons. The insights gleaned from the LANSCE 1 and 2 experiments have led to improvements in recognizing dark scattering in event reconstruction. One approach uses the neutron spacetime interval [26] to categorize neutron multi-hit events as those with multiple neutrons (if they are spacelike) or potentially caused by the same neutron (if they are timelike).

1.2.4 LANSCE 3: Kuchera et al. (2023)

A recent publication from Kuvín *et al.* [15] demonstrated the abilities of a diamond detector as an active target when used with a white neutron source, specifically at LANSCE. A diamond detector does not depend on the conversion of neutron kinetic energy into light; rather, it directly measures the kinetic energy of $n + C$ reaction products. Thus, events that would not be detected in an organic scintillator due to dark scattering can be observed in a diamond detector. Thus, looking at neutrons scattered from the diamond detector could improve on the LANSCE 2 experiment since the n - C interactions would trigger the target diamond detector unlike the target bar in LANSCE 2. The coincidence measurement between the diamond detector where the neutron scatters and one of the MoNA bars, where the neutron is eventually detected, allows for the removal of the background that plagued the LANSCE 2 experiment. Furthermore, the small size of the diamond detector reduces the position uncertainty of the target and hence reduces the angular uncertainty. Kuvín *et al.* [15] also demonstrated the ability of a diamond detector to discern between different reaction channels, including $^{12}\text{C}(n,\alpha)^9\text{Be}$, $^{12}\text{C}(n,p_0)^{12}\text{B}$, and $^{12}\text{C}(n,d_0)^{11}\text{B}$. The LANSCE 3 experiment discussed in this thesis used two diamond detectors with the existing 16 MoNA bars (see Chapter 2).

The angular distributions of neutrons, particularly with knowledge of the particular reaction channel from which they originate, are of great interest to the MoNA Collaboration [8] and those who detect and simulate neutrons with large plastic scintillator arrays. Some limited angular distribution data were obtained in the experiment described in the present work, with neutrons interacting in the diamond and reaction products being detected in a wall of MoNA bars. The limitation arises from the fact that most of the distinct reaction channels that are identified in the diamond are due to reactions that only produce charged particles and are fully stopped in the diamond. Furthermore, while the small size of the diamond detector reduces the angular uncertainty for a scattering experiment, it significantly limits the statistics. Combined with the limited efficiency of a single layer of MoNA, the coincident neutron scattering dataset is rather limited. The study

presented in this thesis focuses on four reaction channels with the least negative Q values with only charged particles in the exit channel: $^{12}\text{C}(n,\alpha)^9\text{Be}$, $^{12}\text{C}(n,p_0)^{12}\text{B}$, $^{12}\text{C}(n,p_1)^{12}\text{B}$, and $^{12}\text{C}(n,d_0)^{11}\text{B}$. In particular, energy-differential cross sections for these channels were determined.

1.3 Previous Cross section Measurements

The first experiments that studied these interactions and measured cross sections for particular reaction channels used the activation technique, in which a ^{12}C sample was irradiated with neutrons, and the beta decay of the reaction products was recorded and identified by beta energy and lifetime. This is beneficial when the daughter nucleus is radioactive and decays by beta decay. Thus, of the daughter nuclei most commonly produced by n-C interactions, ^{12}B , ^9Li , ^8B , ^6He , ^8Li , ^{10}C , ^{11}C , ^7Be , and ^{10}Be , can be studied using this method. Kellogg [28] studied these reactions and obtained cross sections for the production of each daughter nucleus. In this study, a cloud chamber was also used to identify light charged particles produced in n-C interactions, but unique reactions could be deduced only for certain combinations of daughter nuclei and light charged particle products. However, the incident neutron energy in the Kellogg study was not well known (90 ± 60 MeV) which, combined with the ambiguity of the identifications, made this study less than ideal for a precise cross section determination.

Of the possible daughter nuclei that undergo beta decay, $^{12}\text{C}(n,p)^{12}\text{B}$ has been studied the most. Cross sections for this charge-exchange reaction were published in various studies, including those of Bobyr [29], Ablesimov [30], Rimmer [31], and Kreger [32], all of which used the activation method. Among these studies, some high-resolution (with respect to incident neutron energy) cross-section data exist. However, these are limited to incident neutron energies up to 22 MeV. Additionally, these studies could only measure the total production of ^{12}B . This is valuable information, but it is desirable to have sensitivity to which state of ^{12}B is populated, as this affects the reaction kinematics.

The $^{12}\text{C}(n,\alpha)^9\text{Be}$ reaction has been studied extensively over the past 60 years, but typically at low incident neutron energy. Various detector systems and setups have been used, including solid scintillator [33, 34, 35], gridded ionization chambers [18, 36, 37, 38], nuclear emulsions [39, 40], liquid scintillators [41, 42, 43], and $\Delta\text{E-E}$ detectors [16, 19, 44]. The activation technique is not an option here, since ^9Be is stable. A preponderance of data has been taken around 14 MeV incident neutron energy, sometimes to provide calibration data for other measurements [37]. More recently, sCVD diamond detectors have been used [12, 13, 15, 14, 45], which have many benefits over other detectors: (i) these electronic-grade diamonds have good time resolution, allowing for incident neutron energy reconstruction, and (ii) they have good energy resolution, allowing for differentiation between various reaction channels, including the ability to discriminate between various states of daughter nuclei that can be populated. Pulse shape discrimination has been used with both liquid scintillators and diamond detectors to gain further insight into which interactions are occurring within the detector. In Section 4.1, the cross sections determined in the present work

for $^{12}\text{C}(n,\alpha)^9\text{Be}$, $^{12}\text{C}(n,p_0)^{12}\text{B}$, $^{12}\text{C}(n,p_1)^{12}\text{B}$, and $^{12}\text{C}(n,d_0)^{11}\text{B}$ are compared with recent data, most notably those obtained with diamond detectors.

1.4 Simulation tools

There are numerous packages that are used to simulate neutron interactions with matter, in particular neutron interactions with carbon and hydrogen. Every package presented below uses experimental data for at least some of the cross section information, whether exclusively through direct implementation, or indirectly as a normalization to a given simulation. In every case, the quality of the simulation is limited by the quality of the cross section data that is used in the simulation or used to normalize the results. Thus, while a particular focus in this work is given to `MENATE_R` and improving its modeling of n-C interactions, the cross sections measured in this work and in future analysis of this dataset would benefit every simulation package. While these are some of the most widely used softwares for simulating neutron interactions with matter, this list is not exhaustive.

1.4.1 GEANT4

The Geometry ANd Tracking (`GEANT4`) software is a Monte Carlo simulation toolkit to model particle interactions with matter [22, 23, 24]. `GEANT4` features many physics lists, which use different methods of simulating neutron interactions with matter, but most involve solving the particle's equations of motion and may use some cross section data in particular energy ranges. Elastic, inelastic, and total cross sections and angular distribution data are adopted or parametrized from experimental data where possible. In particular, the `QGSP_BIC_HP` physics list will be described, as simulations were performed with it during the course of analysis. The `QGSP_BIC_HP` physics list differs from the `QGSP_BIC` physics list by the use of the high precision neutron package (`NeutronHP`), which uses empirical cross sections from thermal energies up to 20 MeV. Once again, the cross sections in this energy range have not been determined for every possible n-C reaction channel and could benefit from new measurements. The physics list uses the binary cascade model from about 100 MeV to 10 GeV, and above 10 GeV, the physics list uses the Quark Gluon String model, but both of these are outside the scope of this work. However, the energy region for the binary cascade, a type of intranuclear cascade model, is relevant for the simulation of experiments at fast beam facilities such as FRIB and RIBF [46]. Under 100 MeV, particles are simulated with the precompound and nuclear de-excitation models.

1.4.2 MENATE_R

`MENATE_R` is a simulation package built on a `GEANT4` framework that uses measured cross section data to simulate n-C, n-H, n-Al, and n-Fe interactions [21]. `MENATE_R` is used by nuclear structure groups such as MoNA to simulate experimental data. `MENATE_R` is also used by neutrino physicists

to simulate the neutron background in their detectors [47]. Based on which elements are present, `MENATE_R` reads in neutron energy-dependent cross section files to model the various interactions and performs linear interpolation for neutrons with energies that differ from the tabulated values. The cross sections at that incident neutron energy, for all possible interactions, are used to decide which, if any, interaction occurs. At each step through a material, either one or zero processes are chosen to occur based on their cross sections. A random number generator is used to select from the possible reactions, weighted by each reaction cross section. When a reaction is selected to occur, it is simulated in `GEANT4`.

For inelastic processes, the reactions involve different entrance and exit channels. For example, $^{12}\text{C}(n,\alpha)^9\text{Be}$ is treated within `GEANT4` by killing the neutron and ^{12}C at the reaction location and creating an α particle and ^9Be . Momentum and energy conservation are used to calculate the kinematics for the outgoing particles, given the Q values. At the time of writing this dissertation, `MENATE_R` uses classical kinematics. The energy loss of charged reaction particles in materials is handled by `GEANT4`. If neutrons are present in the exit channel, they can interact again in the detector, although this is far more likely with a thick scintillator than with a thin diamond detector.

Due to the empirical cross sections it uses, `MENATE_R` is uniquely suited for simulating organic scintillators for neutron detector setups. However, the simulation is only as good as the cross sections it uses, and cross section data is sparse at higher incident neutron energies. Prior to the present work, very little partial cross section data for neutrons on ^{12}C existed above 22 MeV.

1.4.3 MCNP

Another widely-used simulation package is Monte Carlo N-particle (MCNP) [48], which is used for simulating the interactions of neutrons, photons, electrons/positrons, protons and ions with matter. The primary benefit of MCNP is its extensive cross section libraries that feature cross section data for far more particle-material combinations than `MENATE_R` or `GEANT4`. Furthermore, the cross section information contained in MCNP is updated more frequently and is more often evaluated data, compared to `MENATE_R` which has been updated very little in the past 15 years. However, since exclusive cross sections for many n-C reactions have not been published (or evaluated), there is still room for improvement. MCNP uses pseudo-random numbers to sample the probability distribution functions for each simulated particle and process. Another benefit of MCNP is its ability to simulate the effects of radiation on materials, such as particle heating or fission heating. For all these reasons, MCNP is widely used for the simulation of various aspects of nuclear security, including radiation shielding, dosimetry, reactor design, decontamination, nuclear safeguards, decommissioning, and nonproliferation. MCNP is also used for medical physics and radiography, as well as more fundamental science and detector design. The primary drawback of using MCNP is that it is not open source. It requires a license fee and is export controlled. We did not have access to the code for this analysis, though we did have an MCNP simulation of the neutron flux at LANSCE provided by our LANL collaborators.

1.4.4 neuSIM4

A recently developed simulation package, the neutron SIMulation (neuSIM4) package [49], combined empirical data at low energies with cascade models at higher energies, with a transition region at intermediate energies to reduce discontinuities between the two approaches. The low-energy, empirical portion of the simulation (KSCIN) uses evaluated “data” from the JAEA, and is at least as good as the cross sections currently used in MENATE_R. However, although KSCIN is nominally applicable up to 80 MeV, it relies on calculations above 20 MeV since many exclusive cross sections have not been measured in that energy window. Thus, it would benefit from cross section measurements of new channels and at higher energies, much like the existing version of MENATE_R. The high-energy portion of neuSIM4 shows strong agreement with experimental data, especially using the intra-nuclear cascade model. Their approach is likely superior to that of MENATE_R above 110 MeV, since partial cross sections of n-C reactions at those energies are not likely to be measured for at least a few years. Thus, an empirical approach in this energy range is not practical at this time.

1.4.5 TALYS

A rather different sort of simulation is TALYS [50]. In contrast to the aforementioned codes (MENATE_R, GEANT4, MCNP, and neuSIM4), which primarily focus on detector response, TALYS is instead used for analyzing and predicting nuclear reactions. Among its various uses, perhaps the most basic is in the calculation of reaction cross sections. TALYS focuses on neutron, photon, and light ion reactions with $A > 12$ nuclei and describes reactions up to 200 MeV. Our cross section measurements were restricted to energies below 55 MeV, well within the energy range for which TALYS should be applicable, and focus on the lowest end of the target nuclei mass range. TALYS features various nuclear reaction models integrated into a single code, so that reactions can be calculated with an applicable model from eV scale up to 200 MeV. In this study, our experimentally determined cross sections were compared with TALYS cross sections using default parameters, in which TALYS automatically chooses its most relevant physics model based on the energy range and the projectile and target species. Notably, TALYS does not model resonance reactions and thus the resonances observed in our data could not be reproduced. Future work could involve modeling the resonance region of these cross sections.

1.5 R-matrix Theory

A useful tool for describing resonant behavior in nuclear physics is the R -matrix. The phenomenological R -matrix is used for parameterizing cross sections, particularly at low energy. The discussion is derived primarily from Ref. [51], while the cross section derivation summarizes that presented in [52]. More detailed descriptions of the theory are presented in both sources, as well as [53]. Specifically, we refer to the phenomenological R -matrix, as opposed to the calculable R -matrix,

which is used to solve the Schrödinger equation, typically in atomic physics applications. Most of the parameters have physical significance, a key benefit of the theory.

For a single channel, the R -matrix elements are given by

$$R_{lJ}(E) = \sum_{n=1}^N \frac{\gamma_{nlJ}^2}{E_{nlJ} - E} \quad (1.12)$$

where l is the orbital angular momentum, J is the total angular momentum, E is the center-of-mass energy, E_{nlJ} is the eigenenergy, and N is the number of poles that are relevant to the cross section. γ_{nlJ} are reduced width amplitudes and satisfy the relation for the width: $\Gamma = 2\gamma_{nlJ}^2 P_l$, where P_l is the penetration factor. The penetration factor contains most of the effects of transmission through the Coulomb barrier.

The R -matrix theory can be used to describe scattering states resulting from interactions of particles or systems of particles, such as nucleons and nuclei. To accomplish this, the configuration space is divided into two regions: the internal region and the external region. The dividing line between the internal and external regions is known as the channel radius. The channel radius can be rather arbitrary, but is chosen to be large enough that only long-range forces need to be considered in the external region and anti-symmetrization effects can be neglected. The system is considered to be confined in the internal region. Its eigenstates form a discrete basis, which can be determined. These square-integrable eigenstates can be used to expand a scattering wave function at an arbitrary energy in the internal region. At this point, the R -matrix can be calculated, which is equivalent to the inverse of the logarithmic derivative of the wave function at the boundary. This yields the scattering matrix when matched with the solution in the external region, and can also yield the bound states of the system. The external solution functions as a decreasing exponential in this situation. An iteration is required, because the decreasing exponential depends on the unknown binding energy.

For the case with multiple resonances and multiple channels, we can expand the wave functions in terms of different reaction channels, c . These are uniquely described by the set of quantum numbers: $\{\alpha(J_1, J_2), l, s, \nu, m\}$, where $\alpha(J_1, J_2)$ represents a pair of nuclei with spins J_1 and J_2 , l is the orbital angular momentum, s is the spin of the channel, which satisfies $|J_1 - J_2| \leq s \leq (J_1 + J_2)$, and ν and m are the components of s and l , respectively. The general R -matrix thus becomes

$$R_{cc'}(E) = \sum_{n=1}^N \frac{\gamma_{nc}\gamma_{nc'}}{E_n - E} \quad (1.13)$$

where

$$\gamma_{\lambda,c} = \left(\frac{\hbar}{2\mu_c R} \right)^{1/2} \int \Psi_c^* X_\lambda dS \quad (1.14)$$

represents the overlap integral between the channel wave function Ψ_c and the eigenstate wave function X_λ . This describes how much each particular channel c contributes to an eigenstate of the nucleus, λ . The formal partial width is given by

$$\Gamma = 2P_l \gamma_{\lambda_c}^2 \quad (1.15)$$

The observable width, which is more closely related to the width of the state that is observed in the experiment, is

$$\Gamma_{\lambda_c} = \frac{2P_l \gamma_{\lambda_c}^2}{1 + \gamma_{\lambda_c}^2 \frac{dS_l}{dE}} \quad (1.16)$$

The total width is the sum of all partial widths:

$$\Gamma_{tot} = \sum_c \Gamma_c \quad (1.17)$$

The scattering matrix (S Matrix) is defined as

$$\mathbf{S} = \frac{\mathbf{t}^{1/2} \mathbf{H}^- - a \mathbf{R} \mathbf{t}^{1/2} (\mathbf{H}^- - \beta \mathbf{H}^-)}{\mathbf{t}^{1/2} \mathbf{H}^+ - a \mathbf{R} \mathbf{t}^{1/2} (\mathbf{H}^+ - \beta \mathbf{H}^+)} \quad (1.18)$$

where \mathbf{t} is a diagonal matrix with elements $t_c = \hbar^2/2\mu$, \mathbf{H}^\pm are diagonal matrices with Hankel functions as the diagonal elements, and β is the logarithmic derivative of the R matrix evaluated at the channel radius a . The Hankel functions are composed of regular (F_l) and irregular (G_l) coulomb functions, $H_l^\pm = G_l \pm iF_l$, and are radial solutions to the Schrödinger equation with a Coulomb potential.

The S matrix can then be transformed into the symmetric matrix $\tilde{\mathbf{S}}$ by

$$\tilde{\mathbf{S}} = \mathbf{v}^{1/2} \mathbf{S} \mathbf{v}^{-1/2} \quad (1.19)$$

using the diagonal matrix \mathbf{v} with elements $v_c = \hbar k_c / \mu_c$.

The symmetric S matrix can now be written as

$$\tilde{\mathbf{S}} = \Omega [1 + 2iP^{1/2}(1 - a\mathbf{R}L)^{-1}\mathbf{R}P^{1/2}] \Omega \quad (1.20)$$

where Ω is a matrix whose diagonal elements are $e^{i\phi_c}$, and ϕ_c are the hard-sphere phase shifts.

We can now use the scattering matrix elements to calculate the total cross section from scattering to channel c from c' :

$$\sigma_{cc'}(J_{tot}^\pi) = \frac{\pi}{k_i^2} g_{J_{tot}} |\tilde{S}_{cc'}|^2 = \frac{\pi}{k_i^2} g_{J_{tot}} \frac{\Gamma_c \Gamma_{c'}}{(E - E_r^f)^2 + \Gamma_{tot}^2/4} \quad (1.21)$$

where E_r^f is the formal resonance energy and $g_{J_{tot}}$ is the spin weighting factor:

$$g_{J_{tot}} = \frac{2J_{tot} + 1}{(2J_p + 1)(2J_t + 1)} \quad (1.22)$$

in which J_p and J_t are the spin of the projectile and target nuclei, respectively. Clearly, the cross section is strongly peaked near the resonance energy. In this way, the R matrix theory can be used to calculate and parameterize cross sections.

Chapter 2

EXPERIMENTAL TECHNIQUE

2.1 Beam Production

The beam at LANSCE starts as hydrogen gas, which is ionized to form H^- . The H^- ions are injected into a linear accelerator (LINAC), where they are accelerated up to 800 MeV and subsequently pass through a carbon foil, stripping the electrons and converting the H^- to H^+ . This is a pulsed beam consisting of 120 macropulses per second, of which 100 are sent to WNR (Target 4), and the remaining 20 are sent to the nearby Lujan Center. Each macropulse is 625 μs in duration and composed of micropulses that are separated by 1.8 μs . The H^+ beam impinges on a tungsten target, producing fast neutrons via spallation, with a broad energy distribution up to 800 MeV, also known as a white neutron source. These neutrons propagate in all directions with a nearly isotropic angular distribution.

Flight paths (essentially holes through which neutrons pass) are set at various angles (15, 30, 60, and 90 degrees) relative to the initial H^-/H^+ beam line as shown in Fig. 2.1. The experiment described in this thesis was conducted on the 15 Degree Left (15L) flight path, which allows for the longest flight path distance at the LANSCE facility, approximately 90 m. The experiment was set up in the 90 meter station. Prompt gamma rays are also produced in the spallation target, allowing for precise time/distance calibrations.

Just before the protons impinge on the spallation target, they pass through a scintillator, providing a reference time measurement referred to as “T0” signals. These signals were routed to our data acquisition system (DAQ).

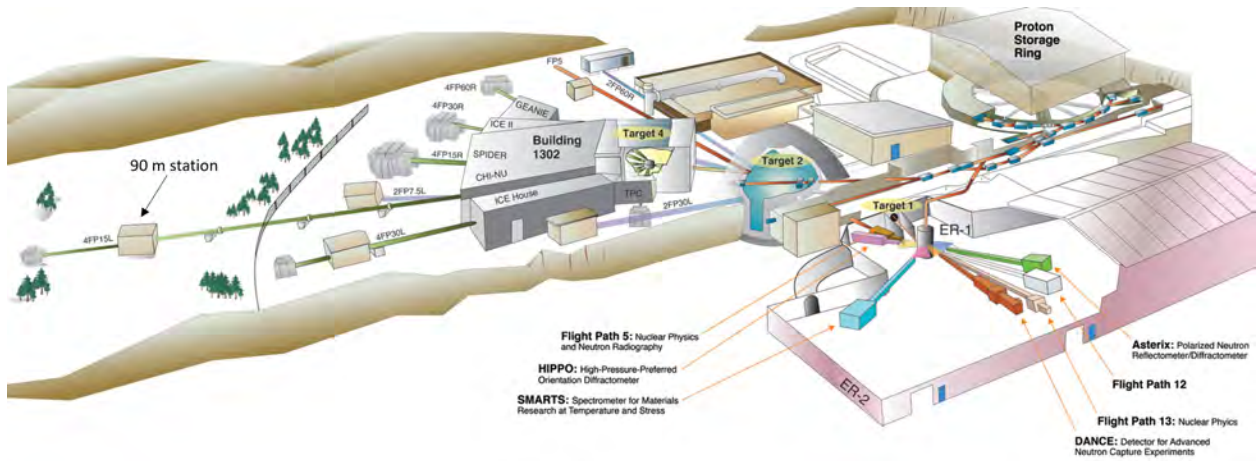


Figure 2.1: An overhead view showing the layout of the LANSCE facility [54]. Of note are Target 4 (the spallation target) and the 90 m station on the 15L flight path. The proton accelerator is not visible in this diagram.

2.2 Collimation

Along each of the flight paths, the beam is collimated to smaller spot sizes and solid angles. On the 15L flight path, there are three stages of collimation, which are summarized in Table 2.1 and depicted in Fig. 2.2. Between the collimators, the beam travels through open air or pipes. These pipes allow much larger solid angles than the collimation, so that the beamspot spreads out as the beam moves further downstream from the collimation. The final collimation stage ends at the entrance of the 90 m station. Only the first 6.54 m of the flight path are under (rough) vacuum. The remainder is in air. The attenuation of neutrons through the air was studied and is described later (Section 3.4.2).

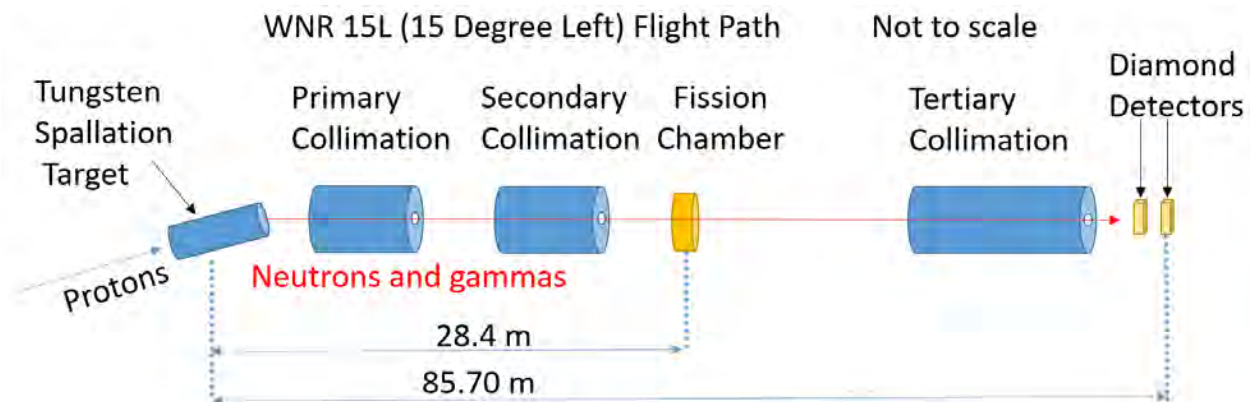


Figure 2.2: An overview of the 15L flight path. Two diamond detectors were placed 85.7 m from the spallation target. The primary, secondary, and tertiary collimation is shown, in addition to the spallation target and fission chamber.

Table 2.1: Summary of the collimation on the 15L flight path at LANSCE.

Collimation	Distance from Target 4 (m)	Length of Collimation (m)	Inner Diameter (mm)	Material
Primary	11.7	1.47	33	polystyrene, steel, borated polystyrene
Secondary	17.4	1.22	19	polystyrene, steel, borated polystyrene
Tertiary	84.7	0.76	3	steel

2.3 Beam Alignment and Imaging

To verify the position and alignment of the neutron beam, beam images were taken on film-like Storage Phosphor Screen BAS-IP [55]. These image plates consist of a photo-stimulable phosphor layer sandwiched between a protective layer and a support layer. The plate was placed in a light-tight aluminum holder and neutron converter before being placed in the beam. The plates are sensitive to neutrons and gammas and have a resolution of about 1 mm. At the beginning of the experiment, a beam image taken inside the 90 m station revealed no neutron beam, while a beam image taken upstream of the station revealed a strong beam. To help locate the beam, some of the collimation was removed, and another beam image was taken (Fig. 2.3a) demonstrating that the beam was not centered, and only some of the most intense portion of the beam was making it through the collimation. The beam pipe into the station was adjusted to improve the alignment. After a few iterations of taking new beam images and further adjusting the beam pipe, a new image showed the beam spot was more centrally located, with much better overlap between the beam spot and collimator exit as shown in Fig. 2.3b. For comparison, beam images taken at the fission chamber location, upstream of the collimation into the 90 m station, and downstream of the collimation into the 90 m station (after alignment) and their projections are also presented in Fig. 2.4.

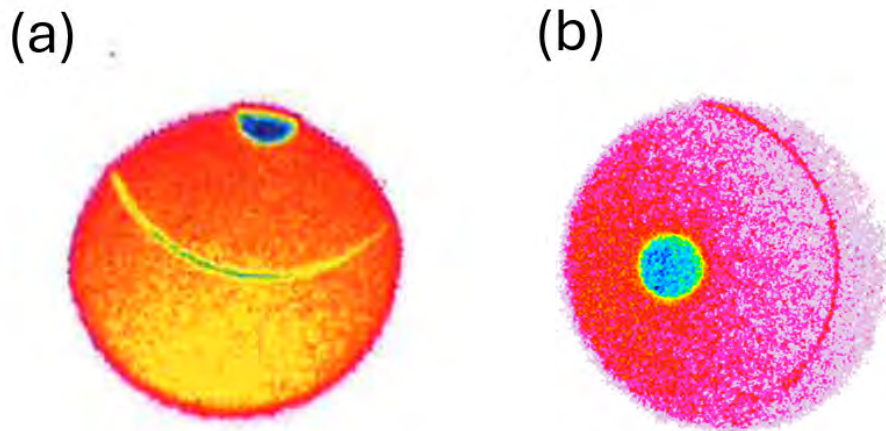
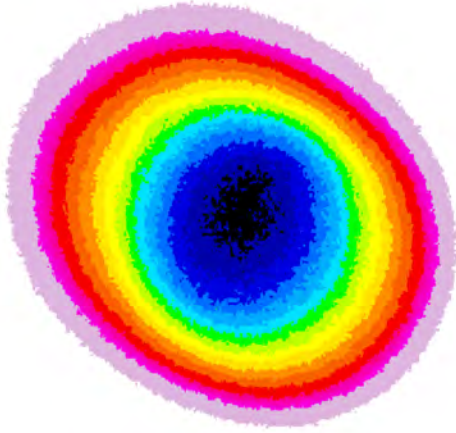
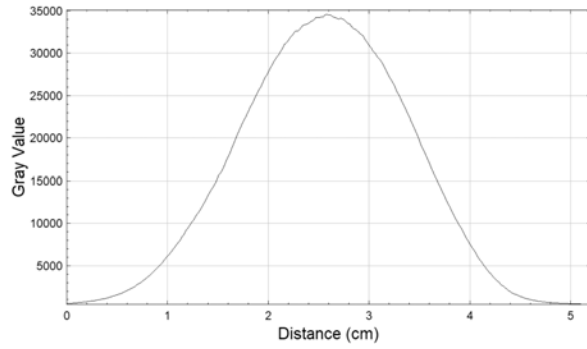


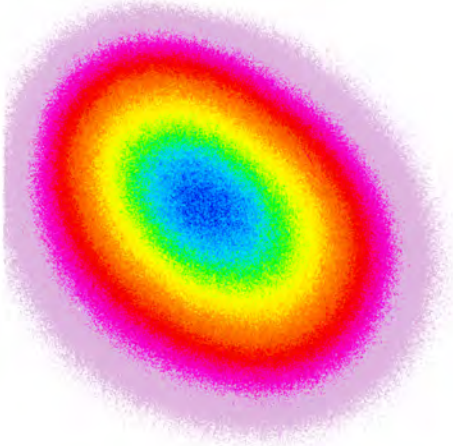
Figure 2.3: Images of the neutron beam inside the 90 m station. The color indicates the intensity of the beam at each position, with blue denoting the highest intensity, then green, yellow, orange, red, and pink in order of decreasing intensity. The intensity of each image is not directly comparable to the other; rather the position of the beam is the important take away from these images. (a) shows an image taken before alignment, where part of the central beam spot was not visible in the station. (b) shows an image taken after some realignment, so that the full beam spot was visible. The intersecting circle visible on each image is due to the structure of the collimation, with two different pieces of collimation inside and outside the circle (see Fig. 2.6). The beam images are each a few centimeters in diameter, and are not to scale here.



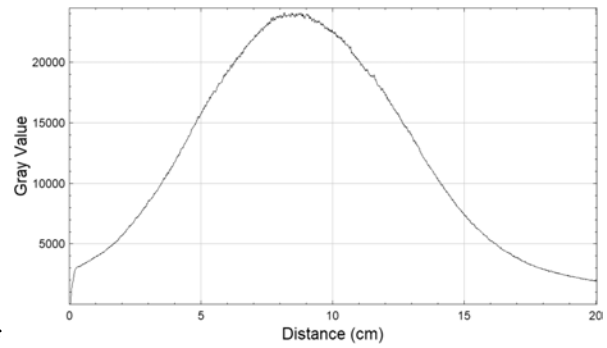
(a) Beam image at fission chamber location, downstream of Chi-Nu



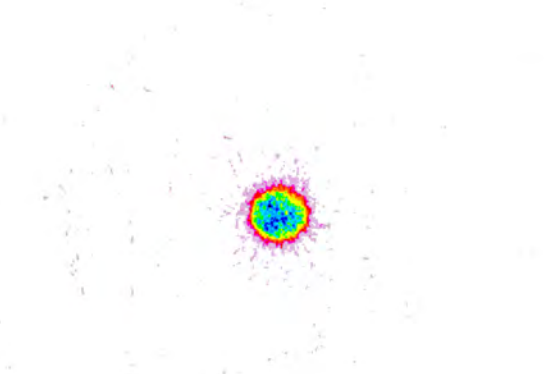
(b) horizontal projection of (a)



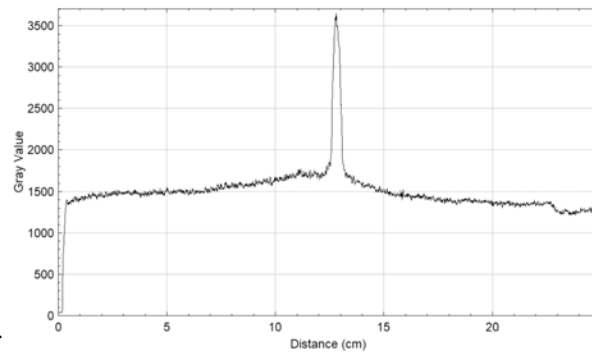
(c) Beam image outside 90 m station, upstream of tertiary collimation



(d) horizontal projection of (c)



(e) Beam image inside 90 m station, downstream of tertiary collimation



(f) horizontal projection of (e)

Figure 2.4: Beam images and their projections for three different locations on the 15L flight path. The images are not to scale. Note the different scales present in the projections (b),(d),(f).

2.4 Fission Chamber

A neutron flux monitor, also known as a fission chamber, was placed 28.4 m from the spallation target, just downstream of the Chi-NU/CoGNAC array. This monitor consists of ^{235}U and ^{238}U foils and an ionization chamber, which measures the fission fragments resulting from neutron-induced fission of $^{235,238}\text{U}$. A picture of the fission chamber is shown in Fig. 2.5.



Figure 2.5: The fission chamber located downstream of Chi-NU/CoGNAC, 28.4 m away from the spallation target. The signals from the chamber were routed into the Chi-NU/CoGNAC DAQ. Neutrons pass through the rectangular cutout behind the fission chamber on their way to the 90 m station.

2.5 Diamond Detectors

Two single-crystal chemical vapor deposited (sCVD) diamonds were used as active targets. These two diamonds were the same model, Cividec B8 Spectroscopic diamonds [56], with $4 \times 4 \text{ mm}^2$ active areas and 0.5 mm thickness. These semiconductor detectors feature good timing and energy resolution. They were installed 85.7 m away from the spallation target. The detectors were placed front-to-front, so that the beam interacted first with the backing, then with the active area of the upstream detector, followed by the active area and the backing of the downstream detector. A picture of the detectors installed in the 90 m station is shown in Fig. 2.6.

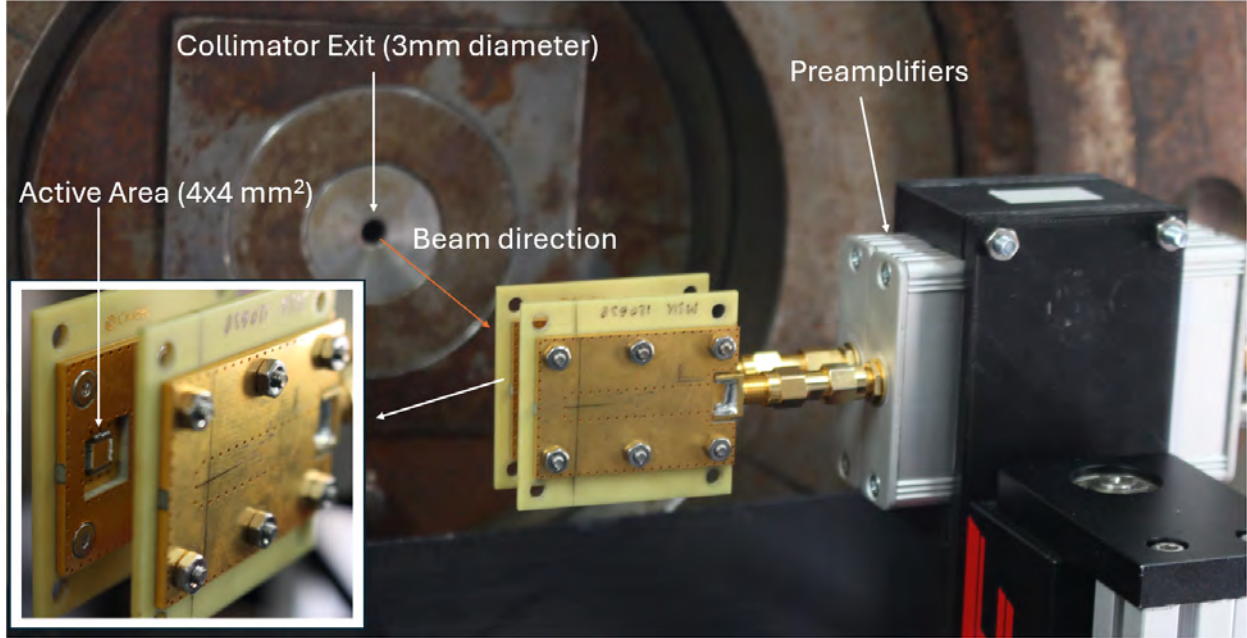


Figure 2.6: The Cividec B8 spectroscopic diamond detectors installed in the 90 m station, near the collimator. The inset shows the front face of the upstream detector, including the active area, which is $4 \times 4 \text{ mm}^2$ and 0.5 mm thick. Also visible are the amplifiers for each detector, placed in a holder attached to a two-dimensional translation stage.

2.5.1 Diamond Detector Position Optimization

The absolute neutron flux was not determined for the cross section measurements. Instead, data were normalized relative to previous (n,α) measurements at 14.1 MeV. However, it was still beneficial to improve the count rate in the diamond detectors by aligning them to maximize their overlap with the neutron beam. First, the diamond detectors were loaded into a holder, such that their active areas were opposite one another and aligned to within less than a millimeter. Then, the holder was loaded onto a two-dimensional translation stage with stepper motors in the horizontal and vertical directions relative to the beam axis, such that the diamond detectors could be moved precisely without needing to access the vault. The count rate was determined on a grid of positions, and the diamonds were placed at the position with the highest count rate for the duration of the experiment. A map of the various diamond positions and their count rates is shown in Fig. 2.7.

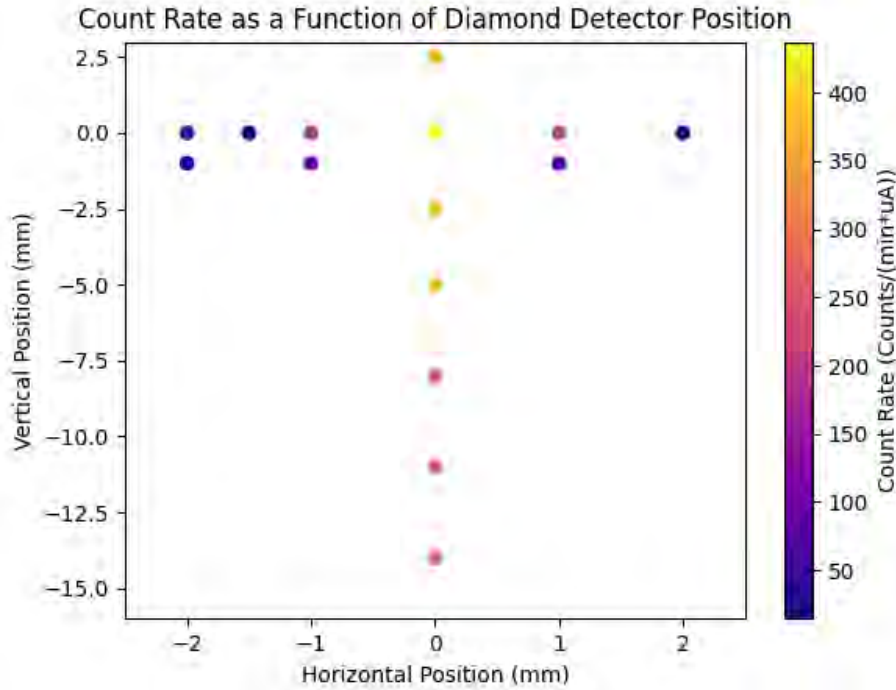


Figure 2.7: The count rate at various diamond detector positions, used to determine the location where the diamond detectors should be placed for the experiment. The origin in this plot is the position where the diamonds were placed in the experiment. The z axis scale shows the count rate at each location and was scaled to account for any fluctuations in beam current.

2.6 MoNA

The MoNA array is made from $2 \text{ m} \times 10 \text{ cm} \times 10 \text{ cm}$ individual bars of BC408 organic scintillator. Neutrons interact via nuclear collisions with the carbon and hydrogen nuclei within the bars, resulting in the generation of recoil protons and light ions. These will ionize other atoms and excite electrons of the nuclei in the material. As atoms de-excite, photons are produced, which propagate to the ends of the bar, where they are read out by a photomultiplier tube (PMT) on each end. The difference in photon arrival times allows the calculation of the neutron's position along the bar, taken as the x coordinate when placed horizontally, perpendicular to the beam. Using an array of these bars allows for high detection efficiency for fast neutrons. The identity of which bar the neutron hits provides the coordinate along the other two dimensions to measure the position of the interaction. Finally, measuring the time of the detection relative to a reference start time (such as T_0) allows for calculation of the neutron's kinetic energy.

The experimental setup within the 90 m station is shown in Fig. 2.8. Fifteen MoNA bars were set up downstream of the diamond detectors to measure the angular distributions of scattered neutrons and charged particles. A stack of 12 bars was set up 2.1 m from the collimator exit. Three

other bars were placed on the ground in front of the stack to measure larger angles. The angular distribution dataset is somewhat limited, since the primary method of identifying the reaction channels in the diamond detector depends on detecting the full energy of the reaction products. If all the reaction products are captured in the diamond, no angular distributions can be measured in MoNA. Thus, there is very little data where both a confident identification and an angular distribution can be obtained. There is some n-C total angular distribution data, and some angular distribution data that can be ascribed to a particular reaction channel, $^{12}\text{C}(n,n'+3\alpha)$.

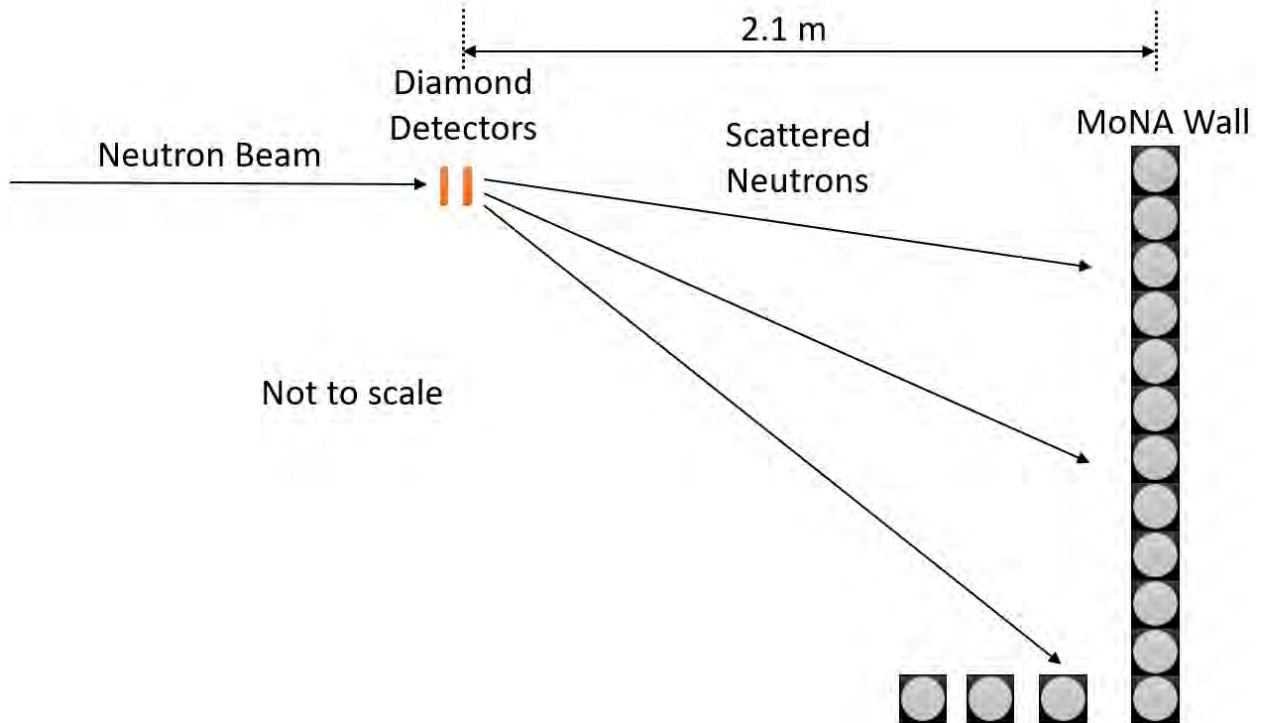


Figure 2.8: The experimental setup within the 90 m station. Two diamond detectors were placed 85.7 m from the spallation target. 15 MoNA bars- organic scintillator bars with a PMT on each side- were placed downstream to measure angular distributions of scattered particles. 12 bars were stacked in a wall, and three more were placed on the floor. The figure is not to scale.

2.7 Electronics and DAQ

The two diamond detectors were the same model, but their signals were processed differently.

- The upstream diamond's signals were routed through a Cividec CX spectroscopic shaping amplifier, which offers excellent energy resolution. This detector produced very large signals that were split (attenuating the signal by a factor of two) and sent into two different digitizer channels with different dynamic ranges ($2 V_{pp}$ and $0.5 V_{pp}$), in hopes that the smaller dynamic range could provide a zoomed-in view of the lower-energy events. However, the energy

resolution was sufficient to analyze the data on the larger dynamic range setting, and thus the channel with the smaller dynamic range was not used for the analysis. The signals from the upstream detector were still too large to fit in the $2 V_{pp}$ scale, so a rotary attenuator was used to attenuate the signal by an additional factor of five, for a total attenuation factor of 10. The signal rise time was about 80 ns.

- The downstream diamond’s signals were routed through a Cividec C6 fast charge amplifier, which can handle higher rates, and were sent directly into the digitizers with no attenuation on a $2 V_{pp}$ range. The signal rise time was about 8 ns. The data from the C6 amplifier would have benefited from offline waveform analysis, specifically in terms of energy resolution, but waveforms were not recorded due to data storage space constraints. However, it should be noted that the energy resolution of the CX spectroscopic amplifier is superior to that expected of the C6 even with waveform analysis.

The event rate for both detectors was far below the maximum rates that the detectors and DAQ could handle, and dead-time corrections were therefore negligible. The signals from the diamond detectors and the MoNA bars were sent to CAEN VX1730 digitizers (14 bit, 500 Megasamples/s), which have pulse shape discrimination (PSD) firmware. The specific settings for the DAQ can be found in [A](#), which shows the relevant portions of the configuration file used in digiTES, the command-line version of the proprietary CAEN CoPASS software [\[57\]](#). A diagram showing the signal paths for the diamond detectors is shown in [Fig. 2.9](#).

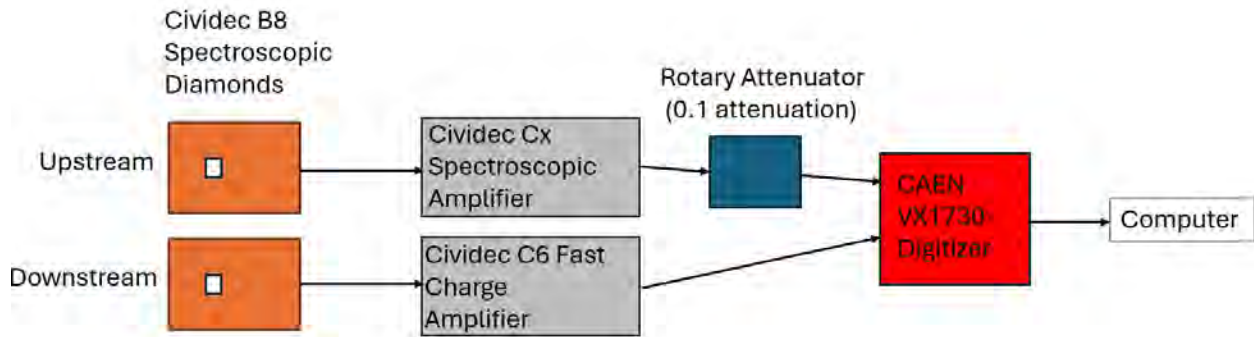


Figure 2.9: Wiring diagram showing the signal paths for the two diamond detectors. The detectors are the same model, but used different amplifiers. The signals from the upstream diamond detector were very large after passing through the spectroscopic amplifier, so a rotary attenuator was used. This channel was attenuated by a factor of 10. For simplicity, only channels that contributed to the data presented in this work are displayed.

Over the course of the experiment, various attenuation settings were used for both diamond detectors. However, only data taken with the final attenuation settings is presented in this work: 0.1 for the upstream detector and 1.0 for the downstream detector. The signals from the fission chamber were routed into the Chi-Nu/CoGNAC DAQ and data was shared after the experiment.

2.8 High Voltage

The diamond detectors and the PMTs for the MoNA bars all needed high voltage to function properly. The diamond detectors require a nominal voltage of +400 V. This was sufficient for the (newly purchased) upstream diamond detector. However, the downstream diamond detector had been used in previous experiments and potentially suffered radiation damage so that it produced far better signals when biased at +500 V. The PMTs for the MoNA bars were biased to a value between 1500 and 1800 V, determined by making the cosmic muon peak occur at 20 MeVee for each PMT.

A summary of useful information about the experiment is collected in Table 2.2.

Table 2.2: Summary of the detector characteristics and run details for the experiment.

Data collection time	253 hours	
Diamond detector thickness	0.5 mm each	
Diamond time resolution	1.0 ns	
Diamond Detector	Upstream	Downstream
Amplifier	Cx	C6
Attenuation setting	0.1	1.0
Detector bias	+400 V	+500 V
Distance from Target 4	85.69 m	85.70 m

Chapter 3

DATA ANALYSIS

3.1 Calibrations and Corrections

To extract meaningful physics, the raw outputs from the detectors needed to be converted to physical quantities. Thus, various calibrations were applied to the data. Much of this calibration was performed in the unpacker software, which takes the raw binary output and converts it into a ROOT [58] file format for easier data processing.

3.1.1 Diamonds

The difference between the time when the neutron is detected and the T0 signal gives the time of flight (ToF). The ToF in the diamond detectors was calibrated using the gamma flash, prompt gamma rays that travel from the spallation target. Since gamma rays travel at a known velocity (the speed of light, c), a precise measurement of the distance from the spallation target to the detector allows one to calibrate the ToF using this feature. This was accomplished by adjusting the time offsets in the unpacking software so that the produced ROOT files had the correct ToF. That procedure was sufficient to calibrate the downstream diamond detector. The upstream diamond required further time calibration due to a ToF drift at higher deposited energies. Since this could not be mapped to an analytic function, a manual transposition of the ToF was conducted at different energies so that the gamma flash occurs at the same ToF regardless of the energy deposited. A comparison of the upstream diamond spectra before and after the ToF drift correction is shown in Fig. 3.1. The calibrated ToF can be used to calculate the relativistic neutron kinetic energy. The highest energy neutrons at LANSCE are over 600 MeV, and have $\beta = v/c > 0.75$.

The diamond detectors also had their energy spectra calibrated, using the $^{12}\text{C}(n,\alpha)$ channel, which is easily identified due to its separation from the other channels. The reaction products (^9Be and an α particle) are often fully stopped in the diamond, so that they deposit the full kinetic energy of the neutron, minus 5.7 MeV due to the Q value (-5.701 MeV). Thus, we can use the neutron ToF to calculate the relativistic kinetic energy of the neutron, and subtract the Q value to find the energy deposited in the detector. Repeating this procedure at various energies yields a calibration curve, which can be used to correct the energy spectra. This operation was performed

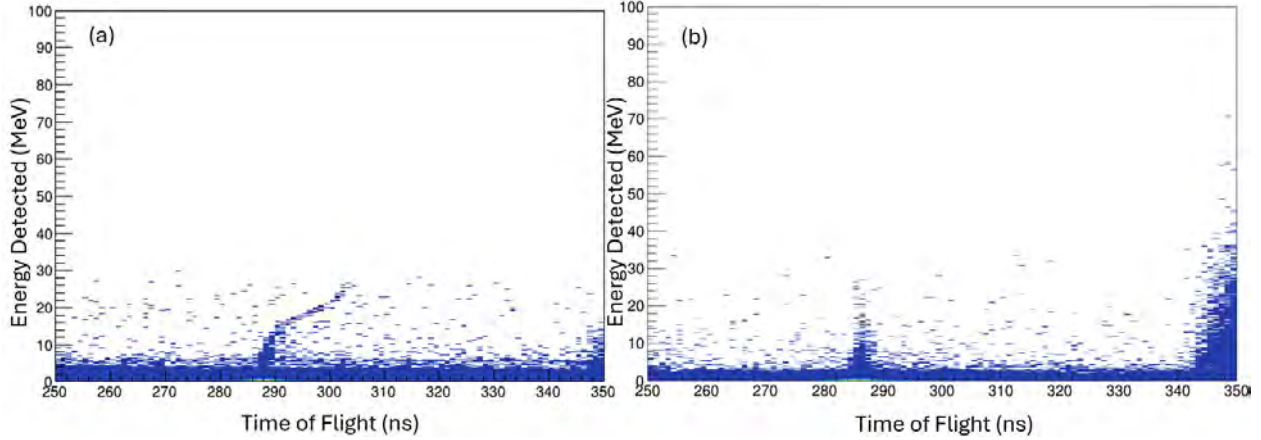


Figure 3.1: A comparison of the energy detected in the diamond vs. the ToF, before (a) and after (b) the ToF drift correction in the upstream diamond detector that made the gamma flash occur at the same ToF regardless of the energy deposited.

for all of the different attenuation settings, though only the data at the final setting was used for the rest of the analysis.

The upstream diamond detector featured a discontinuity in the data at 18 MeV, above which the detector response was non-linear. Again, the $^{12}\text{C}(n,\alpha)$ channel was used for the calibration. Starting from the semi-calibrated spectra (Fig. 3.2), in which the data below 18 MeV energy detected is calibrated, another calibration curve was produced using the same method as the initial energy calibration.

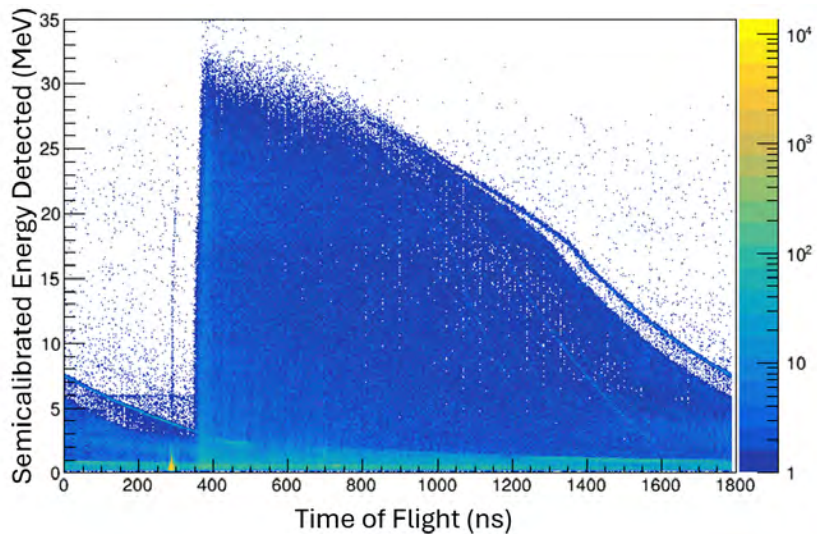


Figure 3.2: Semi-calibrated energy detected in the diamond detector plotted against ToF, for the upstream diamond detector. The energy detected is calibrated correctly below 18 MeV, but another calibration was needed above 18 MeV.

The fully calibrated energy detected vs. ToF plots for each diamond are shown in Fig. 3.3 and Fig. 3.4 for the upstream and downstream detectors, respectively. A further calibration was applied after the Q value reconstruction, and is described in Section 3.2.1.

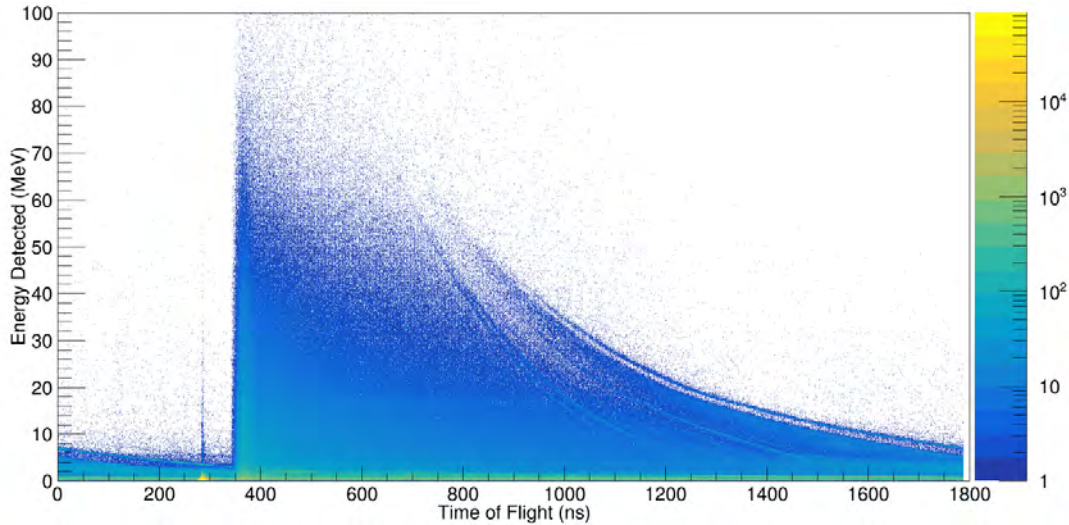


Figure 3.3: Energy detected in the diamond detector plotted against ToF, for the upstream diamond detector, after calibration.

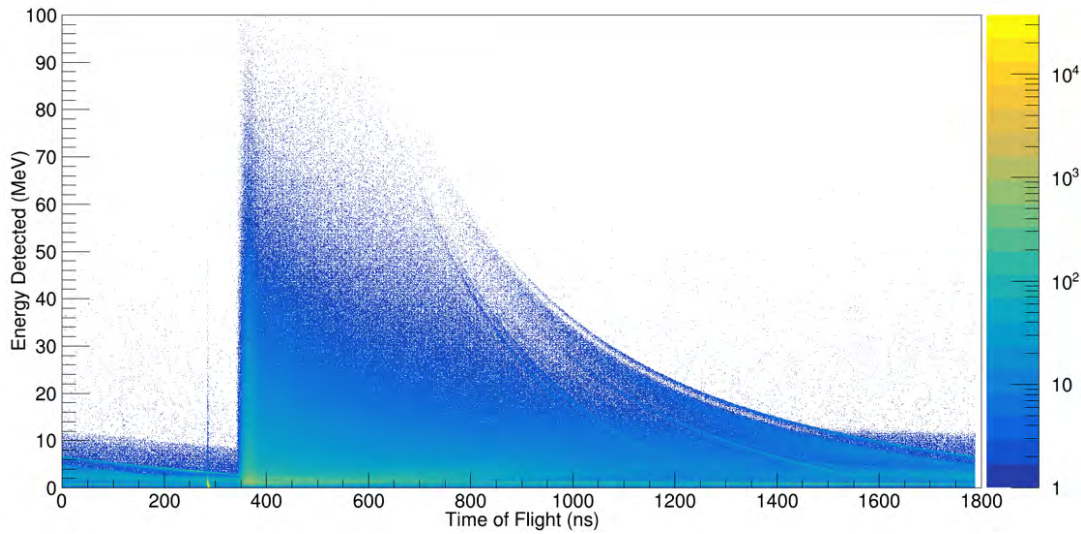


Figure 3.4: Energy detected in diamond detector plotted against ToF, for the downstream diamond detector, after calibration.

3.1.2 Fission Chamber

The fission chamber data was calibrated, with respect to time-of-flight, and this time-of-flight was used to reconstruct the kinetic energy of the neutrons in the fission chamber. A rough energy

calibration was performed, accurate enough that the smaller energy deposits produced by alpha particles and other light charged particles can be filtered out, leaving only events that are due to the neutron-induced fission fragments of interest. Thus, one obtains the number of induced fission events as a function of energy. Although the fission chamber contains both ^{235}U and ^{238}U foils, only the ^{235}U was used for the analysis. The fission chamber data before conversion to flux is shown in Fig. 3.5. The $^{235}\text{U}(n,f)$ cross section is a reference standard up to 200 MeV, and can be used to extract the neutron flux.

Using $^{235}\text{U}(n,f)$ cross section ($\sigma_{n,f}$) reference data [59], with a linear interpolation to find the cross sections for our data bins, the flux (Φ_{fc}) can be obtained:

$$\Phi_{fc} = \frac{N_{fc}}{\sigma_{n,f}} \quad (3.1)$$

where N_{fc} is the counts in a given bin in the fission chamber data. This energy dependent flux was used for the flux normalization for the cross sections. The neutron flux calculated from the fission chamber is shown in Fig. 3.6, and is compared with a flux distribution simulated with MCNP.

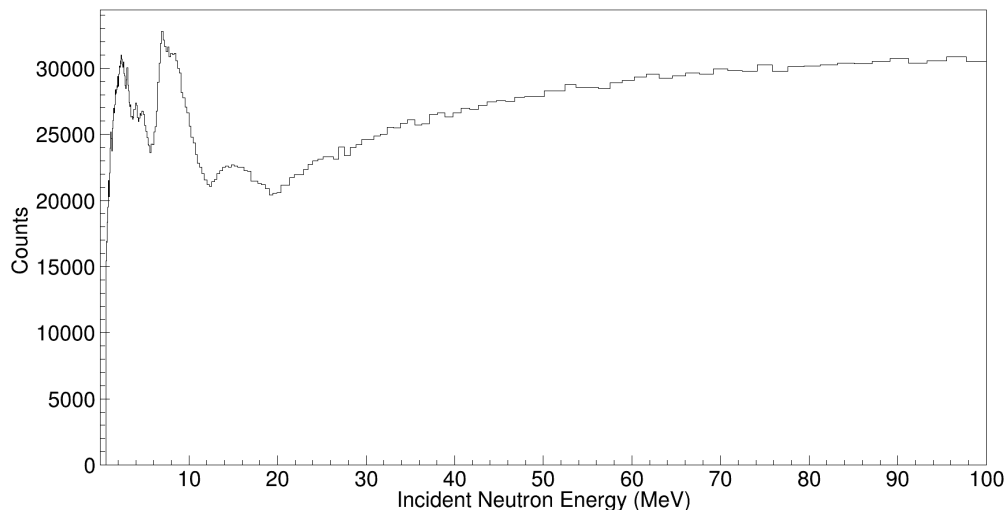


Figure 3.5: The counts measured in the fission chamber as a function of the incident neutron energy. This is the raw output, before the $^{235}\text{U}(n,f)$ cross section standard is used to obtain the neutron flux.

3.1.3 Beam Images

The beam images were processed with an Amersham Typhoon laser scanner [55]. The gray value, a measure of the radiation received, and hence a measure of the beam intensity, was automatically calibrated by the scanner, so that the maximum gray value observed was set to 1.0 for each image individually. This is beneficial for creating images with good contrast and gradient, but prevented them from being used to measure attenuation in the beam. No further calibration was performed on

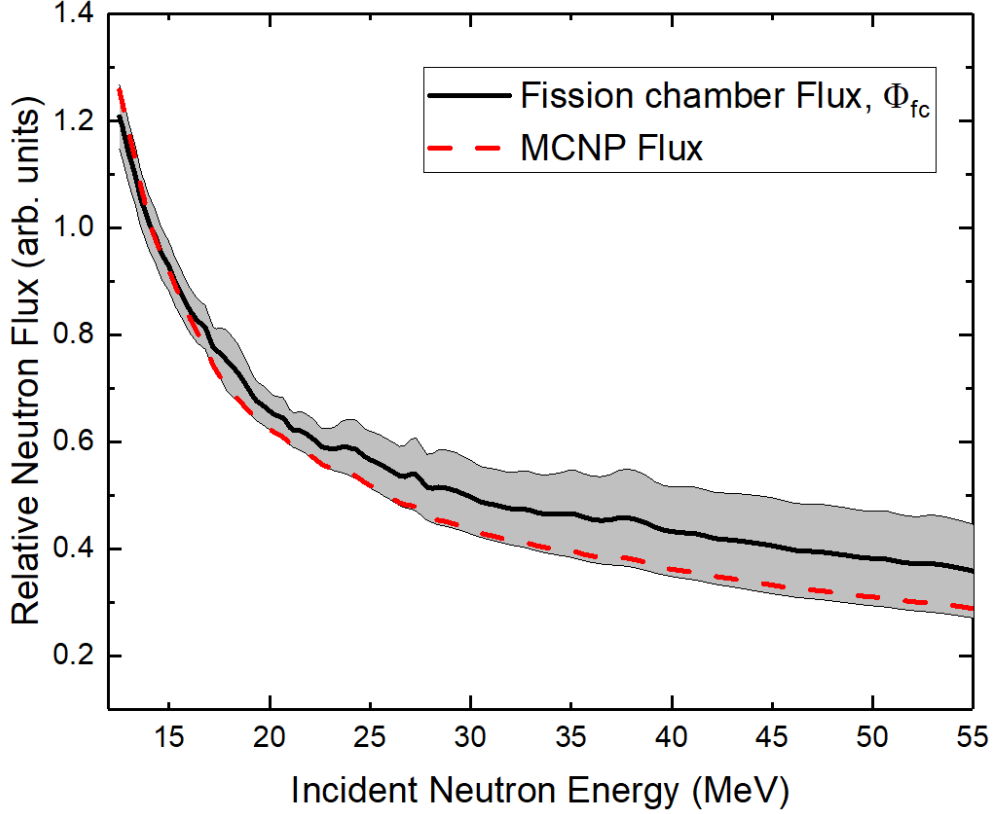


Figure 3.6: The relative neutron flux distribution obtained from the fission chamber, using the $^{235}\text{U}(n,f)$ cross section to convert the counts into flux (black curve) and using an MCNP simulation (red curve). The uncertainty in the flux is shown in the error band (gray shading). Both the flux obtained with the fission chamber and the MCNP flux were normalized at 14.1 MeV.

the images. The digital phosphors output from the scanner were analyzed in ImageJ [60], a digital processing program. The color plots shown here are obtained from a 16-color inverted lookup table. Also presented are projections of the beam spots: Both horizontal and vertical projections were analyzed, but only horizontal projections are shown here for brevity. These projections have the benefit of quantifying the extent of the beam. This also did not need to be calibrated; instead, the processed image is 1:1 with the physical image.

3.2 Event Selection

3.2.1 Q value calculation

For a reaction in which the reaction products deposit all of their kinetic energy in the diamond, one can reconstruct the Q value of the reaction:

$$Q = E_d - E_n \quad (3.2)$$

where E_d is the energy deposited and E_n is the incident neutron energy. Thus, for this method of identification, we are limited to looking at reaction channels and neutron energies where full energy deposition of the reaction products occurs, namely reactions where there are only charged particles in the exit channel, and at beam energies low enough that the charged particles do not escape. The one exception to this is the $^{12}\text{C}(n,n'+3\alpha)$ channel, which even though it has a neutron in the exit channel, we can identify some events confidently as this reaction channel since there are no other Q values nearby. However, although some events can be confidently identified as belonging to this reaction, at higher energies the $^{12}\text{C}(n,n'+3\alpha)$ channel underlies peaks, which belong to other reaction channels, and other continuum processes, and thus an exclusive cross section could not be determined from this channel.

For the other identified channels, sharp peaks arise in the reconstructed Q-value spectrum that correspond to different reaction channels. At less negative reconstructed Q values, identification is very simple, since there are few candidate reactions. At more negative reconstructed Q values, identification is complicated by the possibility of more reaction channels. Identification is further complicated by the possibility of producing a daughter nucleus in an excited state, so that the reconstructed Q value is offset by the energy of the gamma ray, which is typically not detected in the same event window. However, if the identity of a peak can be determined, it allows determination of an exclusive cross section, not just for producing a given daughter nucleus, but for populating a particular energy level of the daughter nucleus.

Reaction channels were identified by comparing our results to the NNDC's Q Value calculator [61], combined with the level scheme data for the relevant daughter nuclei, which include ^9Be , ^{12}B , ^{11}B , ^{10}B , and ^{10}Be . Reconstructed Q value spectra are shown at two different incident neutron energy ranges in Figs. 3.7 and 3.8 to illustrate the various reaction channels present. Note that neutron reactions on ^{12}C producing only charged reaction products have negative Q values.

The energy and time calibration described previously was sufficient for the channels for which cross sections were obtained in this work, as well as those observed in previous studies, namely [13]. To identify channels at more negative reconstructed Q values, another calibration step was required due to a non-linearity in the data affecting the Q value reconstruction. The origin of this non-linearity could be due to an inherent quality of the diamond detector operated with the Cx spectroscopic amplifier, or an issue in the neutron kinetic energy reconstruction or energy calibration in the analysis. Published pulse-height spectra for higher-energy neutrons on diamond do not exist, which otherwise would be helpful in deciphering the reconstructed Q value spectra. To calibrate the reconstructed Q values, the literature Q values of the confidently identified peaks in the data (everything up to $^{12}\text{C}(n,^3\text{He}_0)^{10}\text{Be}$ in Table 3.1) were plotted against their centroids in the data, and a linear calibration was performed. This shifted the reconstructed Q values of unknown peaks closer to their literature values, which helped to identify the next few peaks shown in Table 3.1, up through $^{12}\text{C}(n,t_3)^{10}\text{B}$. This procedure was not sufficient for the peaks observed at the most negative reconstructed Q values, which have more candidate reactions possible, and thus

Table 3.1: Reaction channels observed in the diamond detector. The literature Q values were used to identify the reaction channel. The thresholds helped confirm some identities.

Reaction Channel	Literature Q Value (MeV)	Literature Threshold (MeV)	Note
$^{12}\text{C}(n,\alpha)^9\text{Be}$	-5.702	6.182	
$^{12}\text{C}(n,n'+3\alpha)$	-7.274	7.886	
$^{12}\text{C}(n,p_0)^{12}\text{B}$	-12.587	13.646	
$^{12}\text{C}(n,p_1)^{12}\text{B}$	-13.540	14.599	Overlaps slightly with (n,d ₀)
$^{12}\text{C}(n,d_0)^{11}\text{B}$	-13.732	14.887	Overlaps slightly with (n,p ₁)
$^{12}\text{C}(n,p_2)^{12}\text{B}$	-14.261	15.319	
$^{12}\text{C}(n,p_3)^{12}\text{B}$	-15.208	16.267	Cannot be distinguished from (n,p ₄)
$^{12}\text{C}(n,p_4)^{12}\text{B}$	-15.309	16.369	Cannot be distinguished from (n,p ₃)
$^{12}\text{C}(n,d_1)^{11}\text{B}$	-15.857	17.012	
$^{12}\text{C}(n,d_2)^{11}\text{B}$	-18.177	19.332	
$^{12}\text{C}(n,d_3)^{11}\text{B}$	-18.752	19.907	Cannot be distinguished from (n,t ₀)
$^{12}\text{C}(n,t_0)^{10}\text{B}$	-18.929	20.521	Cannot be distinguished from (n,d ₃)
$^{12}\text{C}(n,^3\text{He}_0)^{10}\text{Be}$	-19.467	21.105	
$^{12}\text{C}(n,t_1)^{10}\text{B}$	-19.647	21.239	
$^{12}\text{C}(n,d_4)^{11}\text{B}$	-20.474	21.629	Cannot be distinguished from (n,d ₅) or(n,t ₂)
$^{12}\text{C}(n,d_5)^{11}\text{B}$	-20.524	21.679	Cannot be distinguished from (n,d ₄) or(n,t ₂)
$^{12}\text{C}(n,t_2)^{10}\text{B}$	-20.669	22.261	Cannot be distinguished from (n,d ₄) or(n,d ₅)
$^{12}\text{C}(n,d_6)^{11}\text{B}$	-21.018	22.173	Cannot be distinguished from (n,t ₃)
$^{12}\text{C}(n,t_3)^{10}\text{B}$	-21.083	22.675	Cannot be distinguished from (n,d ₆)

need to be calibrated more precisely than this. The quality of the identification can be broken into three regions:

Region 1 ($Q > -18.2$ MeV, up to and including the (n,d₂) reaction peak), in which the identification of the peaks is quite clear, with the exception that the (n,p₃) and (n,p₄) peaks cannot be distinguished with our resolution. A previous study [13], perhaps with slightly better resolution, fit (n,p₃+p₄) with two peaks, using the expected branching ratio from a reaction code calculation, but this has not yet been attempted with this dataset.

Region 2 ($-18.7 > Q > -21.0$ MeV), in which peaks are fairly well calibrated, but due to more possible reaction channels, could not be attributed to a single reaction. The only exceptions to this are the $^{12}\text{C}(n,^3\text{He}_0)^{10}\text{Be}$ and $^{12}\text{C}(n,t_1)^{10}\text{B}$ channels, for which peaks can be solely ascribed.

Region 3 ($Q < -21.0$ MeV) , in which the non-linearity of the calibration, combined with the onset of many more possible reactions, have made it impossible to identify the peaks in this region so far. Each unknown peak has at least four possible reactions that may contribute to it.

Table 3.2: Possible identifications for five unidentified peaks observed in the diamond detector. The reconstructed Q value is obtained after the additional calibration step discussed in Section 3.2.1. Since this calibration varies slightly based on the incident neutron energy range over which this calibration is performed, the reconstructed Q values listed here were obtained using a 30-33 MeV incident neutron energy range. The threshold was obtained based on the minimum E_n where the peak was observed, less 2 MeV, similar to where other channels became visible above threshold.

Reconstructed Q Value (MeV)	Threshold (MeV)	Possible Identities (Literature Q Value (MeV))
~ -22.5	24.5	$^{12}\text{C}(\text{n},\text{d}_9)^{11}\text{B}$, $^{12}\text{C}(\text{n},\text{t}_4)^{10}\text{B}$, $^{12}\text{C}(\text{n},\text{d}_0+\alpha_0)^7\text{Li}$, $^{12}\text{C}(\text{n},\text{p}+\alpha)^8\text{Li}$
~ -22.93	26.0	$^{12}\text{C}(\text{n},^3\text{He}_1)^{10}\text{Be}$, $^{12}\text{C}(\text{n},\text{d}_{10})^{11}\text{B}$, $^{12}\text{C}(\text{n},\text{d}_{11})^{11}\text{B}$
~ -23.49	26.0	$^{12}\text{C}(\text{n},\text{t}+\alpha_0)^6\text{Li}$ (-23.39), $^{12}\text{C}(\text{n},\text{d}_{12})^{11}\text{B}$ (-23.552), $^{12}\text{C}(\text{n},\text{p}_1+\alpha_1)^8\text{Li}$ (-23.569), $^{12}\text{C}(\text{n},\text{d}_{13})^{11}\text{B}$ (-23.605), $^{12}\text{C}(\text{n},\text{t}_5)^{10}\text{B}$ (-23.703)
~ -25.10	29.5	$^{12}\text{C}(\text{n},2\alpha+\text{d}+\text{t})$ (-24.864), $^{12}\text{C}(\text{n},\text{t}_{10})^{10}\text{B}$ (-24.954), $^{12}\text{C}(\text{n},\text{t}+\text{d}_0)^8\text{Be}$ (-24.956), $^{12}\text{C}(\text{n},\text{p}+\text{d}_0)^{10}\text{Be}$ (-24.961), $^{12}\text{C}(\text{n},\text{d}_{18})^{11}\text{B}$ (-25.004), $^{12}\text{C}(\text{n},\text{t}_{11})^{10}\text{B}$ (-25.058), $^{12}\text{C}(\text{n},\text{d}_{19})^{11}\text{B}$ (-25.182)
~ -25.79	30.5	$^{12}\text{C}(\text{n},\text{t}+\alpha_1)^6\text{Li}$ (-25.576), $^{12}\text{C}(\text{n},^3\text{He}_4)^{10}\text{Be}$ (-25.647), $^{12}\text{C}(\text{n},^3\text{He}_5)^{10}\text{Be}$ (-25.731), $^{12}\text{C}(\text{n},\text{t}_{13})^{10}\text{B}$ (-25.804), $^{12}\text{C}(\text{n},\text{t}_{14})^{10}\text{B}$ (-25.933)

Table 3.1 lists the peaks that were identified from our experiment, while Table 3.2 lists those that have not yet been identified. The reconstructed Q values of the unidentified peaks were determined based on their calibration from 30-33 MeV incident neutron energy. This calibration varies with energy, so the reconstructed Q value may deviate from what is presented in the table in different incident neutron energy ranges. A detector with better energy and/or time resolution may be able to shed more light on these channels, but would need to be significantly improved since in many cases these reactions have very similar Q values. Notably, the states observed in the daughter nucleus are not only from the primary band, as multiple states are observed that correspond to other bands. Thus, the labeling of excited states (1st, 2nd, 3rd, etc.) refers to the ordering of the overall levels, not just that of the primary band.

From the Q-value spectra, the $^{12}\text{C}(\text{n},\alpha)^9\text{Be}$ events can be determined by a simple 1-D gate, since there is virtually no background. For the other channels, which sit on a background due to other reaction channels, fitting was required to extract the counts at each energy. The HDTV

fitting code [62] was used to fit the peaks with Gaussian distributions and a linear background.

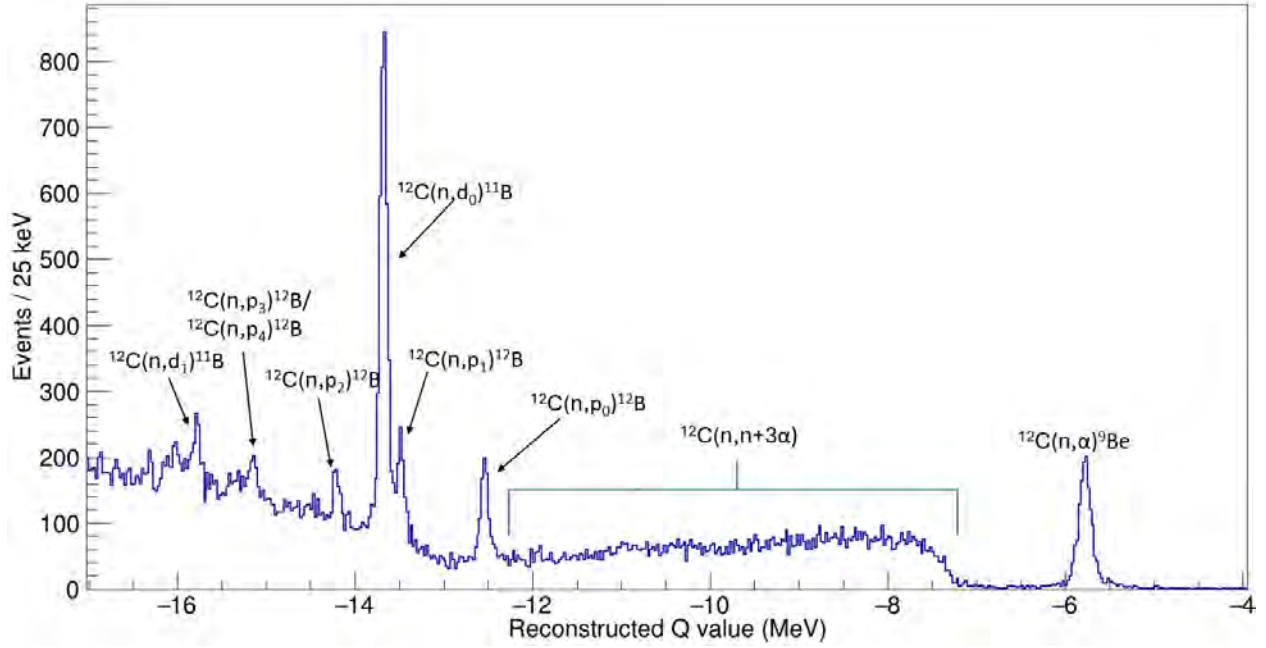


Figure 3.7: Reconstructed Q-value spectrum for 19 MeV neutrons for the upstream detector. The sharp peaks correspond to reactions with only charged particles in the exit channel. The first four peaks from the right were studied in this work: $^{12}\text{C}(n,\alpha)^9\text{Be}$, $^{12}\text{C}(n,p_0)^{12}\text{B}$, $^{12}\text{C}(n,p_1)^{12}\text{B}$, and $^{12}\text{C}(n,d_0)^{11}\text{B}$.

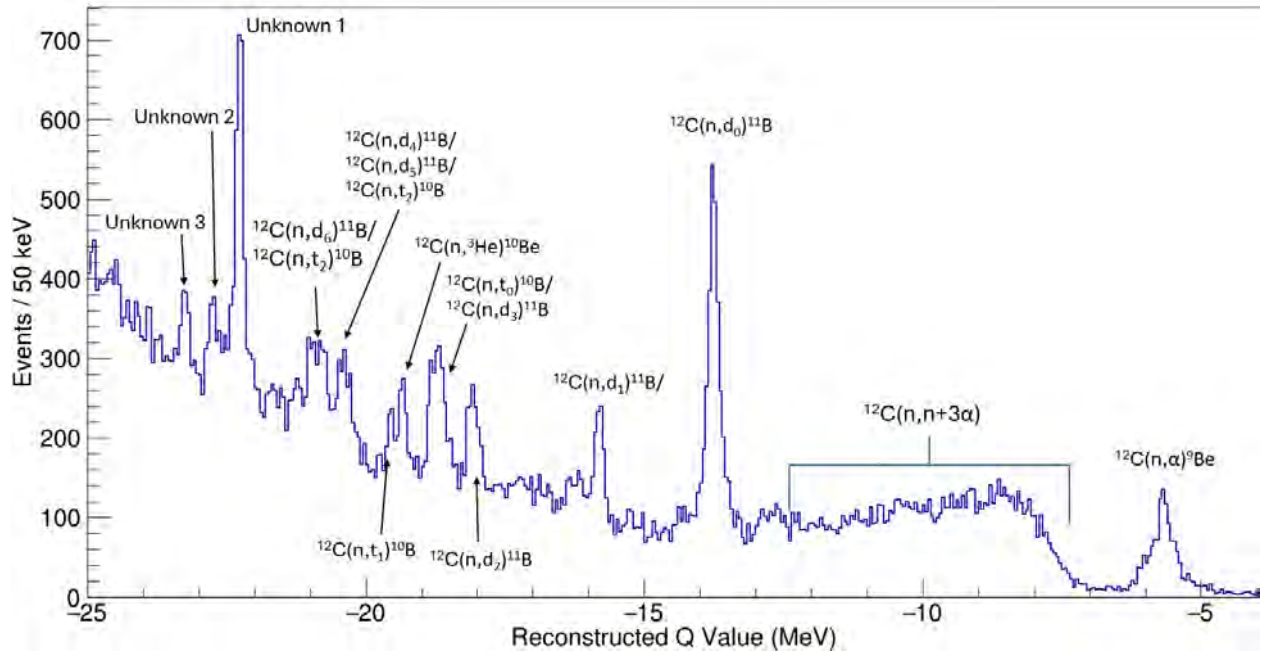


Figure 3.8: Reconstructed Q-value spectrum for 27-30 MeV neutrons for the upstream detector.

3.3 Background subtraction

Assuming that the background does not exhibit sharp changes in shape, using a linear background in our fit effectively subtracts background events with the same reconstructed Q value as the reactions of interest. An example of a fit performed with HDTV is shown in Fig. 3.9.

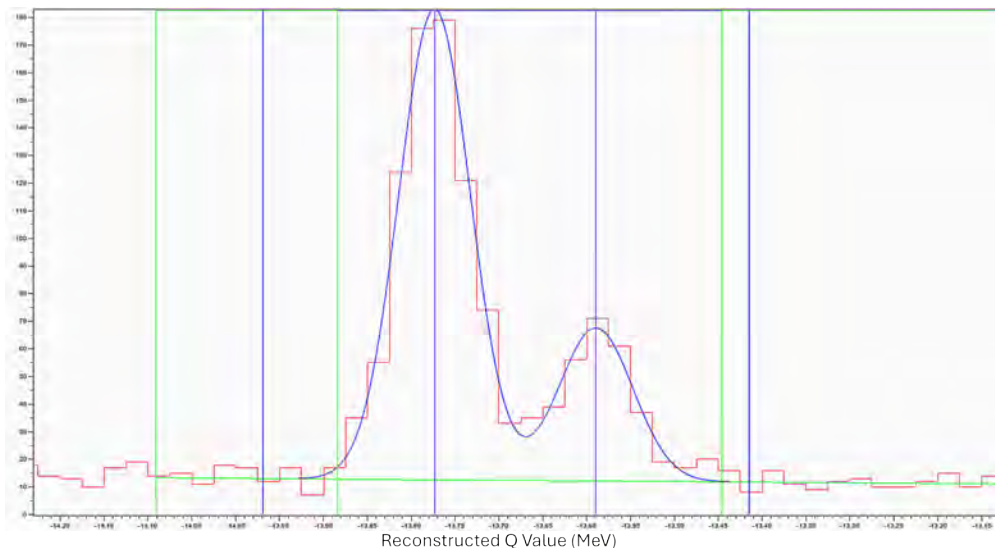


Figure 3.9: Example of peak fitting using HDTV. The red histogram is experimental data at $E_n = 20.37$ MeV, zoomed in on the (n,d_0) (left) and (n,p_1) (right) peaks. The peaks are fit with Gaussian distributions (blue curves) and a linear background (green horizontal line).

3.3.1 External sources of background

The small size of the diamond detector eliminates much of the external background, which includes cosmic muons, secondary light charged particles, and neutrons.

Cosmic muons

Cosmic muons primarily travel vertically through the atmosphere at approximately 1 muon per cm^2 at sea level. Correcting for the higher muon flux at the elevation of Los Alamos, this is closer to 1.8 muons per cm^2 . Since the diamond detectors are placed perpendicular to the neutron beam, the vertical muon flux passes through an area of 0.5 mm (thickness) x 4 mm (horizontal length) = 2 mm^2 . Thus, we have

$$\frac{1.8 \text{ muons}}{\text{cm}^2 \text{ minute}} \times 2 \text{ mm}^2 \times \frac{1 \text{ cm}^2}{100 \text{ mm}^2} = 3.6 \times 10^{-2} \text{ muons per minute} \quad (3.3)$$

Compared to the diamond event rate of roughly 18000 counts per minute from the neutron beam, the muon event rate is negligible.

Light charged particles

Light charged particles are produced in the spallation target. However, these are swept out of the flight path with a magnet and are also attenuated through air, so that none were observed experimentally. Since the beam is not kept under vacuum, there is a small probability of interactions with air producing charged particles that are detected in the diamond. A few of the events to the right of the (n,α) peak in Fig. 3.7 may be due to the $^{14}\text{N}(n,p)^{14}\text{C}$ reaction, but the number of these events is less than 1% that of the events in the (n,α) peak.

Background Neutrons

Thermal neutrons do not have sufficient energy to trigger the detectors above threshold. Previous MoNA experiments at LANSCE dealt with another source of background due to neutrons scattering from the collimator, resulting in a spray of neutrons around the well-defined beam spot, referred to colloquially as “halo neutrons.” These neutrons have similar ToF and hence incident neutron energies as those in the central beam spot, but have much greater angular dispersion. The diamond detectors were placed so that there was a small air gap between them and the collimator exit. This, combined with the small active area of the detector, ensures that the halo neutrons have minimal chances of reaching the detector. Any halo neutron that does reach the diamond must have a trajectory very similar to that of a beam neutron, and thus will have minimal differences in the number of target nuclei seen and the detection efficiency of charged particles produced in a reaction.

3.3.2 Internal sources of background

There are several neutron interactions with the detector that can complicate data analysis, sometimes shifting the reconstructed Q values. Reaction products from these interactions can include gamma rays, charged particles, and neutrons.

Gamma rays

The peak identification by Q value of the various excited states is possible only because the gamma rays from the decay of the excited state are not typically detected in the same event window as they are created. These gamma rays can deposit up to their full energy within the diamond, but are typically not detected in coincidence due to the lifetime of the states. If the gamma ray is detected, and deposits any of its energy in the diamond, this affects the Q value reconstruction in the event window in which it occurs. However, these are uncorrelated, so there should not be any particular peak that gains or loses a disproportionate number of events. In particular, the decay of excited states of ^{10}B , ^{11}B , and ^{12}B can produce gamma rays with energies up to 9 MeV. Similarly, the beta decay of the ground state of unstable nuclei created in the diamond produces beta particles whose detection could negatively affect the Q value reconstruction. Such nuclei include ^{12}B , ^9Li , ^8B , ^6He , ^8Li , ^{10}C , ^{11}C , ^7Be , and others in this region. Again, these are uncorrelated and did not significantly affect our ability to identify the peaks.

Escaping Charged particles

Some higher-energy events produce charged particles with sufficient kinetic energy to escape the detector. This leads to a low-energy-deposition tail for each peak, which contributes to a somewhat linear background. Simulations were performed to estimate this effect and correct for it, since in a thicker detector these events would be recorded in the proper peak.

Reactions with Neutrons in the exit channel

More significant background arises from neutron interactions whose reaction products do not deposit their full kinetic energy in the diamond. One class of such interactions are those that have a neutron in the exit channel. Examples of such interactions are included in Table 3.3. The charged particles produced in these reactions may deposit their energy, but the neutron typically escapes without depositing energy in the diamond. Thus, these continuum events do not create a sharp peak in the reconstructed Q value spectrum.

Table 3.3: Continuum channels that contribute to internal background. The literature Q value [61] represents the Q value for each reaction channel, and hence the maximum reconstructed Q value. Of the many possible continuum reactions, those listed here have some of the largest Q values, and thus have the greatest contributions to the background.

Reaction Channel	Literature Q Value (MeV)	Literature Threshold (MeV)
$^{12}\text{C}(n,n'+3\alpha)$	-7.274	7.886
$^{12}\text{C}(n,n'+p)^{11}\text{B}$	-15.956	17.299
$^{12}\text{C}(n,2n)^{11}\text{C}$	-18.720	20.295
$^{12}\text{C}(n,n'+p+\alpha)^7\text{Li}$	-24.621	26.692
$^{12}\text{C}(n,n'+d)^{10}\text{B}$	-25.186	27.305
$^{12}\text{C}(n,n'+p+t+2\alpha)$	-27.088	29.367
$^{12}\text{C}(n,n'+t)^9\text{B}$	-27.366	29.668
$^{12}\text{C}(n,n'+d+\alpha)^6\text{Li}$	-29.647	32.142

Neutron elastic scattering

Above 12 MeV, elastic scattering of neutrons off carbon – $^{12}\text{C}(n,n)^{12}\text{C}$ – does not deposit sufficient energy in the detector to interfere with the $^{12}\text{C}(n,\alpha_0)^9\text{Be}$ reaction. However, it does interfere with the (n,p_0) , (n,p_1) , and (n,d_0) channels, and contributes to the linear background for these channels. The corresponding maximum recoil carbon energy is given by:

$$(n, n) : E_R = \frac{4A}{(1+A)^2} E_n = \frac{48}{169} E_n \quad (3.4)$$

and the maximum reconstructed Q-value for $^{12}\text{C}(n,n)^{12}\text{C}$ events is

$$(n, n) : Q_{\max} = E_R - E_n = -0.716 E_n \quad (3.5)$$

The $^{12}\text{C}(n,n'+\gamma)^{12}\text{C}$ channel has similar reconstructed Q values, but one must consider the 4.44 MeV γ ray:

$$(n, n' + \gamma) : \quad E_R = \frac{4A}{(1+A)^2}(E_n - E_x) = \frac{48}{169}(E_n - 4.4 \text{ MeV}) \quad (3.6)$$

$$(n, n' + \gamma) : \quad Q_{\text{max}} = E_R - E_n = -0.716 E_n - 1.26 \text{ MeV} \quad (3.7)$$

Fig. 3.10 shows the incident neutron energy ranges at which each background channel is relevant, for the reactions studied in this work.

Population of Neutron-Unbound States

It is also possible to populate neutron-unbound states of the daughter nucleus. When such a state is populated, almost immediately the nucleus emits a neutron. If the neutron escapes without depositing its kinetic energy, the Q value reconstruction will not be correct. Such events were not observed experimentally, but explicit observation was not expected since they would not create a sharp peak. TALYS [50] calculates these events to be possible, in nonnegligible amounts. Population of neutron-unbound states does not affect the four channels for which cross sections were obtained, as the channels presented in this work have less negative reconstructed Q values.

Reactions with ^{13}C

The diamonds in these detectors are natural carbon, and thus are 1.06% ^{13}C . The total cross section for ^{13}C is similar to that of ^{12}C . Thus, about 1% of the total interactions in the diamond are due to n - ^{13}C . In a previous study using the same detectors [15], the $^{13}\text{C}(n,\alpha_0)^{10}\text{Be}$ channel was observed up to 11.6 MeV. Neither this channel nor other ^{13}C channels were identified in the present work. We believe that these interactions contribute to the background. There are some peaks observed in the data where a confident identification has not been made, but it would have to be a particularly large cross section or resonance in ^{13}C to make up for the small fraction of ^{13}C in the diamond. Therefore, it is assumed that all peaks observed in the data correspond to interactions with ^{12}C .

Wraparound neutrons A somewhat unique source of background exists at LANSCE, due to the white neutron source. The accelerator produces monoenergetic protons at 800 MeV. When each pulse of protons impinges on the spallation target, neutrons are produced with a continuous distribution of energies. There is no velocity/momentum filter like there are at beam facilities that employ projectile fragmentation. Thus, every neutron that is produced with the correct solid angle reaches the detector, besides those that are attenuated in the air. Since the micropulses are spaced fairly close together, the slowest moving neutrons of a given micropulse arrive later in time than the fastest moving neutrons of the next micropulse. These slow neutrons are referred to as “wraparound neutrons”. They were observed in previous MoNA experiments at LANSCE. With the improved energy resolution of the diamond detectors compared to the MoNA bars, not only the first generation wraparound (from the micropulse directly before), but also the second generation

Interplay of background channels with analyzed channels

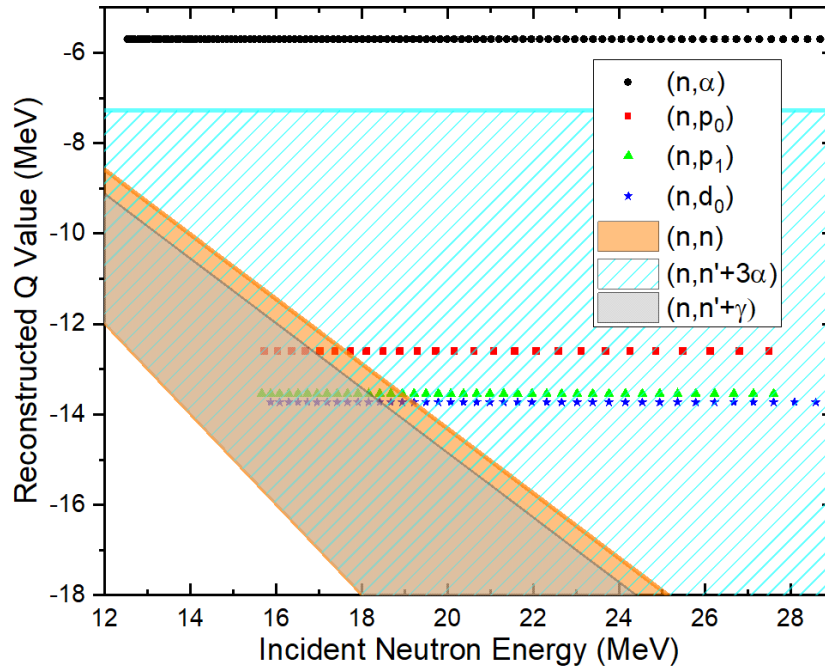


Figure 3.10: Diagram showing the n - ^{12}C background channels that have the greatest impact on the data studied in this work. The data points correspond to the incident neutron energies for which cross sections were determined for each reaction channel studied in this work, while the shaded regions correspond to those where each source of background is present. Note that for the reactions studied in this work, the reconstructed Q value is constant as a function of incident neutron energy. The white region in the bottom left is due to the fact that reconstructed Q values cannot be larger in magnitude than the incident neutron energy.

wraparound (from the micropulse before that) was observed. Third, fourth, and further generations of wraparound are likely present in the data as well, but with reduced impact on the analysis.

These wraparound neutrons have lower maximum energy deposition than the faster moving neutrons of a given pulse, but their ToF cannot be distinguished from faster neutrons that deposit relatively little energy. Due to the kinematics of the channels of interest, these wraparound neutrons produce very negative reconstructed Q values, and thus do not interfere with any of the reaction channels that we studied.

The wraparound neutron background does set a lower limit on the incident neutron energy for which cross sections can be determined. This cutoff is either 9 MeV (where the gamma flash of the next pulse occurs) or 8.4 MeV (where the fastest neutrons of the next pulse arrive). This is a tradeoff: one benefit of this study is the longer flight path, which allows for greater resolving power by spacing out the arrival times of neutrons of different energies. However, the longer the flightpath, the higher the wraparound neutron energy, so that lower energy cross sections could be

determined if a shorter flight path was used. Since the low energy cross sections for the channels of interest have already been well studied [12, 15, 36, 38, 42, 45], this is an acceptable loss. In fact, due to the higher energy focus of this study, the decision was made to focus on the higher neutron energies. Thus, the lowest neutron energies at which cross sections were determined in our study are at $E_n = 12.53$ MeV, corresponding to neutrons with $\text{ToF} = 1800$ ns, i.e. we focus on the content of each micropulse before the next micropulse begins. For future experiments, perhaps an intermediate flightpath length could be used, wherein the wraparound neutron background is lower, but the resolving power is still better than that of a very short flightpath.

3.4 Modeling and Simulation

3.4.1 Charged Particle Detection Efficiency

The diamond detectors have a small thickness, making it quite possible at higher energies that the light ions created in the reactions of interest will escape, and thus not deposit their full energy. Since the event selection depends on an accurate reconstructed Q value, events in which the reaction products do not deposit their full energy will not show up in the correct peak, and the cross section will be underestimated. To correct for this, simulations were run with `MENATE_R` [21] to calculate the efficiency of detecting the charged reaction products.

Each reaction channel was simulated separately to simplify the simulation. For each channel, the probability that the reconstructed Q value shows up in the full energy peak was determined as a function of energy. `MENATE_R` assumes an isotropic distribution in the center of mass (CM) frame for these reactions. The results of these simulations are shown in Fig. 3.11. The simulated efficiency was used to correct the counts found in each peak in the reconstructed Q-value spectrum to what they would be if all charged reaction products had complete energy deposition.

3.4.2 Neutron attenuation in air

Simulations were performed to account for differences in the shape of the neutron flux caused by attenuation of neutrons through the 57.3 meters of air between the fission chamber and the diamond detectors. The simulations were run with `NPTOOL` [63], which consists of a `GEANT4` [22, 23, 24] and `ROOT` [58] framework. The setup consists of two virtual detectors that detect every neutron that passes through their volume, separated by an air gap. The neutron transmission factor, the ratio of the percentage of counts observed in the second detector with the air gap to that without the air gap, was extracted for incident neutron energies ranging from 10 to 100 MeV. Two different physics packages were used to treat the neutron interactions: `HadronPhysicsQGSP_BIC_HP` and `MENATE_R`.

`HadronPhysicsQGSP_BIC_HP` combines the Quark Gluon Plasma, Binary Cascade and neutron High Precision packages as a physics list that uses empirical data below 20 MeV and a cascade

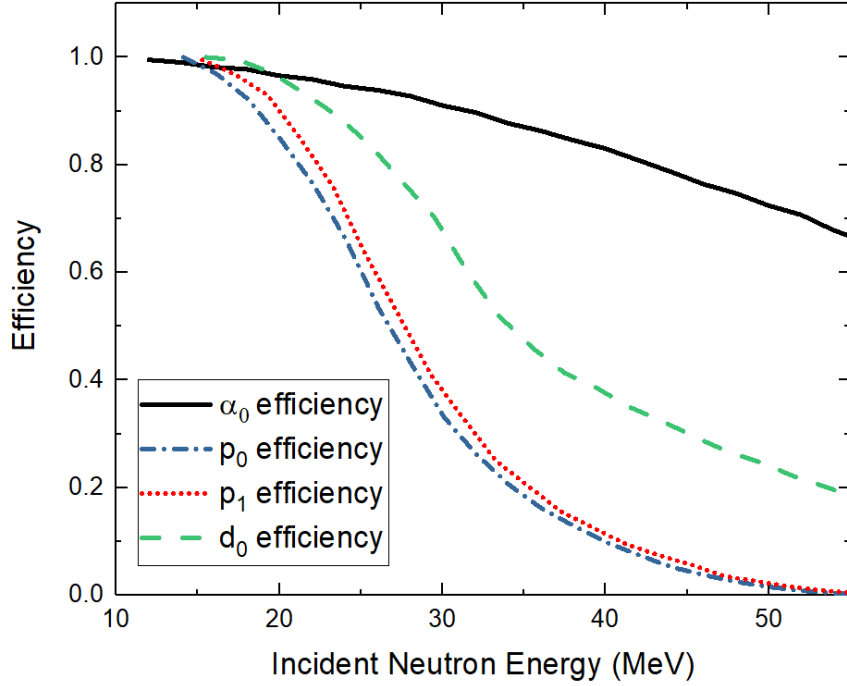


Figure 3.11: Simulated charged particle detection efficiency for $^{12}\text{C}(n,\alpha_0)^9\text{Be}$, $^{12}\text{C}(n,p_0)^{12}\text{B}$, $^{12}\text{C}(n,p_1)^{12}\text{B}$, and $^{12}\text{C}(n,d_0)^{11}\text{B}$. The legend contains only the light ions for simplicity, but the efficiency is for detecting both reaction products.

model above 20 MeV.

MENATE_R is solely based on empirical data, and features cross sections for some of the most common neutron interactions with carbon and hydrogen. Since air consists of relatively low amounts of carbon and hydrogen, a simulation was run with an air-equivalent volume filled with gaseous carbon dioxide, such that the overall particle density of carbon was equal to the particle density of air, taking into consideration the slightly different total cross sections for neutron interactions with carbon, nitrogen, and oxygen.

For the air gap, the reduced density of air at the elevation of Los Alamos (2225 m) was also taken into consideration.

To correct the length of the air gap for MENATE_R, the particle density of carbon in GEANT4 (n_G) was calculated as:

$$n_G = \frac{\rho_{CO_2} \omega_C N_A}{M_C} \quad (3.8)$$

where ρ_{CO_2} (0.00184 g/cm³) is the density of the GEANT4 carbon dioxide material, $\omega_C = 0.279$ is the mass fraction of carbon in carbon dioxide, M_C is the molar mass of carbon, and N_A is Avogadro's constant. Plugging in the values, we obtain:

$$n_G = 2.57 \times 10^{19} \text{ carbon nuclei/cm}^3 \quad (3.9)$$

The particle density of air (n_{air}) is 2.687×10^{19} particles/cm³ at sea level. Correcting for the difference in density between sea level and at the elevation of Los Alamos (2225 m) (ρ_{corr}) and the differences in total cross section for carbon compared with that of nitrogen and oxygen nuclei (σ_{corr}), we obtain the effective particle density for carbon, n_C :

$$n_C = n_{air} \times \rho_{corr} \times \sigma_{corr} = (2.687 \times 10^{19}) (0.80)(1.13) = 2.429 \times 10^{19} \text{ particles/cm}^3 \quad (3.10)$$

Thus, the correction factor for the attenuation medium is

$$n_C/n_G = 2.429/2.57 = 0.945 \quad (3.11)$$

and the length of the carbon dioxide volume was therefore

$$0.945 \times 57.3 \text{ m from the spallation target} = 54.1 \text{ m} \quad (3.12)$$

To ensure a fair comparison between the simulation using `MENATE_R` to the one using the `HadronPhysicsQGSP_BIC_HP` physics list, the attenuation medium was filled with air (CO₂) with a length of 57.3 m (54.1 m) when running the simulation with the `HadronPhysicsQGSP_BIC_HP` physics list (`MENATE_R`). The neutron transmission factor was calculated the same way in both cases.

Since the neutron transmission factors calculated with `MENATE_R` showed a more consistent trend, they were used for the analysis. To verify the applicability of the carbon dioxide with `MENATE_R` simulation, the neutron transmission factor was also calculated using the `HadronPhysicsQGSP_BIC_HP` physics list and carbon dioxide as the attenuation material. Due to the way the data is normalized, the absolute transmission is not used in the cross section calculation. Rather, the ratio of transmission-corrected fluxes is used, so only the relative treatment of the transmission is important. A comparison of the three simulated transmissions is shown in Fig. 3.12.

3.4.3 MCNP Flux

An MCNP [48, 64] simulation of the neutron flux distribution at the spallation target was used to benchmark the flux measured in the fission chamber. The MCNP-simulated flux was corrected to account for neutron attenuation through 85.7 m of air, similar to the approach discussed in the previous section. Generally, this simulated flux has shown relatively good agreement with the flux distributions measured with the flux monitors at LANSCE. Since the flux monitor was not set up in the 90 m station due to low expected count rates, the difference between the measured flux and the MCNP simulated flux was taken as the uncertainty in the flux distribution. This approach has the

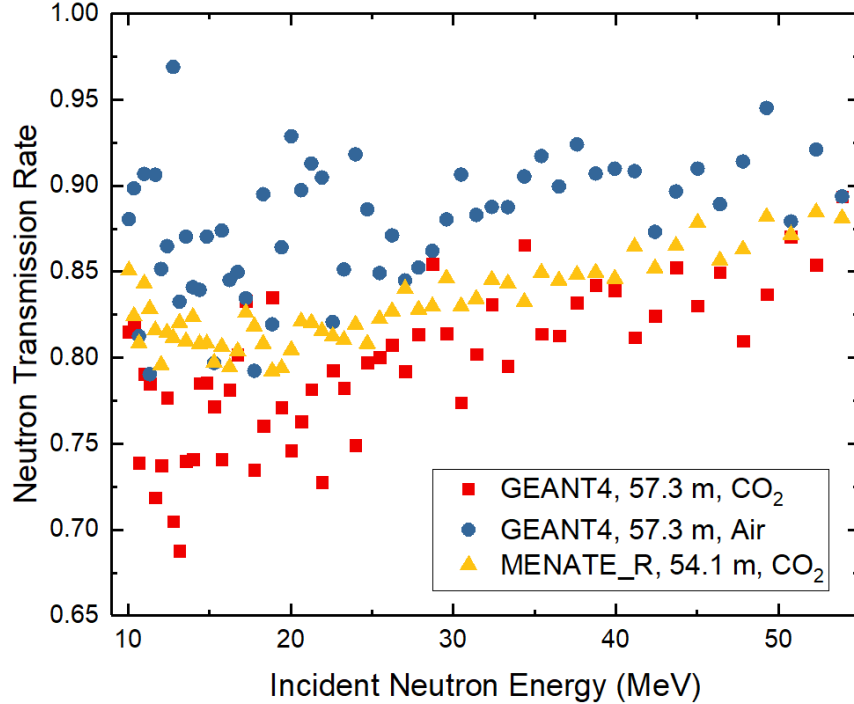


Figure 3.12: A comparison between simulated neutron transmissions using GEANT4 (HadronPhysicsQGSP_BIC_HP) and 57.3 m of air as the attenuation medium, and MENATE_R, with 54.1 m of carbon dioxide as the attenuation medium. See text for details.

benefit of small uncertainties (5%) at lower energies where the normalization is performed and larger uncertainties at higher energies where there is less confidence in the simulation. Admittedly, this is not a generally applicable method of quantifying the flux uncertainty. However, the flux uncertainty obtained with this method is much larger than that calculated from the fission chamber statistics and the $^{235}\text{U}(n,f)$ standard cross section uncertainties, and thus makes a conservative statement about our confidence in the flux distribution. A comparison of the MCNP flux and fission chamber flux are shown in Fig. 3.6. The uncertainty in the neutron transmission simulations is also included in the flux distribution uncertainty. If the uncertainty in the neutron transmission correction was calculated separately based on the discrepancies between the ENDF n-C total cross section [65] and the sum of the cross sections included in MENATE_R, the uncertainty would be no higher than 7%, and typically much lower, up to 25 MeV incident neutron energy, and 10-15% above 25 MeV. This supports the idea that using the MCNP-simulated flux for the flux distribution uncertainty quantification makes a conservative statement about our confidence in the flux distribution.

3.5 Cross section normalization

As mentioned in Section 2.4, the fission chamber was located near the Chi-Nu/CoGNAC array, 57.3 m upstream of the diamond detectors in the 90 m station. Due to the expected low count

rate, a fission chamber was not installed in the station, which created additional complications in extracting an absolute flux for our experiment:

- Notably, the beam spot size differs significantly between the fission chamber location and the 90 m station, as the beam spreads out before passing through the tertiary collimation just before entering the shed.
- Furthermore, the effect of the collimation on the neutron flux has not been characterized, allowing for the possibility of a focusing effect, whereby the flux before and after the collimation does not correspond to what a comparison of solid angles before and after the collimation would predict.
- Calculating the absolute flux at the 90 m station would also require an accurate characterization of the effect of passing through 57.3 m of air. Beam images were taken in an attempt to quantify the attenuation of neutrons, but the automatic scaling of the images performed by the scanner did not allow for an absolute comparison between images.
- Although the number of target nuclei in the diamond detectors is easily calculable, an assessment of the uniformity of this number in and between each diamond is much harder to obtain, since one detector (downstream) had received much more beam prior to the run than the other (upstream).
- Last, the fission chamber was not collecting data for the full duration of the run. While the flux distribution may be valid, the time period over which it was time-integrated does not correspond to the same period that was used for the diamond detectors.

For all these reasons, the absolute neutron flux in the 90 m station could not be determined with certainty, so that an absolute normalization could not be determined. Instead, the cross section measurement was performed relative to existing data, wherein the $^{12}\text{C}(n,\alpha)^9\text{Be}$ channel at 14.1 MeV was used for normalization. This channel is easily identifiable in our dataset with no internal background. This normalization procedure follows the approach of [15], in which recent data from the EXFOR database [66] were used in the calculation of a weighted average $^{12}\text{C}(n,\alpha)^9\text{Be}$ cross section, as shown in Table 3.4. The data from which the weighted average was calculated feature lower systematic uncertainties than earlier measurements. 14.1 MeV is used as the normalization point because many measurements have been made at this energy, and it has also been used as a point of comparison for other studies [37]. This weighted average (n, α) cross section, 63.6 mb ($\sigma_{n,\alpha}$ accepted), carries with it an uncertainty of 4.9%.

The cross section calculation at other incident neutron energies takes the form:

$$\sigma = \gamma \sigma_{n,\alpha \text{ accepted}} \quad (3.13)$$

where the normalization factor, γ , is

$$\gamma = \frac{N\Phi_0 N_{\text{target}} \varepsilon_0}{N_{n,\alpha} \Phi N_{\text{target}} \varepsilon} \quad (3.14)$$

Table 3.4: A breakdown of the data that was used to obtain the weighted average cross section for the $^{12}\text{C}(n,\alpha)^9\text{Be}$ reaction at 14.1 MeV, following the approach of [15].

Reference	E_n (MeV)	σ (mb)	Detection Method
Schmidt <i>et al.</i> [17]	14.02 ± 0.03	56.5 ± 1.9	Derived from inverse reaction: $^9\text{Be}(\alpha,n)^{12}\text{C}$
Schmidt <i>et al.</i> [17]	14.20 ± 0.04	62 ± 2.1	Derived from inverse reaction: $^9\text{Be}(\alpha,n)^{12}\text{C}$
Haight <i>et al.</i> [16]	14.10 ± 0.15	72 ± 9	2 ΔE prop. counters, 1 E solid state counter
Sanami <i>et al.</i> [18]	14.10	70 ± 7	Gridded ionization chamber
Pillon <i>et al.</i> [12]	14.10 ± 0.01	64.7 ± 3.2	Diamond detector
Kondo <i>et al.</i> [19]	14.2 ± 0.2	69 ± 6	Si surface barrier detector telescope (ΔE -E)
Weighted average	14.1	63.6 ± 3.1	

N represents the background-subtracted counts measured in a given bin for a particular reaction channel, Φ_0 represents the neutron flux from the fission chamber at 14.1 MeV, ε_0 represents the detection efficiency of the $^{12}\text{C}(n,\alpha_0)^9\text{Be}$ reaction products at 14.1 MeV, $N_{n,\alpha}$ represents the (n,α) counts detected in the 14.1 MeV bin, Φ is the neutron flux obtained from the fission chamber, and ε is the detection efficiency of the charged particles produced in the reaction. This has the benefit that N_{target} , the number of target nuclei, cancel out if the same detectors are used for the normalization, i.e. to obtain N and $N_{n,\alpha}$. Additionally, only the ratio of neutron flux at different energies is considered, removing the possible focusing effect due to collimation.

3.6 R matrix fits

R matrix fits were performed with AZURE2 [67] for each of the reactions studied in this work. The information used to create the entrance and exit particle pairs is included in Table 3.5. The light particle spin and heavy particle spin were obtained from the NNDC [61]. The separation energy (S) was calculated via

$$S = (M_1 + M_2 - M_C) \times 931.5 \text{ MeV/u} \quad (3.15)$$

where M_1 and M_2 are the masses of the two entrance (or exit) particles, respectively, and M_C is the mass of the compound nucleus, in this case ^{13}C .

The channel radius (R) was obtained from

$$R = R_0(A_1^{1/3} + A_2^{1/3}) \quad (3.16)$$

where $R_0 = 1.2$ fm is the constant of proportionality for an average nuclear radius, and A_1 and A_2 are the masses in atomic mass units (u) of the two entrance (or exit) particles, respectively. The R matrix fits should be independent of the channel radius.

For each reaction, various compound nucleus levels were included. Several background levels were included at higher excitation energy: 25 MeV for (n,α) and 35 MeV for (n,p_0) , (n,p_1) , and

Table 3.5: Data used to create the particle pairs for the reactions in AZURE2

Entrance Channel						
Light Particle	Light spin	Heavy Particle	Heavy spin	E_x (MeV)	S (MeV)	Channel Radius (fm)
n	$1/2^+$	^{12}C	0^+	0	4.946	3.947
Exit Channels						
α	0^+	^9Be	$3/2^-$	0	10.648	4.401
p	$1/2^+$	^{12}B	1^+	0	17.533	3.947
p	$1/2^+$	^{12}B	2^+	0.953	17.533	3.947
^2H	1^+	^{11}B	$3/2^-$	0	18.68	4.108

(n,d_0). More importantly, levels were included that correspond to resonances observed in the excitation function for each reaction. The levels included for each reaction are shown in Table 3.7. The columns labeled “Fix?” refer to whether or not the state was fixed in excitation energy. The width was kept as a free parameter for every state. An arbitrary initial partial width of 1000 eV was used for every level and channel combination. The energies listed in Table 3.7 refer to the excitation energy of the compound nucleus.

The data used for fitting are angle-integrated, energy-differential cross sections. R matrix analysis is often performed with double differential cross section data, with the benefit that fitting a resonance of unknown J^π across different angles can help confirm the J^π . When fitting angle-integrated data, this method of confirmation is not available. However, we do have access to various reaction channels, which can also be used to help confirm the spin and parity assignments of unknown states. At the time of writing this manuscript, only single-channel fits have been performed on the data; future work will involve fitting all reaction channels simultaneously to lend greater support for our conclusions.

The data files used for the fitting already included a full uncertainty quantification. The data norm. was set to one, and held fixed, and the norm. error was set to 0. The excitation functions were fit over the range where resonance-like behavior was observed, so from incident neutron energies up to 21.5 MeV for (n,α), and about 27 MeV for (n,p_0), (n,p_1), and (n,d_0). No experimental effects, such as beam energy loss in target, energy resolution, or geometric effects of the setup, were included, as the fits matched the data reasonably well without including such effects. The results of the R matrix analysis are included in Section 4.2.

Table 3.6: Initial levels and channels that were included in the AZURE2 calculation for $^{12}\text{C}(\text{n},\alpha)^9\text{Be}$

Fix?	Level Spin	Energy
yes	$3/2^-$	12.282 MeV
no	$9/2^-$	13.5 MeV
yes	$7/2^-$	14.05 MeV
yes	$5/2^-$	16.0577 MeV
yes	$7/2^+$	16.081 MeV
no	$3/2^+$	16.1 MeV
no	$3/2^+$	18.42 MeV
no	$5/2^-$	20.56 MeV
no	$5/2^+$	23.3 MeV
yes	$1/2^-$	25 MeV
yes	$1/2^+$	25 MeV
yes	$3/2^-$	25 MeV
yes	$3/2^+$	25 MeV
yes	$5/2^-$	25 MeV
yes	$5/2^+$	25 MeV

Table 3.7: Initial levels and channels that were included in the AZURE2 calculation for $^{12}\text{C}(\text{n},\text{p}_0)^{12}\text{B}$, $^{12}\text{C}(\text{n},\text{p}_1)^{12}\text{B}$, and $^{12}\text{C}(\text{n},\text{d}_0)^{11}\text{B}$.

$^{12}\text{C}(\text{n},\text{p}_0)^{12}\text{B}$			$^{12}\text{C}(\text{n},\text{p}_1)^{12}\text{B}$			$^{12}\text{C}(\text{n},\text{d}_0)^{11}\text{B}$		
Fix?	Spin	Energy (MeV)	Fix?	Spin	Energy (MeV)	Fix?	Spin	Energy (MeV)
yes	$1/2^-$	19.9	no	$1/2^+$	21.28	yes	$1/2^+$	22.23
yes	$1/2^-$	21.15	no	$5/2^+$	24	yes	$1/2^+$	25.95
yes	$7/2^+$	27	yes	$5/2^+$	25.99	yes	$1/2^-$	28.75
yes	$1/2^-$	35	yes	$1/2^-$	35	yes	$1/2^-$	35
yes	$1/2^+$	35	yes	$1/2^+$	35	yes	$1/2^+$	35
yes	$3/2^-$	35	yes	$3/2^-$	35	yes	$3/2^-$	35
yes	$3/2^+$	35	yes	$3/2^+$	35	yes	$3/2^+$	35
yes	$5/2^-$	35	yes	$5/2^-$	35	yes	$5/2^-$	35
yes	$5/2^+$	35	yes	$5/2^+$	35	yes	$5/2^+$	35

Chapter 4

RESULTS AND DISCUSSION

4.1 Cross sections

4.1.1 $^{12}\text{C}(n,\alpha)^9\text{Be}$

Energy-differential cross sections for the $^{12}\text{C}(n,\alpha)^9\text{Be}$ reaction were determined from $E_n = 12.5$ MeV to 55 MeV. The cross sections are plotted in Fig. 4.1. Various data for this channel, including counts, charged particle detection efficiency, neutron transmission correction factors, uncertainties, and the cross sections, are located in Table A.1 in the appendix. This measurement dramatically extends the energy range over which cross sections have been determined for this channel. Strong agreement is shown between this work and recent measurements performed with diamond detectors ([12, 13, 14, 15]). Resonances are observed in the excitation function, and are discussed later (Section 4.2). These resonances correspond to enhancements of the cross section around excited states of the ^{13}C ($^{12}\text{C}+n$) compound nucleus. This work and recent data sets are compared to the ENDF/B-VIII.0 evaluation [65]. The ENDF/B-VIII.0 evaluation is based on older experimental data, and does not take into consideration the studies shown in Fig. 4.1. Good agreement is shown between this work, recent studies, and the evaluation from 17-20 MeV, but lesser agreement is shown below 17 MeV. Additionally, the evaluation does not extend above 20 MeV, due to limited data when the evaluation was made. This work provides data that could extend the evaluation to 55 MeV incident neutron energy. The newest evaluation (ENDF/B-VIII.1) did not contain any update for the $^{12}\text{C}(n,\alpha)^9\text{Be}$ cross section.

4.1.2 $^{12}\text{C}(n,p_0)^{12}\text{B}$

The cross sections determined for the production of a proton and population of ^{12}B in the ground state are shown in Fig. 4.2, and extend from $E_n = 15.7$ MeV to 27.6 MeV. Only studies that measured the exclusive population of ^{12}B in the ground state are included in this figure. Older works, including those of Kellogg [28], Bobyr [29], Ablesimov [30], Rimmer [31], and Kreger [32], which all used the activation technique, are not included here. Activation measurements that detect the beta decay of the ^{12}B ground state do not accurately represent this cross section, since

the ground state of ^{12}B can be fed not only through $^{12}\text{C}(n,p_0)^{12}\text{B}$, but also from the decay of higher excited states of ^{12}B . Rimmer [31] in particular notes that this may be an issue, but discounts it as unlikely. However, as the present work and the work of Pillon et al. [13] showed, the cross section for (n,p_1) is on the same order as (n,p_0) . When production of the ^{12}B ground state via decay of the 1st, 2nd, 3rd, and 4th excited states of ^{12}B is also considered, the cross section of the $^{12}\text{C}(n,p_0)^{12}\text{B}$ reaction may be significantly overpredicted by an activation measurement of the ^{12}B ground state. The counts, charged particle detection efficiency correction, and neutron transmission correction are included in Table A.2 in the appendix, while the cross sections and full uncertainty quantification are located in Table A.3 in the appendix.

Reasonable agreement is shown with previous studies [15, 14, 12, 13]. Of these, better agreement is shown with the data of Kuvín [15] and Pillon (2017) [13], while the earlier work of Pillon (2011) [12] is generally lower than our measured cross section, and the Majerle study [14] found a very large cross section with significant uncertainty at $E_n = 17.3$ MeV. Some structure in the cross section is visible, with possible resonances observed in the excitation function, discussed in Section 4.2. There is no ENDF evaluation for this partial cross section, unlike $^{12}\text{C}(n,\alpha)^9\text{Be}$, so this comparison cannot be made. There is an evaluated inclusive cross section for $^{12}\text{C}(n,p)$, which combines at least $^{12}\text{C}(n,p_0)^{12}\text{B}$, $^{12}\text{C}(n,p_1)^{12}\text{B}$, $^{12}\text{C}(n,p_2)^{12}\text{B}$, $^{12}\text{C}(n,p_3)^{12}\text{B}$, and $^{12}\text{C}(n,p_4)^{12}\text{B}$, but this is not directly comparable to the $^{12}\text{C}(n,p_0)^{12}\text{B}$ partial cross section.

A comparison was made with a TALYS [50] calculation performed using default parameters, as was done in [15]. The calculation agrees with the scale of the data but does not feature the fluctuations that may be due to resonant behavior.

McNaughton *et al.* also published data on the $^{12}\text{C}(n,p_0)^{12}\text{B}$ channel [68]. This study used silicon ΔE and sodium iodide E detectors to detect charged reaction products from neutron interactions on a carbon target. In theory, this should be a valid method to investigate these reactions. However, numerous discrepancies in the published work make it less than ideal for comparison. Based on the published proton energy spectra, various states are observed. However, while these states should correspond to the energies of the states of ^{12}B , they do not correspond to any measured states, and the J^π are incorrect. In McNaughton’s study [68], states are identified as $^{12}\text{C}(n,p_0)^{12}\text{B}$ ($E_x = 0$ MeV, $J^\pi = 1^+$), $^{12}\text{C}(n,p_1)^{12}\text{B}$ ($E_x = 4.3$ MeV, $J^\pi = 2^-$), and $^{12}\text{C}(n,p_2)^{12}\text{B}$, ($E_x = 7.4$ MeV, $J^\pi = 1^-$). However, the latter two states do not correspond to measured states of ^{12}B . There is a 1^- state of ^{12}B at $E_x = 4.3$ MeV, but for the 7.4 MeV state, there are no measured states within 100 keV. Not only do these states not match with the designation of the first and second excited states of ^{12}B in this work and other recent works, they do not match up with any excited states. Further, both of these states, if they existed, would be neutron unbound, and hence unlikely to produce a sharp peak in the proton spectra. Because of these inconsistencies, as well as the fact that only statistical uncertainties are listed, so that a full uncertainty quantification is missing, these results are not included in the cross section plots. For completeness, McNaughton *et al.* [68] obtained a cross section of 3.4 ± 0.6 mb for the $^{12}\text{C}(n,p_0)^{12}\text{B}$ cross section at 56 MeV, which might be a

reasonable value if not for the issues listed above.

4.1.3 $^{12}\text{C}(n,p_1)^{12}\text{B}$

Cross sections were also determined for the $^{12}\text{C}(n,p_1)^{12}\text{B}$ reaction, in which a proton and ^{12}B in the first excited state ($J^\pi = 2^+$, $E_x = 0.953$ MeV) are produced. The cross sections for this channel are shown in Fig. 4.3. The counts, charged particle detection efficiency correction, and neutron transmission correction are included in Table A.4 in the appendix, while the cross sections and full uncertainty quantification are located in Table A.5 in the appendix. Only the work of Pillon *et al.* (2017) [13] published a cross section for this channel that is directly comparable. This work extends the energy range over which cross sections have been determined, from 16.5 to 27.6 MeV (previously 18.9 to 20.7 MeV). Other studies did not report a separate cross section for this channel, largely due to insufficient resolution to isolate the contributions of this channel and $^{12}\text{C}(n,d_0)^{11}\text{B}$. These channels have very similar Q values, (-13.54 and -13.73 MeV for the (n,p₁) and (n,d₀) channels, respectively). One study [15], realized that they did not have sufficient resolution to isolate these peaks, and instead published a combined (n,p₁ + d₀) cross section. Other studies [14, 12] are in a similar situation, in that they could not isolate the (n,p₁) channel whether it was reported in the original work or not. In the present work, although the (n,p₁) and (n,d₀) channels are not fully separated, two distinct peaks are easily observed and identified at these energies.

Reasonable agreement is shown between this work and Pillon’s study [13]. The relatively higher cross section that Pillon measured at 18.91 MeV was consistent with the findings of this work. The other cross sections by Pillon are almost within the uncertainties of this study. This reaction channel suffered from low statistics, compared to the much higher yields for the (n, α) and (n,d₀) channels. A number of the cross sections appear to be aberrant, such as at 17.18, 17.42, 18.94, and/or 21.3 MeV, but the fits in HDTV were verified rigorously.

Again, there is no ENDF evaluation for this exclusive cross section, only the inclusive cross section for $^{12}\text{C}(n,p)$ which is not directly comparable. Instead, a TALYS calculation using default parameters was performed. The calculation agrees with the scale of the data, but again is not expected to account for the potentially resonant behavior.

4.1.4 $^{12}\text{C}(n,d_0)^{11}\text{B}$

The last channel for which cross sections were determined in the present work is $^{12}\text{C}(n,d_0)^{11}\text{B}$, shown in Fig. 4.4. The counts, charged particle detection efficiency corrections, and neutron transmission corrections are included in Table A.6 in the appendix, while the cross sections and full uncertainty quantification are located in Table A.7 in the appendix. Again, only the Pillon (2017) study [13] is directly comparable. The present work extended the energies over which cross sections have been measured both below and above the incident neutron energies of the Pillon study, from $E_n = 15.8$ to 45.5 MeV. Although several other studies [14, 12] reported cross sections for $^{12}\text{C}(n,d_0)^{11}\text{B}$, they did not have sufficient resolution to isolate the (n,d₀) from the (n,p₁), and

due to the non-negligible (n,p_1) contribution to the cross section, they are not directly comparable. Again, Kuvín *et al.* published a combined $(n,d_0 + p_1)$ cross section since their resolution was insufficient to separate the peaks. A discussion of these results is discussed in the next section

The data for this channel in the current work agree fairly well with Pillon’s findings [13]. The scale of the data matches well. The relatively higher cross section that Pillon measured at $E_n = 18.91$ MeV is consistent with the measurements of this work, as a possible resonant structure is observed in that energy range. Two of the cross sections measured by Pillon were larger than those measured in this work, at 19.88 and 20.69 MeV, but the rest of their cross sections are within our uncertainty. This channel had much higher statistics than the (n,p_0) and (n,p_1) channels.

Once again, there is no ENDF evaluation for the $^{12}\text{C}(n,d_0)^{11}\text{B}$ partial cross section, only an inclusive cross section $^{12}\text{C}(n,d)$, which is not directly comparable. Instead, a TALYS calculation using default parameters was performed. The calculation does not agree as well with the scale of the data as the calculations did for (n,p_0) and (n,p_1) . The shape of the calculation agrees reasonably well with the data, but again is not expected to account for the potentially resonant behavior.

McNaughton *et al.* [68] also published a partial cross section for this channel, 20 ± 2 mb for 56 MeV neutrons. Although the (n,d_0) data looked reasonable in the work, because of the issues with the states of the (n,p) reactions published in this work, described in Section 4.1.2, this datum was not include in the cross section plots either.

4.1.5 $^{12}\text{C}(n,d_0)^{11}\text{B} + ^{12}\text{C}(n,p_1)^{12}\text{B}$

To allow for comparison with datasets that could not isolate the (n,d_0) and (n,p_1) channels, the combined cross sections for $^{12}\text{C}(n,d_0)^{11}\text{B} + ^{12}\text{C}(n,p_1)^{12}\text{B}$ are shown in Fig. 4.5. The data for this work and Pillon (2017) were obtained from summing the separate cross sections for $^{12}\text{C}(n,p_1)^{12}\text{B}$ and $^{12}\text{C}(n,d_0)^{11}\text{B}$ in the respective works, which are shown separately in Figs. 4.3 and 4.4. The data for Kuvín (2021) were directly taken from the published $^{12}\text{C}(n,d_0 + p_1)$ cross section published in that work. For Pillon (2011) and Majerle (2020), data were taken from the respective published $^{12}\text{C}(n,d_0)^{11}\text{B}$ cross sections, since the data for (n,p_1) was contained within the (n,d_0) peak. These results are compared with a TALYS calculation, which summed the results of the individual (n,d_0) and (n,p_1) channels, which are also shown separately in Figs. 4.3 and 4.4 Overall good agreement is shown with both studies of Pillon *et al.* and Majerle *et al.*. The significantly smaller cross sections measured by Kuvín *et al.* around 20 MeV were not replicated in this work, but otherwise the Kuvín data is well reproduced. The TALYS calculation underpredicts the majority of the data. This underprediction is primarily due to the $^{12}\text{C}(n,d_0)^{11}\text{B}$ channel, as seen in the poor gross agreement between TALYS and data in Fig. 4.4 for (n,d_0) , and the good gross agreement observed in Fig. 4.3 for (n,p_1) . Above 29 MeV, the (n,p_1) channel was not observed in the present work. Thus, the combined $(n,d_0 + p_1)$ data did not have a separate contribution from (n,p_1) above 29 MeV.

4.1.6 Cross section uncertainties

The total uncertainty for the cross sections is the quadrature sum of the individual uncertainties, including statistical, charged-particle efficiency correction, fit/integration, previous data for normalization, and flux shape. The uncertainties are assumed to be uncorrelated.

Statistical Uncertainties:

Common to all experiments are statistical uncertainties. The statistical uncertainties for $^{12}\text{C}(n,\alpha)^9\text{Be}$ were determined from the square root of the (n,α) counts (N), since there is no background to consider. Thus, for the (n,α) channel,

$$\sigma_{\text{statistical}} = \sqrt{N} \quad (4.1)$$

and the fractional uncertainty is given by

$$\sigma_{\text{fractional,statistical}} = \frac{\sqrt{N}}{N} \quad (4.2)$$

For the other channels, a linear background was subtracted to find the counts due to only the (n,p_0) , (n,p_1) , or (n,d_0) channels. The statistical uncertainties for these must therefore include the background counts, so for the (n,d_0) channel, for instance,

$$\sigma_{\text{statistical}} = \sqrt{N_{n,d_0} + N_{\text{background}}} = \sqrt{N_{\text{total}}} \quad (4.3)$$

where N_{total} is the total number of counts over the fitting region, both in the peak and in the background. The fractional uncertainty due to statistics is calculated via

$$\sigma_{\text{fractional,statistical}} = \frac{\sqrt{N_{n,d_0} + N_{\text{background}}}}{N_{n,d_0}} = \frac{\sqrt{N_{\text{total}}}}{N_{n,d_0}} \quad (4.4)$$

These fractional uncertainties were calculated for each cross section and included in the quadrature sum for the total uncertainty for each cross section.

The primary way of reducing the statistical uncertainties at the analysis stage is to reduce the granularity of the cross sections, that is, to use larger incident neutron energy windows for each cross section data point. There is a trade-off when determining the bin size: using smaller incident neutron energy ranges can reveal structures and resonant behavior in the data, but at the expense of larger statistical uncertainties. In this study, the bins were chosen to have a consistent ToF spread. This has the benefit that the bins cover a larger energy spread at higher incident neutron energies, so that the smaller cross sections and lower efficiencies at higher energies are partially offset by the larger bins. Additionally, since resonant behavior is less likely to be observed at higher energies, there is less to lose by using a larger incident neutron energy window at higher energies. 5.8 ns-wide ToF bins were used for the $^{12}\text{C}(n,\alpha)^9\text{Be}$ cross section, to match what was used by Kuvín *et al.* [15]. 15 ns ToF bins were used for the $^{12}\text{C}(n,p_0)^{12}\text{B}$ cross section, to help offset

the increased statistical uncertainties due to fewer events, a result of the reduced cross section and efficiency for this channel. 10 ns ToF bins were used for the $^{12}\text{C}(n,p_1)^{12}\text{B}$ and $^{12}\text{C}(n,d_0)^{11}\text{B}$ cross sections. This was chosen so that the same histograms could be fit to extract counts from the (n,p_1) and (n,d_0) channels, which were fit simultaneously in HDTV. The (n,d_0) yield is much higher than that of (n,p_1) , so (n,d_0) could reasonably have used slightly smaller bins if not for this constraint and (n,p_1) could have used larger bins. The statistical uncertainties are part of the reason why (n,p_1) has the largest uncertainties of the channels studied in this work.

An additional source of statistical uncertainty contributed to every channel: the uncertainty in the number of (n,α) counts at 14.1 MeV $N_{n,\alpha}$ in Equation 3.14, used for normalization. This uncertainty, a constant 2.96%, has a relatively small effect in the total uncertainty at low incident neutron energy, and decreasing contributions at higher incident neutron energies.

Charged particle detection efficiency uncertainty:

As mentioned in Section 3.4.1, the counts for each reaction channel in each incident energy bin were corrected to account for incomplete energy deposition of charged reaction products. This effect was simulated in MENATE_R, which assumes an isotropic distribution in the center-of-mass frame. Based on comparisons with experimentally measured $^{12}\text{C}(n,\alpha)^9\text{Be}$ angular distributions, this was determined to create an uncertainty of about 4%. This uncertainty was used for all of the reaction channels and at every energy presented in this work. Majerle *et al.* [14] studied the effect of the angular distributions of the reaction products on their simulated efficiency, comparing the isotropic in the center-of-mass system angular distribution (a) with the extreme case of forward directed alphas, protons, and deuterons (b). Table 2 from that paper [14] is reproduced here in Table 4.1. The angular distribution was shown to have a significant effect on the efficiency; however, the experimental data show that the reaction products are not solely forward-directed as in the extreme case studied by Majerle. The simulated efficiencies used in the present work differ slightly from those used in the Majerle study, with universally higher simulated efficiencies in the present work, resulting in a smaller efficiency correction factor for the cross sections. This may be due to the differing energy resolutions of the detectors in the present work and in Majerle’s study, and perhaps using a slightly different cutoff for the full energy peak. Slightly better agreement is shown between the present work and the efficiency used in Kuvin’s study [15]. The efficiency of (n,p_1) is very similar to that of (n,p_0) , but slightly higher due to the removal of 0.953 MeV of kinetic energy from the charged reaction products; compare with Fig. 3.11.

Fit/Integration:

The (n,α) channel did not require any fitting to extract the counts, only a simple 1-dimensional gate. For the other channels, a fit was performed using a Gaussian and linear background. This introduces uncertainty based on the quality of the fit and the degree to which the data match the Gaussian line shape. Thus, the fit/integration uncertainty is zero for the (n,α) but is nonzero for

Table 4.1: A reproduction of Table 2 in Majerle *et al.* [14], in which the simulated charged particle detection efficiency is compared for two angular distributions: (a), in which an isotropic distribution in the center of mass frame is used, and (b), in which the alphas, deuterons, and protons were fully forward focused. The angular distributions used in the present study agree much closer with (a),

E_n (MeV)	$^{12}\text{C}(n,\alpha_0)^9\text{Be}$		$^{12}\text{C}(n,d_0)^{11}\text{B}$		$^{12}\text{C}(n,p_0)^{12}\text{B}$	
	Detection Efficiencies					
	a	b	a	b	a	b
17.3	0.97	0.91	0.98	0.93	0.93	0.82
20.4	0.95	0.87	0.92	0.77	0.81	0.52
20.5	0.95	0.87	0.92	0.76	0.8	0.51
24.6	0.93	0.81	0.8	0.46	0.57	
26.1	0.92	0.78	0.75	0.32	0.49	
28.8	0.9	0.73	0.64		0.36	
30.7	0.88	0.69	0.57		0.27	
33.3	0.86	0.63	0.48		0.19	
34.2	0.85	0.61	0.45		0.17	

the other channels. To quantify this uncertainty, the width error produced by HDTV was divided by the width parameter of the fit. This produced uncertainties of roughly 4% at lower energies for the (n,p₀) and (n,d₀) channels, which increased up to approximately 10% at higher energies. The fit/integration uncertainty was higher for (n,p₁), increasing from about 6% to 17% at the highest energies. The quality of each fit was evaluated by eye, and the uncertainty quantified here matched well with the qualitative judgment of the fit. The peak quality degrades as one moves to higher energy, since the statistics get lower.

Previous data (normalization):

As discussed in Section 3.5, and enumerated in Table 3.4, the cross sections were normalized to previous $^{12}\text{C}(n,\alpha)^9\text{Be}$ experimental data [12, 16, 17, 18, 19] at 14.1 MeV. The absolute cross sections presented in this work can only be as good as the cross sections to which they are normalized. The weighted average of these previous measurements carries with it 4.9% uncertainty that applies to every cross section presented in this work. For the lowest energy (12-17 MeV) (n, α) cross sections, this is a significant contribution to the total uncertainty. At higher energies and for the other channels, the other uncertainties – particularly statistical, flux, and fit/integration uncertainties – are larger, and thus the previous data uncertainty contributes less to the total uncertainty.

Flux shape:

As mentioned in Section 3.4.3, the fission chamber (flux monitor) was not located at the same location as the diamond detectors. Thus, there was more uncertainty than one would calculate based solely on the fission chamber statistics and $^{235}\text{U}(\text{n},\text{f})$ cross section uncertainties. Instead, the flux uncertainty was quantified by the deviation of the fission chamber's derived flux with a trusted MCNP simulation. Fig. 4.6 compares the uncertainty in the neutron flux based on the two approaches. To obtain the blue curve, the uncertainty from the fission chamber statistics in each of our cross section bins was summed in quadrature with the uncertainties from the $^{235}\text{U}(\text{n},\text{f})$ reference standard cross sections. These uncertainties are significantly smaller than those obtained from the deviation with simulation. Although one could hope that our measured flux shape is more accurate than this method would suggest, we erred on the side of caution to make a conservative statement about our confidence in the flux shape.

Incident neutron energy reconstruction:

The incident neutron energy was reconstructed from the neutron ToF and flight path distance, using the following formula:

$$E_n = m_n c^2 \left(\frac{1}{\sqrt{1 - (\frac{l}{ct})^2}} - 1 \right) \quad (4.5)$$

where l is the distance and t is the neutron ToF. The extrema of the energy measurements occur when $l = l + \sigma_l$ and when $t = t - \sigma_t$, and the opposite. The uncertainty in the path length was at most 10 cm, and the neutron ToF was known to within 1 ns. Thus, the uncertainty in the reconstruction was obtained from a worst-case error analysis of the relativistic incident energy calculation. This yields uncertainties ranging from 0.35% at 12 MeV and 0.49% at 55 MeV.

For simplicity, the maximum incident neutron energy reconstruction uncertainty for the energies in this work (0.49%, at 55 MeV), was adopted for every data point. This uncertainty is much smaller than the other uncertainties and thus does not affect the total uncertainty significantly. This uncertainty was also taken as the incident neutron energy (horizontal axis) error bars in the cross section plots.

4.1.7 Visualizing cross section uncertainties

To easily visualize the impacts of the various sources of uncertainty, Figs. ?? ?? show how individual uncertainties contribute to the total uncertainty for each measured cross section. The height of each bar corresponds to the total fractional uncertainty, which is what is used to create the vertical error bars in the cross section plots. Each column in the uncertainty plot corresponds to one data point in the corresponding cross section plot. The relative contribution for each source of uncertainty to each bar is based on the percentage of the total uncertainty, but is only intended to be viewed qualitatively.

These uncertainty plots can also be used to visualize the total uncertainties in the cross sections between each of the channels. The (n,α) cross section features the lowest fractional uncertainties at low energy, but has extremely large fractional uncertainties at higher energies. Less variation in the total uncertainty is observed for the other channels, with the (n,p_0) , (n,p_1) , and (n,d_0) channels having between approximately 9% and 30% uncertainty at the highest energies. These plots demonstrate that at low energy, the total uncertainty is not dominated by a single source, but instead is due to a mix of contributions. At high energies, the statistical and flux distribution uncertainties dominate, in addition to the fit/integration uncertainty for the (n,p_0) , (n,p_1) , and (n,d_0) channels.

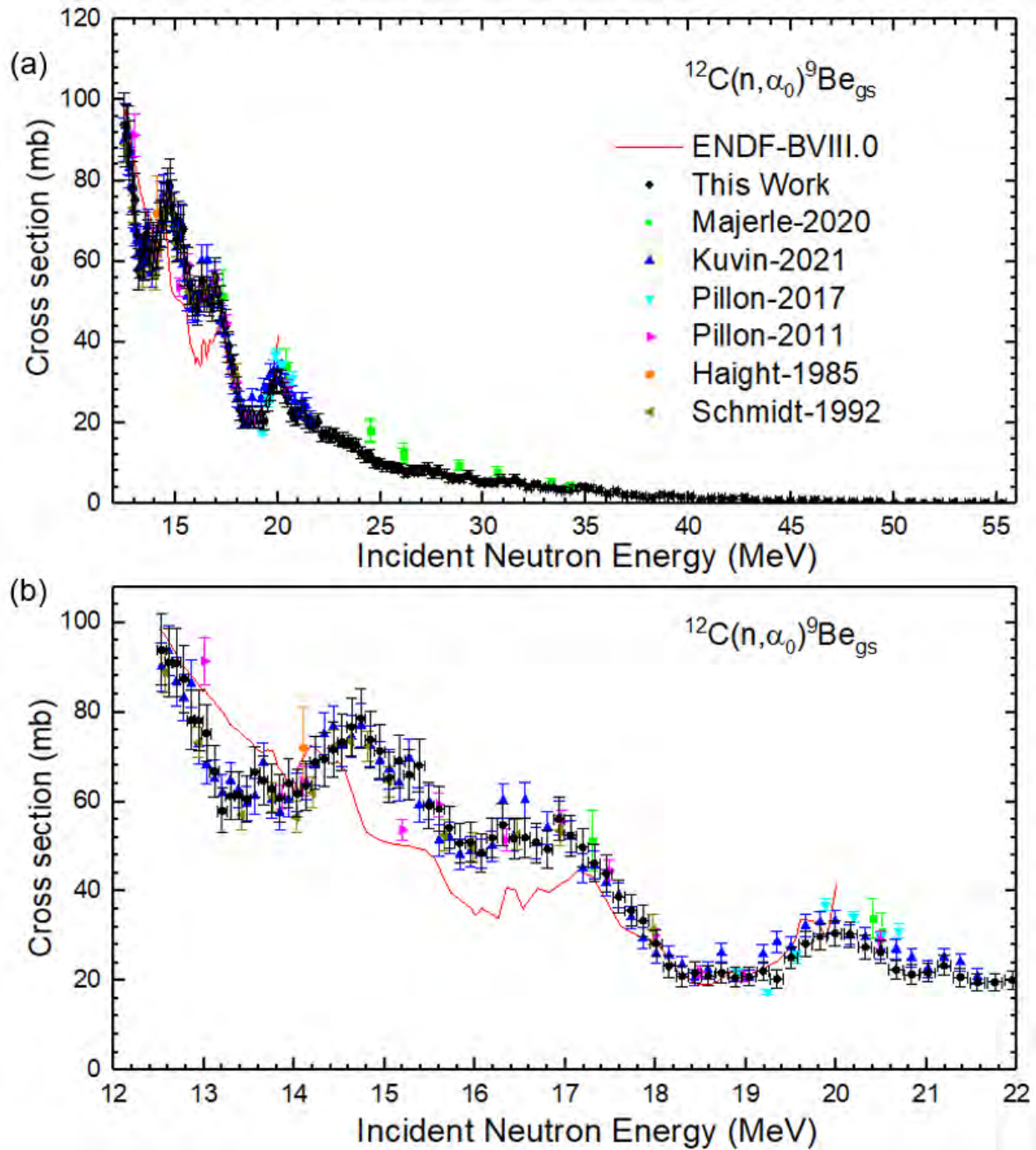


Figure 4.1: Cross sections for the $^{12}\text{C}(n, \alpha)^9\text{Be}$ reaction. The data was normalized to previous $^{12}\text{C}(n, \alpha)^9\text{Be}$ data at 14.1 MeV. This work shows strong agreement with recent data [15, 16, 14, 12, 13, 17]. The five most recent studies used diamond detectors. (a) shows the full range of the measurement in this work, while (b) focuses from 12-22 MeV, where the majority of previous work has been done. Also included is the ENDF/B-VIII.0 evaluation, demonstrating its need to be updated with more recent data.

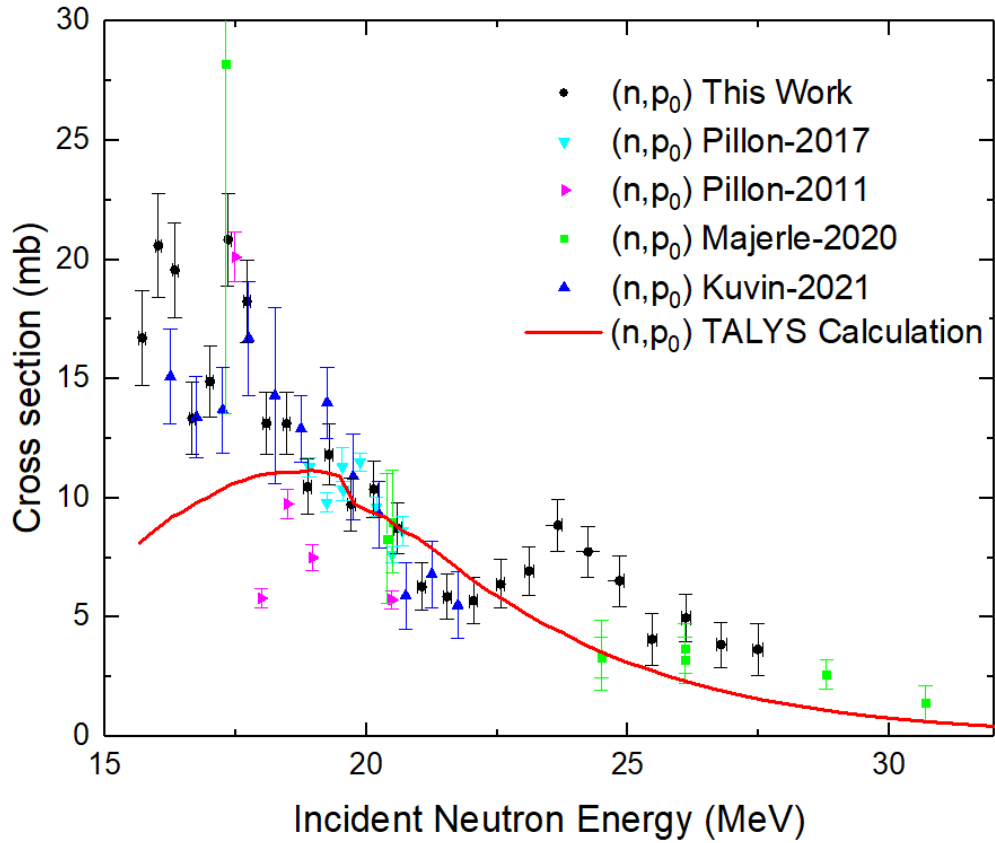


Figure 4.2: Cross sections for the $^{12}\text{C}(n,p_0)^{12}\text{B}$ reaction. The data was normalized to previous $^{12}\text{C}(n,\alpha)^9\text{Be}$ experimental data at 14.1 MeV. This work and previous experimental data are compared to a TALYS calculation using default parameters. Reasonable agreement is shown between this and previous experimental data.

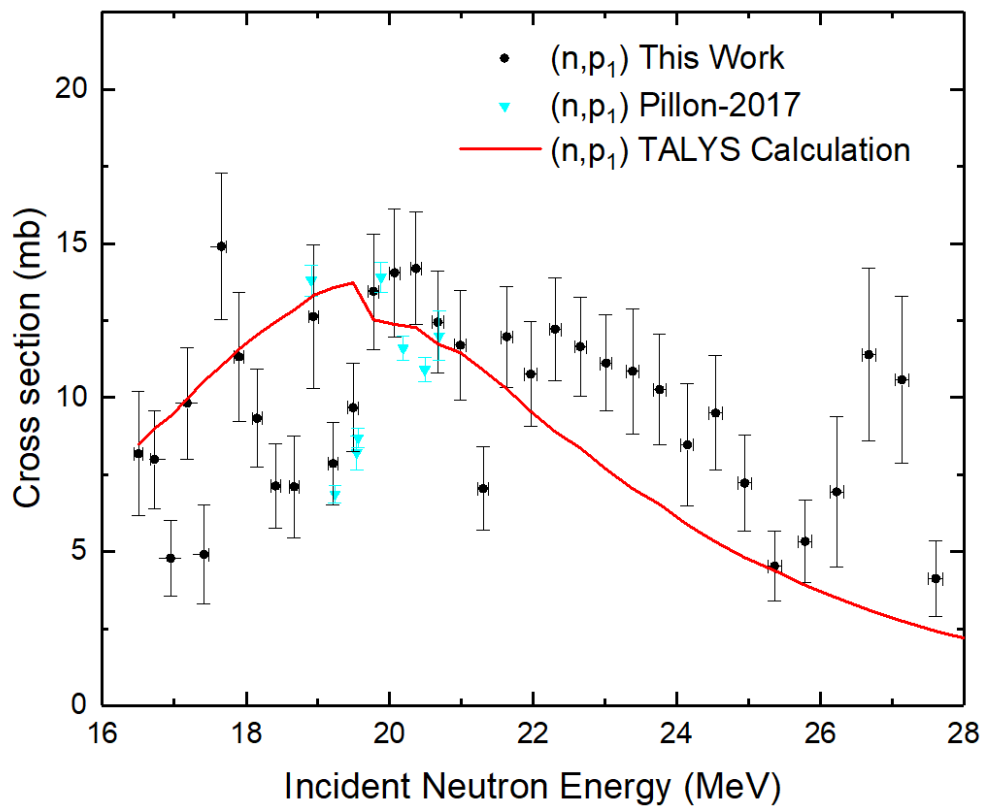


Figure 4.3: Cross sections for the $^{12}\text{C}(n,p_1)^{12}\text{B}$ reaction. The data was normalized to previous $^{12}\text{C}(n,\alpha)^9\text{Be}$ experimental data at 14.1 MeV. This work and previous experimental data are compared to a TALYS calculation using default parameters.

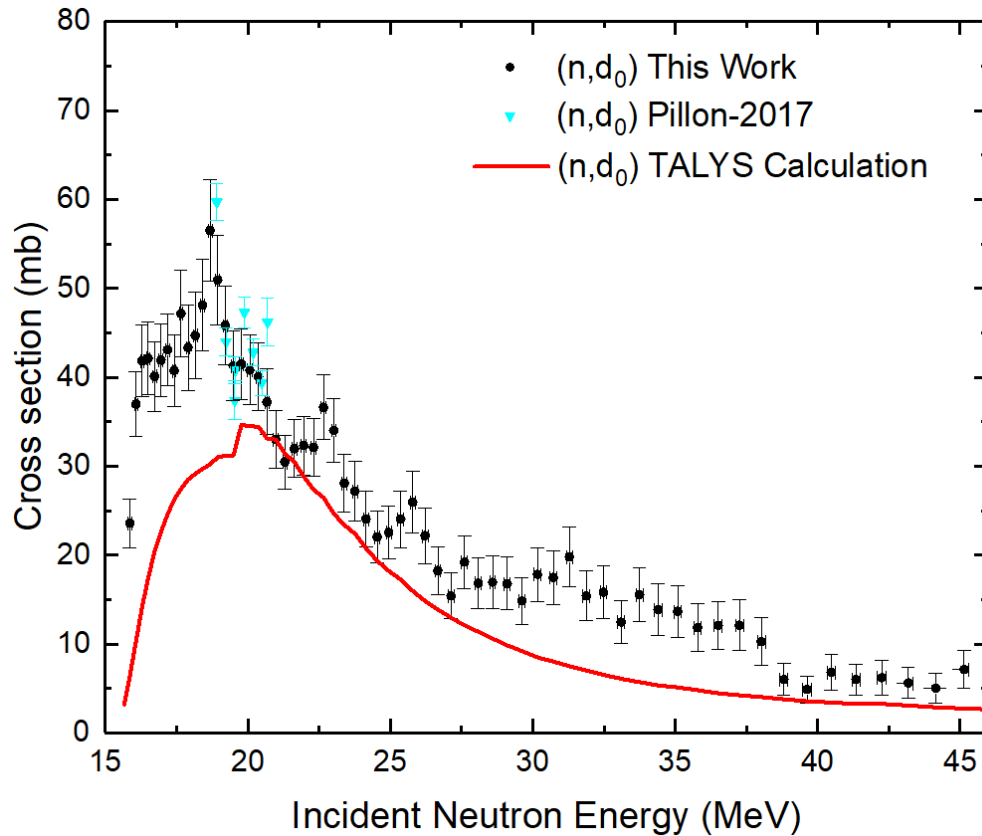


Figure 4.4: Cross sections for the $^{12}\text{C}(n,d)^{11}\text{B}$ reaction. The data was normalized to previous $^{12}\text{C}(n,\alpha)^9\text{Be}$ experimental data at 14.1 MeV. This work and previous experimental data are compared to a TALYS calculation using default parameters.

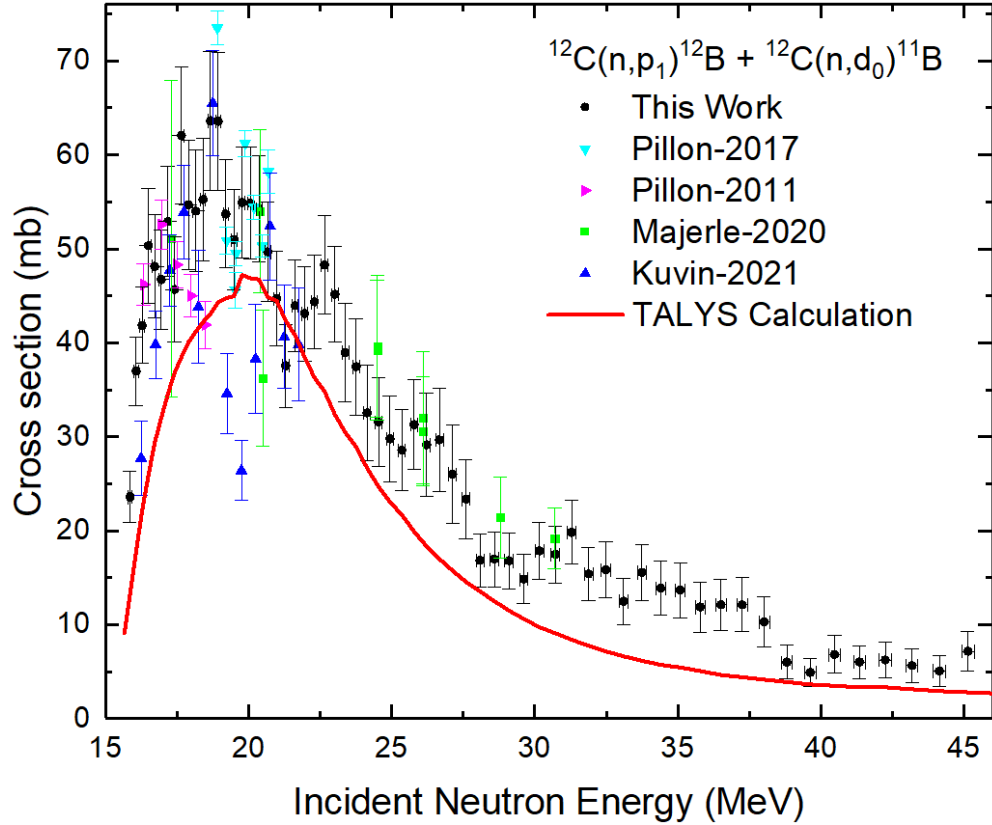


Figure 4.5: Cross sections for $^{12}\text{C}(n,p_1)^{12}\text{B} + ^{12}\text{C}(n,d_0)^{11}\text{B}$. The data was normalized to previous $^{12}\text{C}(n,\alpha)^9\text{Be}$ experimental data at 14.1 MeV. This work and previous experimental data are compared to a TALYS calculation using default parameters. The data for this work and Pillon (2017) were obtained from summing the separate cross sections for $^{12}\text{C}(n,p_1)^{12}\text{B}$ and $^{12}\text{C}(n,d_0)^{11}\text{B}$ in the respective works. The data for Kuvin (2021) were directly taken from the published $^{12}\text{C}(n,d_0 + p_1)$ cross section published in that work. For Pillon (2011) and Majerle (2020), the data were taken from the respective published $^{12}\text{C}(n,d_0)^{11}\text{B}$ cross sections.

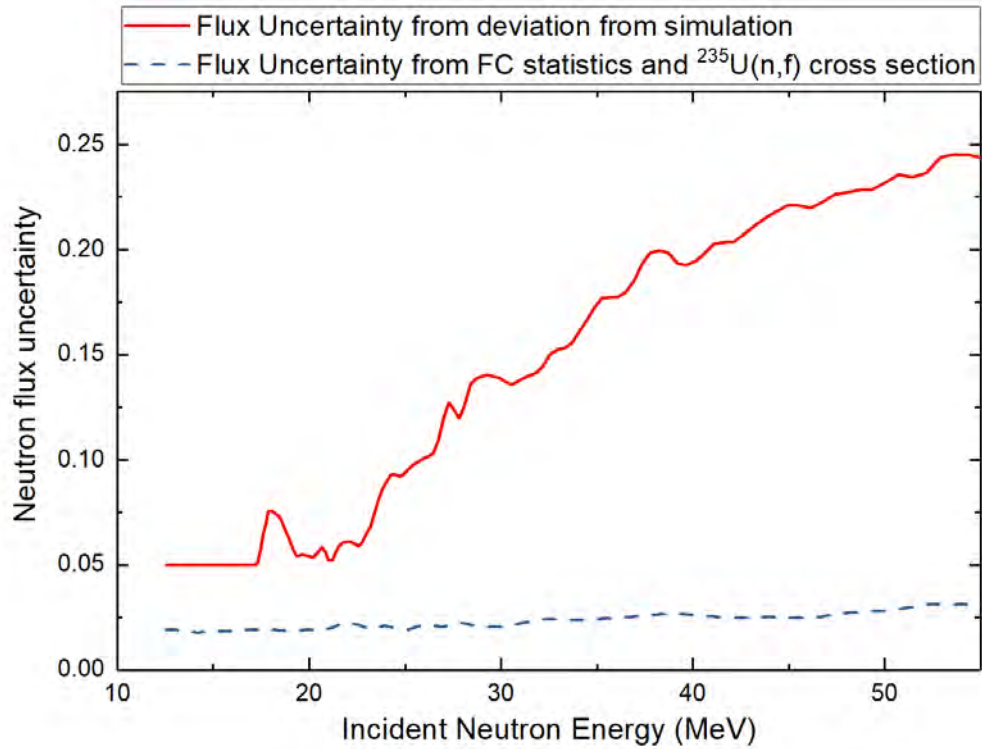


Figure 4.6: A comparison of two methods of quantifying the uncertainty in the neutron flux at the 90 m station. The red curve was used in the cross section uncertainty, and was obtained by the deviation of the fission chamber derived flux from MCNP simulations of the flux. The blue curve demonstrates that the uncertainty in the flux obtained from the fission chamber statistics and the $^{235}\text{U}(n,f)$ reference standard cross sections is much lower. This gives confidence that the flux uncertainty that was used in the cross section uncertainty calculation is an understatement of our confidence in the flux shape. The difference in the two methods of uncertainty quantification can be at least partly attributed to uncertainties in the neutron attenuation correction, which was not separately quantified.

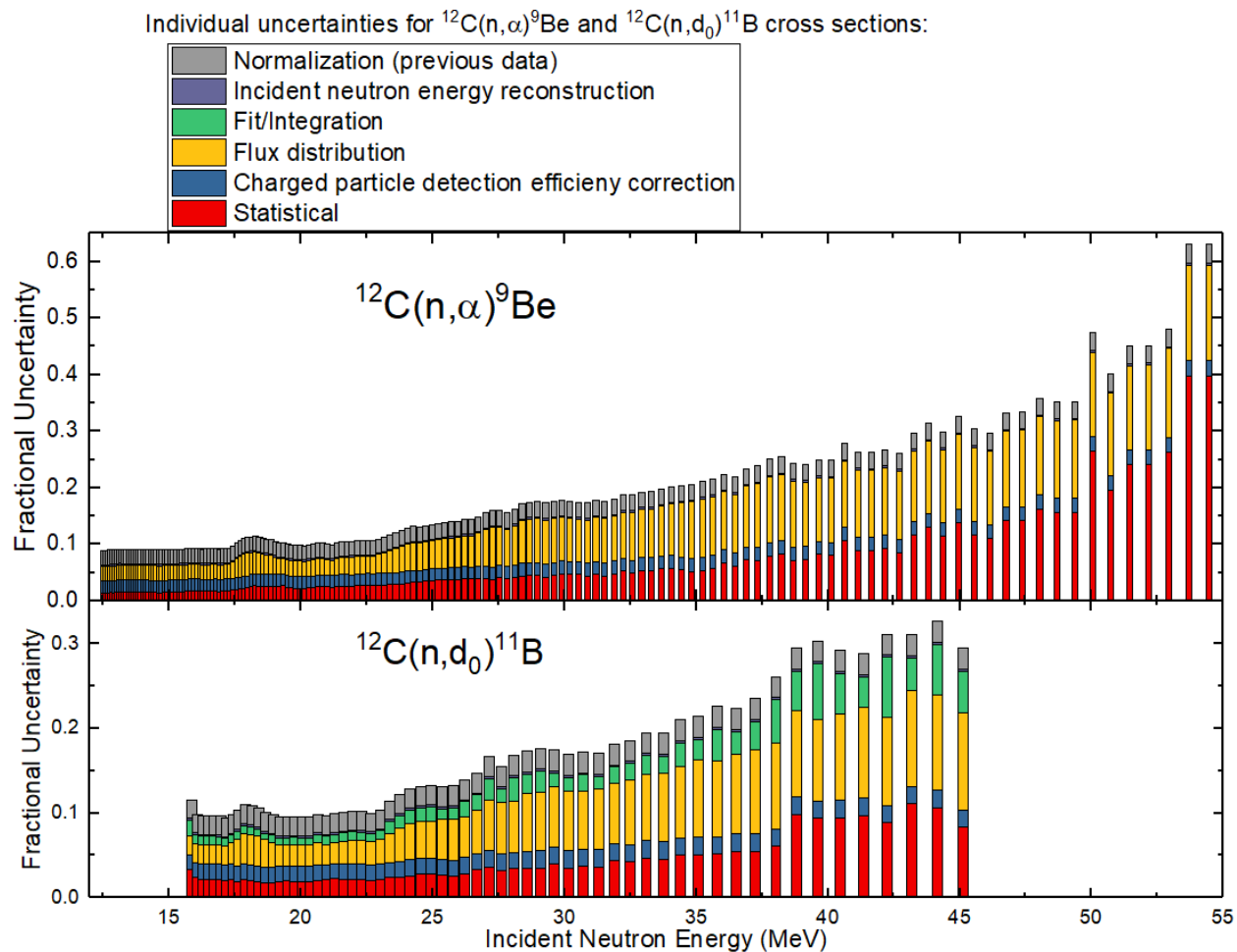


Figure 4.7: Summary of uncertainties that contribute to the $^{12}\text{C}(n,\alpha)^9\text{Be}$ and $^{12}\text{C}(n,d_0)^{11}\text{B}$ cross sections. The total height of each bar shows the total fractional uncertainty at each data point, calculated from the quadrature sum of the individual uncertainties. In this plot, the individual uncertainties (statistical, normalization, etc.) are scaled so that their height represents their percentage of the sum (linear sum) of the uncertainties at each point. The normalization, incident neutron energy reconstruction, and charged particle detection efficiency correction uncertainties are constant, while the fit/integration (for n,d_0), flux distribution, and statistical uncertainties increase significantly at higher energy.

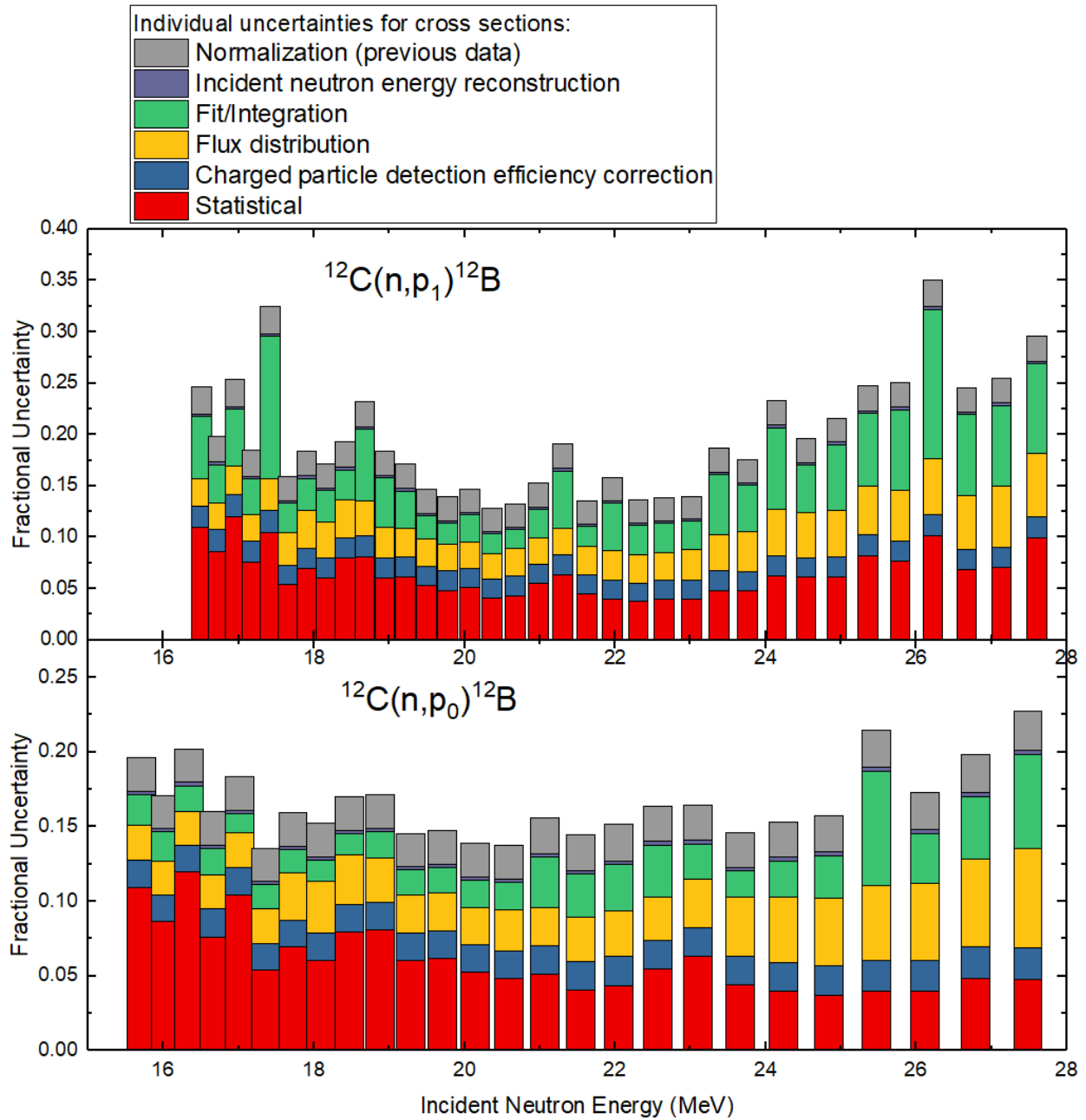


Figure 4.8: Summary of uncertainties that contribute to the $^{12}\text{C}(n,p_0)^{12}\text{B}$ and $^{12}\text{C}(n,p_1)^{12}\text{B}$ cross sections. The total height of each bar shows the total fractional uncertainty at each data point, calculated from the quadrature sum of the individual uncertainties. In this plot, the individual uncertainties (statistical, normalization, etc.) are scaled so that their height represents their percentage of the sum (linear sum) of the uncertainties at each point. The normalization, incident neutron energy reconstruction, and charged particle detection efficiency correction uncertainties are constant, while the fit/integration, flux distribution, and statistical uncertainties increase significantly at higher energy.

4.2 R-matrix fits

R matrix fits of the cross sections were performed with the code AZURE2 [67]. For (n,p_0) , (n,p_1) , and (n,d_0) , the cross section data from the present work were used, due to the larger incident neutron energy range and higher granularity data presented in this work. For (n,α) , the cross sections from Kuvin et al. [15] were used, since their study went lower in incident neutron energy, where the most prominent resonances are. To this point, each reaction channel has been fit individually. Future work will entail performing a multichannel fit with the four exit channels and, perhaps, others, providing better support for the spectroscopic implications of the analysis. In addition, results for branching ratios for the different exit channels can be obtained with a multi-channel fit. For this first pass through the fitting, the focus was placed on obtaining the best possible fit, as evidenced by minimizing the χ^2/N , where N is the number of data points. Through this method, good fits for the reaction channels were obtained. The R-matrix results were compared to NNDC's evaluated levels of ^{13}C [69]. In this section, the comparison with literature is with this evaluation, unless otherwise stated.

4.2.1 $^{12}\text{C}(n,\alpha)^9\text{Be}$

Prominent resonances are observed for the (n,α) channel. Up to about 19 MeV excitation energy, only the (n,α) channel has data that can be fit, for the channels studied in this work. Thus, for this channel, the lower-energy portion of the excitation function would not change based on a multichannel fit with the other channels studied here. Some agreement is shown between the excitation energies of the peaks and the published states of ^{13}C . Some of the troughs may correspond to states of ^{13}C , although levels have not yet been added to the fit to account for the troughs, only the peaks.

The first resonance was observed at $E_x = 12.282$ MeV (J^π $3/2^-$, $\Gamma = 895$ keV). There is a state in the literature at the same excitation energy ($E_x = 12.282$ MeV, $1/2^-$, $\Gamma = 122$ keV). The excitation function was best fit with the $3/2^-$ state, and the width of the fit is much larger than that in literature. Future work will involve verifying this spin-parity assignment. Especially with angle-integrated cross sections, there is no guarantee of a unique solution- different spin-parity assignments may result in a similar fit. Thus, while a $3/2^-$ state produced the best fit of our data, we are not suggesting the accepted spin-parity assignment, $1/2^-$, is incorrect at this time

The second resonance was observed at $E_x = 13.409$ MeV ($5/2^-$, $\Gamma = 496$ keV). The closest energy state in literature is at $E_x = 13.420$ MeV, with tentative J^π assignment ($9/2^-$) and $\Gamma = 41$ keV. However, the angular momentum does not match, although the assignment is uncertain in literature. The width also does not align very well, making this correspondence uncertain, despite the good agreement in the excitation energy.

The third resonance observed has $E_x = 13.544$ MeV ($9/2^-$, $\Gamma = 129$ keV). This matches the previously described state in literature much better ($E_x = 13.420$ MeV, with tentative spin-parity

assignment J^π ($9/2^-$) and $\Gamma = 41$ keV). The J^π determined from the fit agrees with the spin-parity assignment in literature, while the total width matches much closer than the state at 13.409 MeV. Thus, it seems likely that the 13.420 MeV state found in literature corresponds to this third resonance, rather than the second resonance. The fit was better when two levels are included in this region, but both states could not be identified based on the states of ^{13}C .

A fourth resonance was observed at 14.05 MeV, with J^π $7/2^-$, $\Gamma = 1783$ keV. This did not correspond exactly with a single state of ^{13}C . The literature states that are closest in energy have $E_x = 14.13$ MeV, J^π ($3/2^-$, $5/2^-$), $\Gamma = 160$ keV, and $E_x = 13.92$ MeV, unknown J^π , $\Gamma = 100$ keV. Some agreement is also shown with the 14.39 MeV state in literature, which has J^π $7/2^-$, $\Gamma = 282$ keV. Again, more work is needed to verify the characteristics of this state.

A fifth resonance was observed with $E_x = 16.149$ MeV, $5/2^-$, $\Gamma = 548$ keV. This corresponds well with a state found in literature: $E_x = 16.152$ MeV, ($5/2^-$), $\Gamma = 240$ keV. These results could help clear up the uncertainty in the spin-parity assignment found in literature, helping to confirm it as $5/2^-$.

A sixth resonance was found at $E_x = 16.604$ MeV, $7/2^+$, $\Gamma = 658$ keV. There are no states in literature that match the excitation energy, with the nearest state being found at 16.948 MeV. However, the fit improved noticeably when this level was added.

Another resonance was found at $E_x = 17.195$ MeV, $3/2^+$ and an immensely wide width, $\Gamma = 14372$ keV. This resonance is midway between two known states of ^{13}C : 16.948 MeV and 17.363 MeV. The differences in excitation energy between the fit parameter and these states, combined with the unrealistic width, call into question the validity of this resonance. This state originated from another state that we included in the fit, but did not hold the location fixed, and AZURE2 placed it here. Since the fit improved significantly with this state added, we kept it for now.

Another resonance was observed at 18.596 MeV ($3/2^+$, $\Gamma = 1480$ keV). This may correspond to a known state of ^{13}C : 18.699 MeV with J^π ($3/2^+$, $5/2^+$), $\Gamma = 98$ keV, although the widths are not in agreement. Another state is similar in excitation energy, 18.497 MeV, with unknown J^π and $\Gamma = 91$ keV, but has not been observed as many times as the 18.699 MeV state.

A final resonance was observed at $E_x = 23.035$ MeV, $5/2^+$, $\Gamma = 67844$ keV. A state of ^{13}C has been observed at 23.0 MeV, with J^π ($3/2^+$, $5/2^+$) and $\Gamma \approx 1.5$ MeV. The width from our fits was much larger and is not a realistic value. Including a state in this excitation energy brought the fit much closer to the experimental data. When the width of the state was fixed with a more reasonable value (i.e. closer to literature), the fit was much worse, so for the fit displayed, the width was not held as a fixed parameter. Further adjustment of parameters is needed to clear up this discrepancy.

4.2.2 $^{12}\text{C}(n, p_0)^{12}\text{B}$

The resonances observed in the (n, p_0) excitation function were not as prominent as those of the (n, α) . However, up to three possible resonances are observed. Reasonable agreement is shown

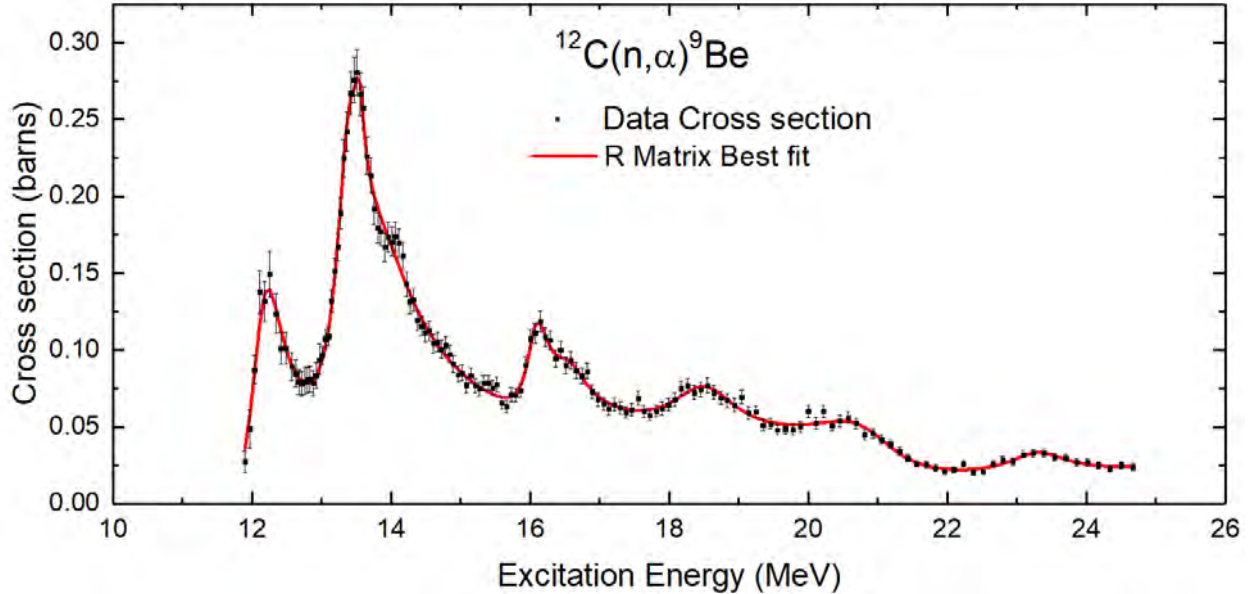


Figure 4.9: R matrix best fit for $^{12}\text{C}(n,\alpha)^9\text{Be}$ cross sections, performed with AZURE2. The black data points are the published cross sections from Kuvín *et al.* [15], with the published uncertainties as well. The red curve is the R matrix best fit.

between the R-matrix best fit results and the states of ^{13}C found in literature [69]. The first resonance for this channel, at 19.90 MeV, matches the excitation energy of a state in literature (19.9 MeV), with no accepted J^π , and with an approximate width of 600 keV. This published width [69] differs from the width we determined from our fit, 1356 keV, but is within the same order of magnitude. There is another literature state that this resonance could correspond to (20.111 MeV, $1/2^-$, $\Gamma = 1090$ keV), but there is more confidence in the energy of a resonance than the width.

The second resonance observed in this channel ($E_x = 21.15$ MeV) matches reasonably well with the literature state ($E_x = 21.050$ MeV, $\Gamma = 4.2$ MeV). The width from our fit was 3335 keV, in reasonable agreement with the literature value [69]. There is no accepted spin and parity for this state, but we found it was best fit with $1/2^-$.

A possible broad resonance was observed at $E_x = 27$ MeV. This does not match up with previously observed states of ^{13}C , with the two closest levels at 26.791 and 27.466 MeV. There is no accepted spin-parity assignment or total width for either state, making it impossible to determine which, if either, state this resonance corresponds to.

4.2.3 $^{12}\text{C}(n,p_1)^{12}\text{B}$

This channel features one possible resonance around $E_x = 21.2$ MeV and either two broad resonances or one very broad resonance at higher energies. For this channel, the literature states were used to inform the initial fit parameters. Thus, good agreement is observed between the output parameters

Table 4.2: Resonance parameters from the R matrix fits performed with AZURE2 for $^{12}\text{C}(n,\alpha)^9\text{Be}$.

E_x (MeV)	J^π	Γ (keV)
12.282	$3/2^-$	895
13.409	$5/2^-$	496
13.544	$9/2^-$	129
14.050	$7/2^-$	1783
16.149	$5/2^-$	548
16.604	$7/2^+$	658
17.195	$3/2^+$	14372
18.596	$3/2^+$	1480
23.035	$5/2^+$	67844

for the R-matrix fit and those of the literature states.

The first resonance at $E_x = 21.28$ MeV corresponds to a state with the same energy in literature [69], but the widths differ (160 keV in literature, 876 keV in this work). There is no accepted spin-parity assignment for this state, but a $1/2^+$ state was found to produce the best fit.

A very broad state is found in literature ($E_x = 24$ MeV, $\Gamma = 10$ MeV) where we observed a broad hump in our excitation function ($E_x = 24$ MeV, $\Gamma = 7675$ keV). There is no accepted spin-parity assignment for this state in literature [69], but we found that it was best fit with a $5/2^+$ state.

Lastly, a broad hump is observed around $E_x = 26$ MeV in our data. A state was observed in literature [69] at $E_x = 26?$ MeV, but with no accepted spin-parity assignment or total width. Our best fit of the data featured a state with $E_x = 25.99$ MeV, $J^\pi = 5/2^-$, $\Gamma = 5142$ keV.

Again, it should be mentioned that this channel had higher uncertainties than the others, due to lower statistics and the close proximity of the (n,d_0) peak affecting the quality of the peak fitting to obtain the counts. Thus, we have less certainty in the R-matrix results of this channel compared to others.

4.2.4 $^{12}\text{C}(n,d_0)^{11}\text{B}$

Three fairly distinct resonances are observed for this channel. The first resonance was fit best with $E_x = 22.23$ MeV, $5/2^-$, $\Gamma = 2989$ keV. This matches reasonably well with a state in literature [69] ($E_x = 22.2$ MeV, $\leq 5/2$, $\Gamma = 1.1$ MeV). The spin-parity assignment from the fit clarifies this uncertain assignment in literature. However, it is worth noting that the data was fit almost as well with a $1/2^+$ state, which is also possible according to literature.

A second resonance was observed around 26 MeV and was best fit with a state at $E_x = 25.95$ MeV, $1/2^+$, $\Gamma = 4840$ keV. This may correspond to a state found in literature [69] at $E_x = 26$ MeV, but it is difficult to confirm since there is not an accepted width or spin-parity assignment in literature [69]. This state is very close in energy to the 25.99 MeV state observed from the (n,p_1)

Table 4.3: Resonance parameters from the R matrix fits performed with AZURE2 for $^{12}\text{C}(n,p_0)^{12}\text{B}$, $^{12}\text{C}(n,p_1)^{12}\text{B}$, and $^{12}\text{C}(n,d_0)^{11}\text{B}$.

$^{12}\text{C}(n,p_0)^{12}\text{B}$			$^{12}\text{C}(n,p_1)^{12}\text{B}$			$^{12}\text{C}(n,d_0)^{11}\text{B}$		
E_x (MeV)	J^π	Γ (keV)	E_x (MeV)	J^π	Γ (keV)	E_x (MeV)	J^π	Γ (keV)
19.90	$1/2^-$	1356	21.28	$1/2^+$	876	22.23	$5/2^-$	2989
21.15	$1/2^-$	3335	24.00	$5/2^+$	7675	25.95	$1/2^+$	4840
27.00	$7/2^+$	1666	25.99	$5/2^-$	5142	28.75	$1/2^-$	25200
Background States			Background States			Background States		
35.00	$1/2^-$	3108	35.00	$1/2^-$	5000	35.00	$1/2^-$	951000
35.00	$1/2^+$	5000	35.00	$1/2^+$	0.0045	35.00	$1/2^+$	771000
35.00	$3/2^-$	5000	35.00	$3/2^-$	5000	35.00	$3/2^-$	5000
35.00	$3/2^+$	5000	35.00	$3/2^+$	5000	35.00	$3/2^+$	1288
35.00	$5/2^-$	5000	35.00	$5/2^-$	5000	35.00	$5/2^-$	899900
35.00	$5/2^+$	5000	35.00	$5/2^+$	0.011	35.00	$5/2^+$	5000
35.00	$7/2^-$	917	35.00	$7/2^-$	5000	35.00	$7/2^-$	5000
35.00	$7/2^+$	5000	35.00	$7/2^+$	5000	35.00	$7/2^+$	5000

fit, which was best fit with a $5/2^-$ state, but with a similar total width. This could benefit from a multichannel fit to help clear up the discrepancy.

Finally, the excitation function was best fit with a third resonance with $E_x = 28.75$ MeV, $1/2^-$, $\Gamma = 25200$ keV. This immensely broad resonance does not correspond to any known states in literature, as the nearest two states are about 1.3 MeV away (27.466 and 30 MeV, respectively). However, the χ^2/N improved when the state was added. Further analysis is required to see how the fit is affected by the presence of the state and its parameters.

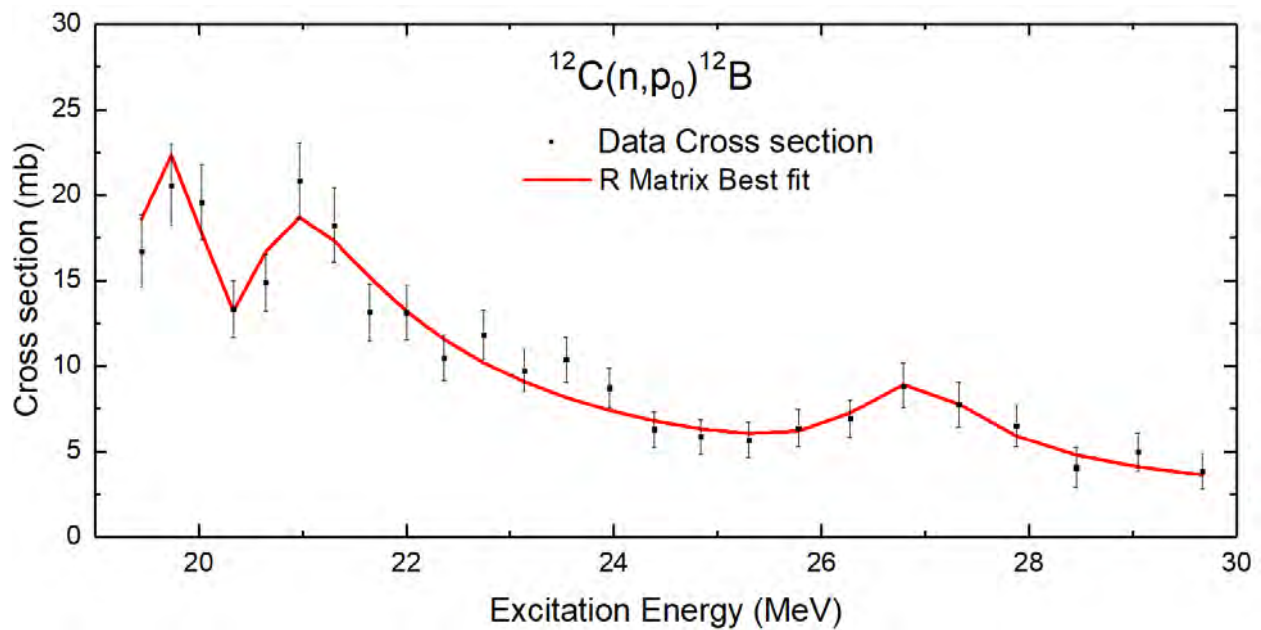


Figure 4.10: R matrix best fit for $^{12}\text{C}(n,p_0)^{12}\text{B}$ cross sections, performed with AZURE2. The black data points are the cross sections from the present work, with their uncertainties. The red curve is the R matrix best fit.

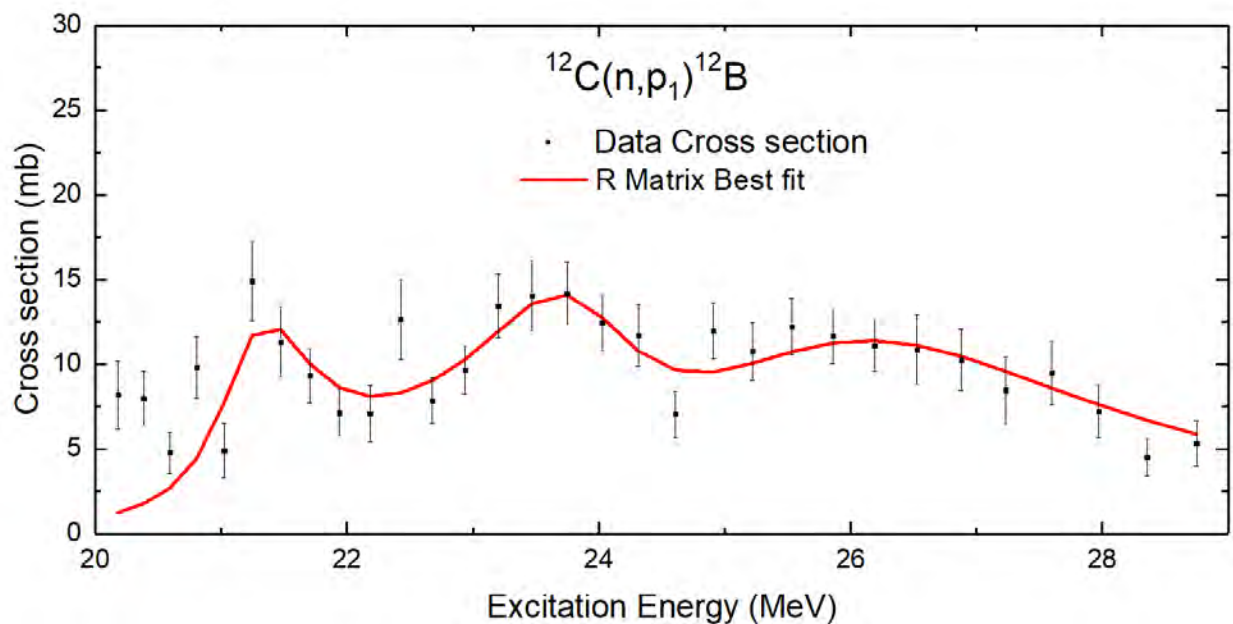


Figure 4.11: R matrix best fit for $^{12}\text{C}(n,p_1)^{12}\text{B}$ cross sections, performed with AZURE2. The black data points are the cross sections from the present work, with their uncertainties. The red curve is the R matrix best fit.

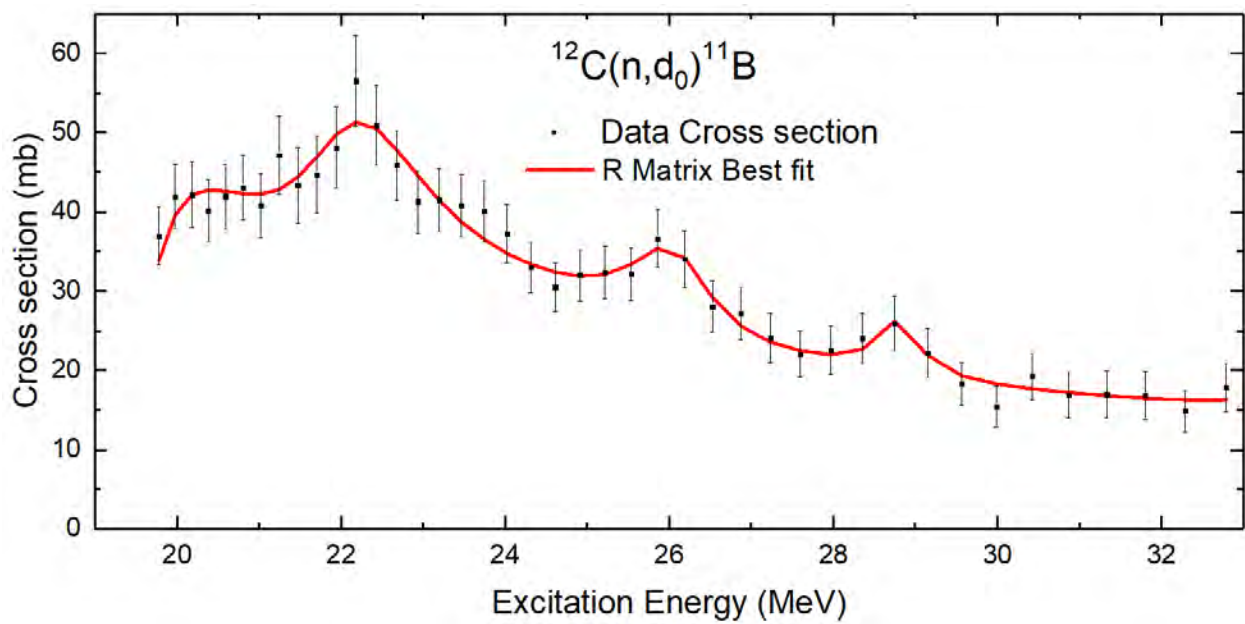


Figure 4.12: R matrix best fit for $^{12}\text{C}(n,d_0)^{11}\text{B}$ cross sections, performed with AZURE2. The black data points are the cross sections from the present work, with their uncertainties. The red curve is the R matrix best fit.

4.3 MENATE_R Improvements

Numerous improvements were made to the reaction channels available in MENATE_R and the cross sections for those and existing channels. In this section, the changes to MENATE_R are laid out in detail.

4.3.1 New Channels in MENATE_R

To improve MENATE_R's treatment of n-C interactions, new channels were added. To start, $^{12}\text{C}(n,d_0)^{11}\text{B}$ and $^{12}\text{C}(n,t_0)^{10}\text{B}$ channels were added. These are crucial since deuteron and triton production were not included in MENATE_R prior to this. Next, the (n,p), (n,d), and (n,t) channels were divided into separate channels corresponding to which state of the daughter nucleus (^{12}B , ^{11}B , or ^{10}B) was populated. The population of excited states of the daughter nucleus affects the kinematics by removing kinetic energy from the reaction products. Thus, an accurate simulation of these processes requires separate treatments for each state. For this version of MENATE_R, the decay of unstable daughter nuclei is not simulated, since the time scale of these decays is much larger than the typical event windows for fast beam experiments. These decays do lead to an uncorrelated gamma ray background ranging from hundreds of keV to a few MeV that affects event reconstruction. This effect may be addressed in future versions of MENATE_R. The current version of the code is available in an online repository [70]. At this time, the updates to MENATE_R have been implemented in NPTool. Future work may also involve updating GEANT4 to use the new version of MENATE_R.

4.3.2 Cross section updates in MENATE_R

For each new channel and some existing channels, the cross sections in MENATE_R were updated to take into account the most recent data. The channels for which new cross sections were added will now be listed.

$^{12}\text{C}(n,\alpha)^9\text{Be}$:

The n, α channel was updated to account for the most recent data taken with diamond detectors. From just above threshold to 21.56 MeV, the cross sections for this channel are taken from the work of Kuvin *et al.* in 2021 [15]. Above 21.56 MeV, the cross sections are taken from the present work. These cross sections offer much higher granularity than the previous MENATE_R offerings, and account for the strong resonant behavior of this channel. Since there are no bound excited states of ^9Be , this channel did not need to be updated further to separately treat each excited state. Instead, excited states of ^9Be undergo alpha breakup into $2\alpha + n$, that is, the $^{12}\text{C}(n,n'+3\alpha)$ channel, which was not addressed in this work. A comparison of the old (n, α) cross section and the updated version is shown in Fig. 4.13. The updated MENATE_R cross section features larger cross sections in the low-energy resonance region, but much smaller cross sections above 15 MeV.

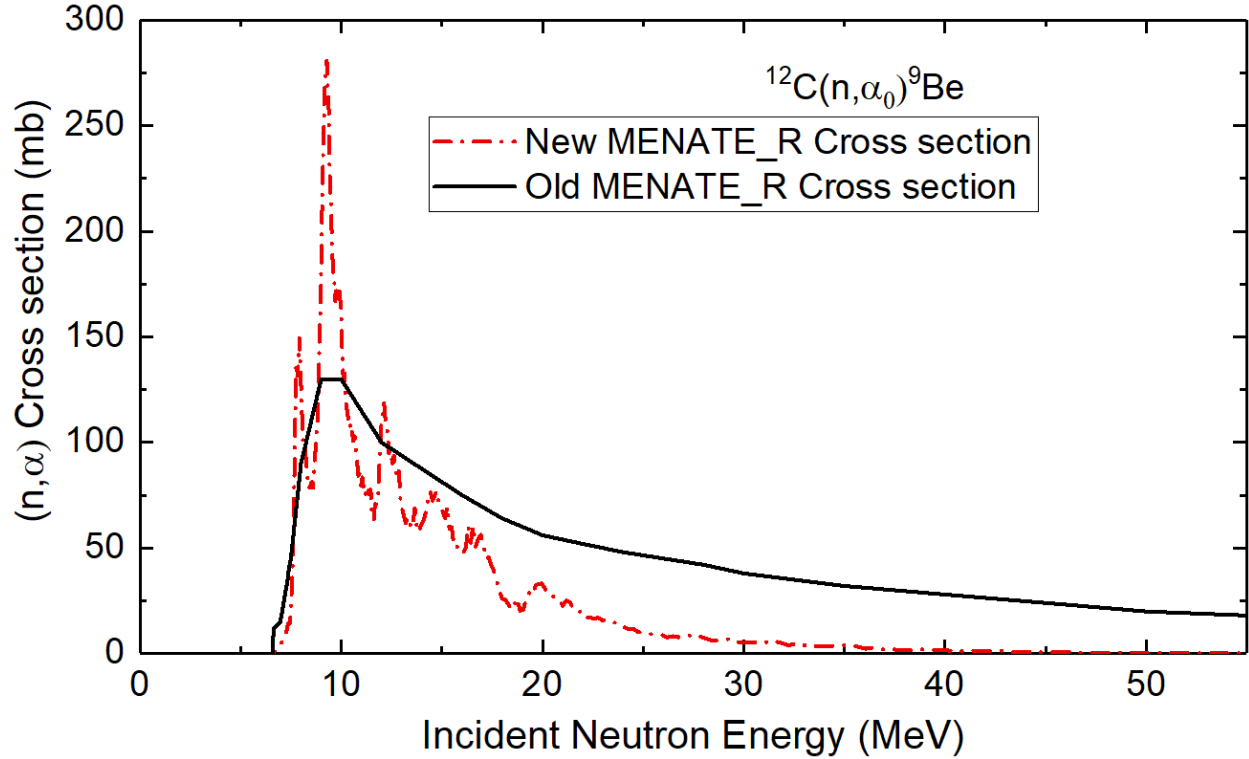


Figure 4.13: Cross sections for the $^{12}\text{C}(n,\alpha)^9\text{Be}$ reaction, comparing the old version of MENATE_R and the new version. The data for the new version was normalized to previous $^{12}\text{C}(n,\alpha)^9\text{Be}$ data at 14.1 MeV. The new version offers much higher granularity, and the resonances that characterize this cross section are visible.

$^{12}\text{C}(n,p_0)^{12}\text{B}$:

As previously mentioned, the (n,p) channel was broken up into separate channels to account for the population of each excited state in ^{12}B . Thus, the former cross section file, Carbon12_np12B.dat, containing inclusive cross sections, needed to be updated. This reaction channel now exclusively refers to the population of ^{12}B in the ground state ($J^\pi = 1^+$, $E_x = 0$), and uses the same kinematics and Q value as the previous combined $^{12}\text{C}(n,p)^{12}\text{B}$ channel. The cross section for this channel was taken from the present work.

$^{12}\text{C}(n,p_1)^{12}\text{B}$:

This channel refers to production of a proton and ^{12}B in the first excited state (2^+ , $E_x = 0.953$ MeV). This cross section was also taken from the present work. The cross section file for this is Carbon12_np_1_12B.dat. The Q value for the reaction was set to -13.54 MeV.

$^{12}\text{C}(n,p_2)^{12}\text{B}$:

This channel refers to production of a proton and ^{12}B in the second excited state (2^- , $E_x = 1.673$ MeV). The data for this peak in the present work have not yet been analyzed, and thus the cross section for the (n,p_0) reaction was used as a placeholder. The threshold was adjusted to account for the kinematic differences between the two reactions. The cross section file for this is Carbon12_np_2_12B.dat. The Q value was set to -14.26 MeV.

$^{12}\text{C}(n,p_3)^{12}\text{B}$:

Since the (n,p_3) and the (n,p_4) channels have very similar excitation energies, indistinguishable in the current study, they are treated identically in this simulation. The Q value was set to that of (n,p_3) , -15.208 MeV. This channel in MENATE_R refers to production of a proton and ^{12}B in the third excited state (1^- , $E_x = 2.6208$ MeV) or the fourth excited state, (0^+ , $E_x = 2.723$ MeV). The data for this peak in the present work have not yet been analyzed, and thus the cross section for the (n,p_0) reaction was used as a placeholder. The threshold was adjusted to account for the kinematic differences between this and (n,p_0) . The cross section file for this is Carbon12_np_3_12B.dat. Thus, the cross sections contained in Carbon12_np_3_12B.dat represent those of the combined $^{12}\text{C}(n,p_3)^{12}\text{B} + ^{12}\text{C}(n,p_4)^{12}\text{B}$ cross section. Fig. 4.14 shows a comparison of the $^{12}\text{C}(n,p)^{12}\text{B}$ cross sections in the old and new versions of MENATE_R. Since the cross sections for (n,p_2) and (n,p_3+p_4) have not been measured yet in the current study, and the (n,p_0) reaction was used as a place holder, the new cross sections for these channels lie on top of each other. This overemphasizes the resonances observed in the (n,p_0) channel when all the new channels are summed together, to the point that the new total $^{12}\text{C}(n,p)^{12}\text{B}$ cross section is much higher than the old $^{12}\text{C}(n,p)^{12}\text{B}$ cross section for $15 \leq E_n \leq 20$ MeV. Since the (n,p_2) and (n,p_3+p_4) channels have smaller cross sections than the (n,p_0) and (n,p_1) , when these channels are measured and updated in MENATE_R, they will bring the total cross section much closer to old (n,p) cross section below 22 MeV. Above 22 MeV, the old (n,p) cross section increases rapidly, contrary to the reduction observed in the data of the present work, other recent studies, and TALYS reaction code predictions (see Fig. 4.2). Extending the measurements of the $^{12}\text{C}(n,p)^{12}\text{B}$ cross section beyond 30 MeV will be crucial for further improving this channel's treatment in simulation.

All other states of ^{12}B (above the 4th excited state) are above the neutron separation energy ($E_x = 3.369$ MeV). Although it is possible to populate these states, events corresponding to these states will not show up in a sharp peak in a diamond detector spectrum, since they are neutron unbound. Almost instantaneously, the excited ^{12}B nucleus will decay into $^{11}\text{B} + n$, and the neutron will typically escape the detector with some of the kinetic energy. This is kinematically the same as the $^{12}\text{C}(n,np)^{11}\text{B}$ reaction, which is already included in MENATE_R. At this time, there is no separate treatment of these excited states in the simulation, since cross sections cannot be obtained with this data set. Potentially reasonable cross sections could be obtained from a TALYS calculation, but

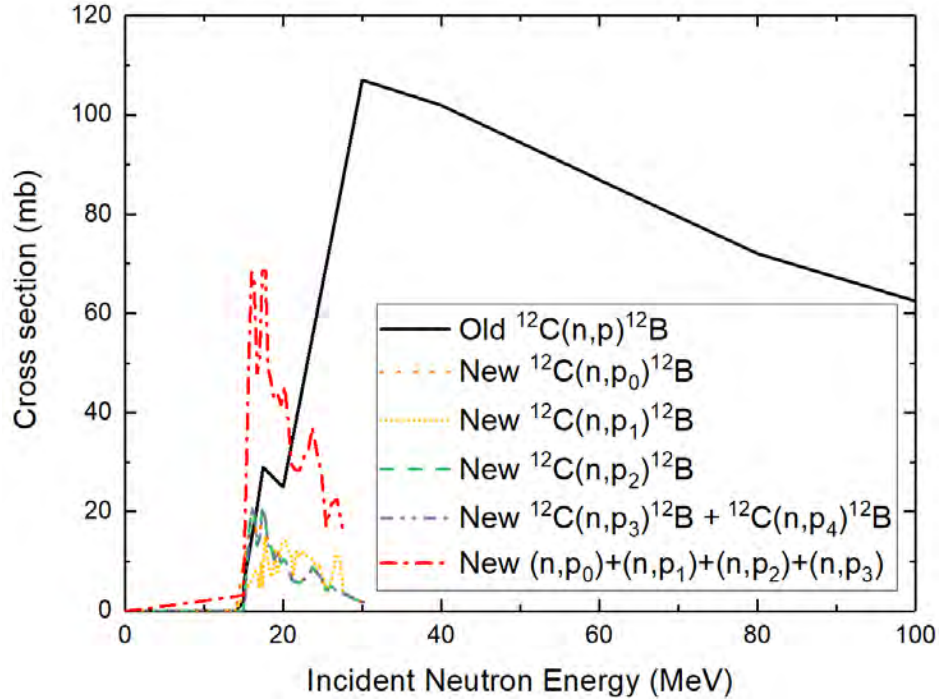


Figure 4.14: Cross sections for $^{12}\text{C}(n,p)^{12}\text{B}$, comparing the old version of MENATE_R and the new version. The “New $^{12}\text{C}(n,p_0)^{12}\text{B}$ ” and “New $^{12}\text{C}(n,p_1)^{12}\text{B}$ ” cross sections use the real data measured in this work. The “New $^{12}\text{C}(n,p_2)^{12}\text{B}$ ” and “New $^{12}\text{C}(n,p_3)^{12}\text{B} + ^{12}\text{C}(n,p_4)^{12}\text{B}$ ” cross sections have not yet been measured in the present work, so the $^{12}\text{C}(n,p_0)^{12}\text{B}$ data was used as a placeholder, hence the (n,p_0) , (n,p_2) , (n,p_3+p_4) curves lie on top of one another. This overemphasizes the resonances present in this reaction. The data for the new version was normalized to previous $^{12}\text{C}(n,\alpha)^9\text{Be}$ data at 14.1 MeV. The new version offers much higher granularity, and the resonances that characterize these cross sections are visible.

the resonant behavior that characterizes the cross sections in this energy range would be absent. If an experiment was conducted with a dedicated setup including neutron and gamma ray detection, the cross sections for these unbound states could potentially be determined.

$^{12}\text{C}(n,d_0)^{11}\text{B}$:

As previously mentioned, the newly added (n,d) channel was broken up into separate channels to account for the population of each excited state in ^{11}B . This reaction channel exclusively refers to the population of ^{11}B in the ground state ($J^\pi = 3/2^-$, $E_x = 0$). The cross section for this channel was taken from the present work and is stored in Carbon12_nd11B.dat. The Q value is -13.732 MeV.

$^{12}\text{C}(n,d_1)^{11}\text{B}$:

This reaction channel refers to production of a deuteron and the population of ^{11}B in the first excited state ($J^\pi = 1/2^-$, $E_x = 2.124$ MeV). The data for this peak in the present work have not yet been analyzed, and thus the cross section for the (n,d_0) reaction was used as a placeholder. This considerably overestimates the cross section for this channel. The placeholder cross section for this channel is stored in Carbon12_nd_1_11B.dat. The Q value is -15.857 MeV.

$^{12}\text{C}(n,d_2)^{11}\text{B}$:

This reaction channel refers to production of a deuteron and the population of ^{11}B in the second excited state ($J^\pi = 5/2^-$, $E_x = 4.445$ MeV). The data for this peak in the present work have not yet been analyzed, and thus the cross section for the (n,d_0) reaction was used as a placeholder. This considerably overestimates the cross section for this channel. The placeholder cross section for this channel is stored in Carbon12_nd_2_11B.dat. The Q value is -18.177 MeV.

$^{12}\text{C}(n,d_3)^{11}\text{B}$:

This reaction channel refers to production of a deuteron and the population of ^{11}B in the third excited state ($J^\pi = 3/2^-$, $E_x = 5.02$ MeV). The data for this peak in the present work have not yet been analyzed, and thus the cross section for the (n,d_0) reaction was used as a placeholder. This considerably overestimates the cross section for this channel. The placeholder cross section for this channel is stored in Carbon12_nd_3_11B.dat. The Q value is -18.75 MeV.

$^{12}\text{C}(n,d_4)^{11}\text{B}$ and $^{12}\text{C}(n,d_5)^{11}\text{B}$:

Since the (n,d_4) and the (n,d_5) channels have very similar excitation energies, indistinguishable in the current study, they are treated identically in this simulation. This reaction channel in MENATE_R refers to production of a deuteron and the population of ^{11}B in the fourth excited state ($J^\pi = 7/2^-$, $E_x = 6.742$ MeV) or the fifth excited state ($J^\pi = 1/2^+$, $E_x = 6.792$ MeV). The data for this peak in the present work have not yet been analyzed, and thus the cross section for the (n,d_0) reaction was used as a placeholder. This considerably overestimates the cross section for this channel. The placeholder cross sections for these channels are stored in Carbon12_nd_4_11B.dat. The Q value was set to -20.47 MeV, matching that of the $E_x = 6.742$ MeV state.

$^{12}\text{C}(n,d_6)^{11}\text{B}$:

This reaction channel refers to production of a deuteron and the population of ^{11}B in the sixth excited state ($J^\pi = 5/2^+$, $E_x = 7.285$ MeV). The data for this peak in the present work have not yet been analyzed, and thus the cross section for the (n,d_0) reaction was used as a placeholder. This considerably overestimates the cross section for this channel. The placeholder cross section for this channel is stored in Carbon12_nd_5_11B.dat. The Q value is -21.02 MeV.

$^{12}\text{C}(n,d_7)^{11}\text{B}$:

This reaction channel refers to production of a deuteron and the population of ^{11}B in the seventh excited state ($J^\pi = 3/2^+$, $E_x = 7.978$ MeV). The data for this peak in the present work have not yet been analyzed, and thus the cross section for the (n,d_0) reaction was used as a placeholder. This considerably overestimates the cross section for this channel. The placeholder cross section for this channel is stored in Carbon12_nd_6_11B.dat. The Q value is -21.71 MeV.

$^{12}\text{C}(n,d_8)^{11}\text{B}$:

This reaction channel refers to production of a deuteron and the population of ^{11}B in the eighth excited state ($J^\pi = (3/2^-)$, $E_x = 8.56$ MeV). The data for this peak in the present work have not yet been analyzed, and thus the cross section for the (n,d_0) reaction was used as a placeholder. This considerably overestimates the cross section for this channel. The placeholder cross section for this channel is stored in Carbon12_nd_7_11B.dat. The Q value is -22.29 MeV.

Most of the remaining states of ^{11}B below the neutron separation energy ($E_x = 11.454$ MeV) are alpha unbound, so they are effectively $^{12}\text{C}(n,d+\alpha)^7\text{Li}$. These have not yet been incorporated into MENATE_R.

$^{12}\text{C}(n,t_0)^{10}\text{B}$:

This reaction channel refers to production of a triton and the population of ^{10}B in the ground state ($J^\pi = 3^+$, $E_x = 0$). The data for this peak in the present work have not yet been analyzed. A placeholder cross section for this reaction was obtained from the average of the (n,d_0) and the (n,p_1) reaction. This considerably overestimates the cross section for this channel. The placeholder cross section for this channel is stored in Carbon12_nt10B.dat. The Q value is -18.929 MeV.

$^{12}\text{C}(n,t_1)^{10}\text{B}$:

This reaction channel refers to production of a triton and the population of ^{10}B in the first excited state ($J^\pi = 1^+$, $E_x = 0.718$ MeV). The data for this peak in the present work have not yet been analyzed. A placeholder cross section for this reaction was obtained from the average of the (n,d_0) and the (n,p_1) reaction. This considerably overestimates the cross section for this channel. The placeholder cross section for this channel is stored in Carbon12_nt_1_10B.dat. The Q value is -19.65 MeV.

$^{12}\text{C}(n,t_2)^{10}\text{B}$:

This reaction channel refers to production of a triton and the population of ^{10}B in the second excited state ($J^\pi = 0^+$, $E_x = 1.740$ MeV). The data for this peak in the present work have not yet been analyzed. A placeholder cross section for this reaction was obtained from the average of the

(n,d₀) and the (n,p₁) reaction. This considerably overestimates the cross section for this channel. The placeholder cross section for this channel is stored in Carbon12_nt_2_10B.dat. The Q value is -20.669 MeV.

$^{12}\text{C}(n,t_3)^{10}\text{B}$:

This reaction channel refers to production of a triton and the population of ^{10}B in the third excited state ($J^\pi = 1^+$, $E_x = 2.154$ MeV). The data for this peak in the present work have not yet been analyzed. A placeholder cross section for this reaction was obtained from the average of the (n,d₀) and the (n,p₁) reaction. This considerably overestimates the cross section for this channel. The placeholder cross section for this channel is stored in Carbon12_nt_3_10B.dat. The Q value is -21.08 MeV.

$^{12}\text{C}(n,t_4)^{10}\text{B}$:

This reaction channel refers to production of a triton and the population of ^{10}B in the fourth excited state ($J^\pi = 2^+$, $E_x = 3.587$ MeV). The data for this peak in the present work have not yet been analyzed. A placeholder cross section for this reaction was obtained from the average of the (n,d₀) and the (n,p₁) reaction. This considerably overestimates the cross section for this channel. The placeholder cross section for this channel is stored in Carbon12_nt_4_10B.dat. The Q value is -22.516 MeV.

$^{12}\text{C}(n,t_5)^{10}\text{B}$:

This reaction channel refers to production of a triton and the population of ^{10}B in the fifth excited state ($J^\pi = 3^+$, $E_x = 4.774$ MeV). The data for this peak in the present work have not yet been analyzed. A placeholder cross section for this reaction was obtained from the average of the (n,d₀) and the (n,p₁) reaction. This considerably overestimates the cross section for this channel. The placeholder cross section for this channel is stored in Carbon12_nt_5_10B.dat. The Q value is -23.703 MeV.

$^{12}\text{C}(n,t_6)^{10}\text{B}$ and $^{12}\text{C}(n,t_7)^{10}\text{B}$ and $^{12}\text{C}(n,t_8)^{10}\text{B}$:

Since the (n,t₆), (n,t₇), and (n,t₈) channels have very similar excitation energies, indistinguishable in the current study, they are treated identically in this simulation. This reaction channel in MENATE_R refers to production of a triton and the population of ^{10}B in the sixth excited state ($J^\pi = 2^-$, $E_x = 5.110$ MeV), seventh excited state ($J^\pi = 2^+$, $E_x = 5.163$ MeV), or eighth excited state ($J^\pi = 1^+$, $E_x = 5.182$ MeV). The data for this peak in the present work have not yet been analyzed. A placeholder cross section for this reaction was obtained from the average of the (n,d₀) and the (n,p₁) reaction. This considerably overestimates the cross section for this channel. The

placeholder cross sections for these channels are stored in Carbon12_nt_6_10B.dat. The Q value is that of the (n,t_6) state, -24.039 MeV.

Comparison between old and new versions of MENATE_R

To demonstrate the impact of adding these new channels to MENATE_R and modifying existing channels, simulations using the two versions are compared in Fig. 4.15. The simulations were otherwise identical, with the same energy resolution (3.15%), time resolution (1 ns), number of incident neutrons, and a flat energy distribution from 12.47 MeV to 55 MeV. Another valuable observable to consider is the total n-C cross section used by the simulation. Fig. 4.16 compares the total cross section in the old version of MENATE_R with that of the new version of MENATE_R. To calculate the total cross section, we took a linear interpolation of every individual reaction cross section and summed it at integer values of incident neutron energy. The total cross sections in the simulation are compared with the total n-C cross section in the ENDF [65]. At present, the old version of MENATE_R is a better match for ENDF, so it is still preferable to use the old version of MENATE_R instead of the new for anything where the total n-C cross section is important. As more of the cross sections are determined in the current work and implemented in the new version, the total n-C cross section will decrease, since the placeholder reactions added to the new version all overpredict the cross section. This is expected to bring the total n-C cross section in the new version closer to the ENDF than the old version when every new channel is updated. If every cross section in MENATE_R is updated and there remains a significant gap between the total cross section in MENATE_R and that in ENDF, then perhaps a global scaling of the cross sections in MENATE_R may be in order.

Comparison between MENATE_R and data

Perhaps the most important metric for the success of a simulation package is its ability to accurately reproduce experimental data. Shown in Fig. 4.17 is a comparison between simulated diamond spectra and the experimental reconstructed Q value spectra from the diamond for 19 ± 0.5 MeV neutrons. The simulation, using the new version of MENATE_R, is the red histogram, while the experimental data is in blue. The simulated histogram was scaled to match the four rightmost peaks, and the $^{12}\text{C}(n,n'+3\alpha)$ continuum. Note that good agreement is shown between the counts in each peak for the four rightmost peaks, showing that the relative cross sections for those four channels in the simulation agree with experiment. The agreement between simulation and data for the (n,p_1) channel is not perfect, though the background does not agree as well around the (n,p_1) and (n,d_0) peaks, which would help bring simulation and data into better agreement. Additionally, of the channels studied in this work, the uncertainty was highest for (n,p_1) . Since the cross sections have not been determined for the three peaks on the left - (n,p_2) , (n,p_3+p_4) , and (n,d_1) - yet, agreement is not expected between the simulation and data. Rather, the agreement in peak location (reconstructed Q value) is the main takeaway from those peaks for now.

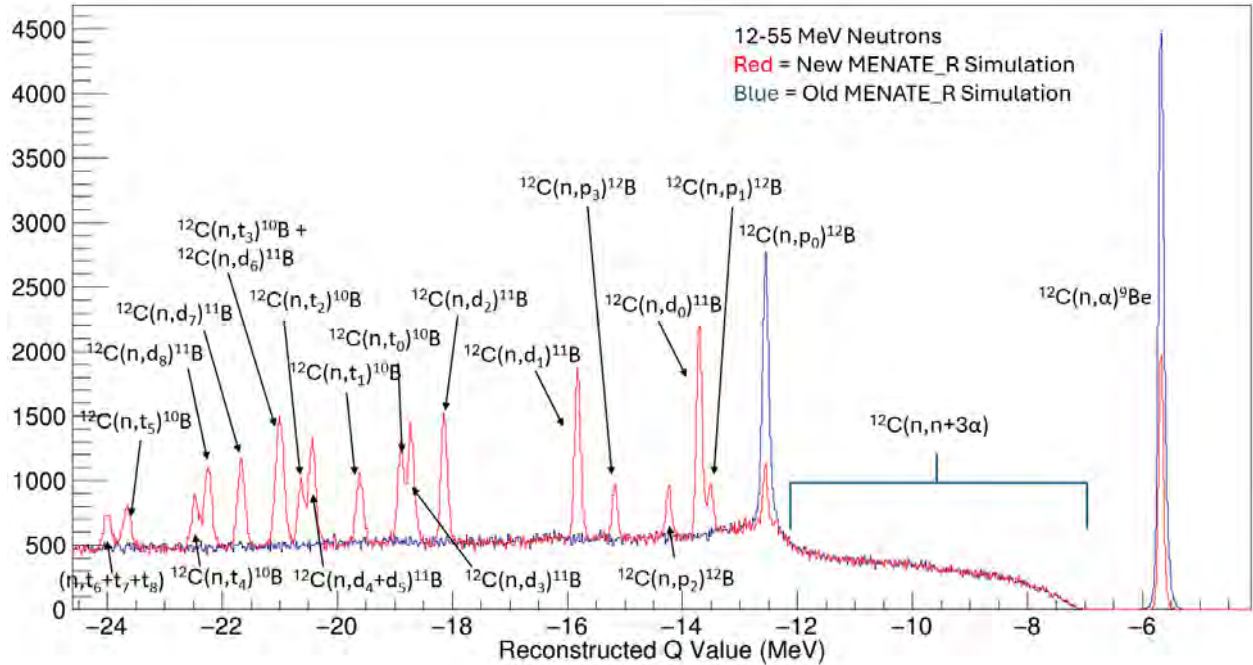


Figure 4.15: Simulated reconstructed Q value spectrum for a diamond detector, comparing the old version of MENATE_R and the new version. Many more reaction channels are included in the new version. The continuum channels have not changed, so the background shows excellent agreement between the old and new version. The two simulations were normalized such that the same number of neutrons were incident on the detector. See the previous section for more detail about each of the reactions included in the new version of MENATE_R.

The shape of the continuum channels in simulation differs somewhat from data. In particular, note the difference in shape between simulation and data for $(n,n'+3\alpha)$ between -9 and -7 MeV reconstructed Q value. This would presumably be due to the simulation predicting the neutron to inherit more of the kinetic energy compared to what occurs in reality. At more negative reconstructed Q values, say below -13.5 MeV, the background is not as well modeled, perhaps due to issues with cross section data for some of the continuum channels in MENATE_R. These were not addressed in this work, but may be addressed in future improvements to MENATE_R.

A second comparison between simulated diamond Q value spectra and data, this time for 27-30 MeV neutrons, is shown in Fig. 4.18. The simulation (red) was scaled to match data (blue) as well as possible for (n,d_0) and $(n,n'+3\alpha)$. The issues with calibration at more negative reconstructed Q values is apparent, since the location of the peaks observed in data does not match the literature peak locations used in simulation. For clarity, the peaks in MENATE_R are labeled, while the peaks in data are not, for the most part. One notable exception is the $^{12}\text{C}(n,^3\text{He}_0)^{10}\text{Be}$, which is observed in the data, but has not yet been added to MENATE_R. Once again, since measured cross sections have not yet been implemented in MENATE_R for peaks to the left of (n,d_0) , agreement between simulation and data is not expected. Note that the (n,p) channels are barely visible in data in this

energy range, so that the small peaks produced with MENATE_R still overpredict the contribution of those reactions. This is at least partly due to MENATE_R using the cross section value at the highest measured energy in the cross section file for any energies exceeding the file's range. When measured cross sections are implemented for (n,p2) and (n,p3+p4), this discrepancy should be reduced. The figure clearly shows that all the peaks beyond (n,d0) have cross sections that are too large. Additionally, not every peak that is simulated corresponds to one in data, so that some channels in MENATE_R may need to be removed to achieve the best agreement with data. The broadening of peaks, particularly the (n, α), at higher incident neutron energies, is observed in data but is not reproduced in simulation.

General comments about this version of MENATE_R:

This version of MENATE_R is far from complete. Until such time as real cross sections are implemented for all of the new reaction channels in MENATE_R, the old version of MENATE_R agrees better with experimental data for at least for the n-C total cross section. The new cross sections that have been added (“real cross sections”), having been obtained from data, agree well with data. The reaction channels that were added with just placeholder cross sections are all too large, and the simulated peaks in the reconstructed Q value plot are much larger than data. Thus, for most organic scintillator detector response applications, the old version of MENATE_R is preferable to the new version. This version must be modified before it is adequate for rigorous applications.

A note of caution: while it may seem tempting to increase the cross sections artificially, to make simulations run faster or simulate more neutron interactions, great care should be taken. First, to keep the relative contributions from every reaction channel the same, every cross section file must be adjusted with the same factor. That is, if one cross section is multiplied by 10, all the other cross sections must be multiplied by 10 to keep the relative contributions of the different processes the same. More troubling is that when certain reaction channels are simulated with much larger cross sections (1000x larger, for instance), spurious peaks arise in a reconstructed Q value spectrum that are not observed experimentally, nor do they appear when a simulation with the typical cross sections is performed. These misbehaving channels include $^{12}\text{C}(n,n)^{12}\text{C}$, $^{12}\text{C}(n,n'+\gamma)^{12}\text{C}$, and $^{12}\text{C}(n,n'+3\alpha)$, which all have neutrons in the exit channel. The issues may arise from a second neutron interaction within the detector, made possible because of the greatly increased cross section, which otherwise would very seldom occur. No major issues like these were observed when using much larger cross sections for the channels that only produced charged particles. Especially for channels with a small cross section, increasing the cross section to obtain the charged particle detection efficiency may be beneficial and can decrease statistical fluctuations in the results of the simulation, provided the cross section is not increased so high that the average interaction point is substantially different than the middle of the detector. A good rule of thumb for this is that a simulation to determine the charged particle detection efficiency should still be valid as long as a significant fraction, perhaps 50% or so, of the neutrons pass through without interacting.

One should avoid “saturating” the cross section, so that every neutron interacts with the detector when calculating efficiency. Greater care should be taken when considering the overall detector response and absolute efficiency, and significant changes to the cross sections are not recommended for most uses of the code.

4.3.3 Potential Future Updates with MENATE_R

The primary planned future update for MENATE_R is the determination of cross sections for new channels (n,p_2) , (n,p_3+p_4) , (n,d_1) , (n,d_2) , etc. The analysis is already underway for these channels. More channels may be added past the eighth excited states of the (n,d) and (n,t) reactions, and some existing channels may be removed if the peaks are not observed above background when the identification and calibration is complete. The $^{12}\text{C}(n,^3\text{He})^{10}\text{Be}$ reaction channel has also been observed in the data, and this could be added to MENATE_R, along with any excited states that are observed. Additionally, new classes of reaction channels could be added, including those corresponding to population of α -unbound states of ^{10}B and ^{11}B . This would change these reactions from $^{12}\text{C}(n,d)^{11}\text{B}$ and $^{12}\text{C}(n,t)^{10}\text{B}$ to $^{12}\text{C}(n,d+\alpha)^7\text{Li}$ and $^{12}\text{C}(n,t+\alpha)^6\text{Li}$, respectively. At even higher excitation energy, the neutron unbound states of ^{11}B and ^{10}B could be modeled as well, in the form of $^{12}\text{C}(n,n'+d)^{10}\text{B}$ and $^{12}\text{C}(n,n'+t)^9\text{B}$, in much the same way that the $^{12}\text{C}(n,n'+p)^{11}\text{B}$ reaction accounts for the neutron unbound states of ^{12}B .

Further work with MENATE_R could entail updating angular distributions for reaction channels for which they have been measured, including $^{12}\text{C}(n,\alpha)^9\text{Be}$, $^{12}\text{C}(n,n'+3\alpha)$, and $^{12}\text{C}(n,n'+\gamma)^{12}\text{C}$. Also, updating the code so that it uses fully relativistic kinematics would improve its modeling ability, particularly at higher energies.

As mentioned previously, the gamma decay of excited states of ^{12}B , ^{11}B , and ^{10}B is not included in the simulation. These decays could be included, which is particularly important when simulating experiments with a long data collection time or with low thresholds so that these relatively low energy signals are recorded. Finally, the beta decay of unstable nuclei in the ground state could be simulated, which is important under the same conditions as the gamma decays.

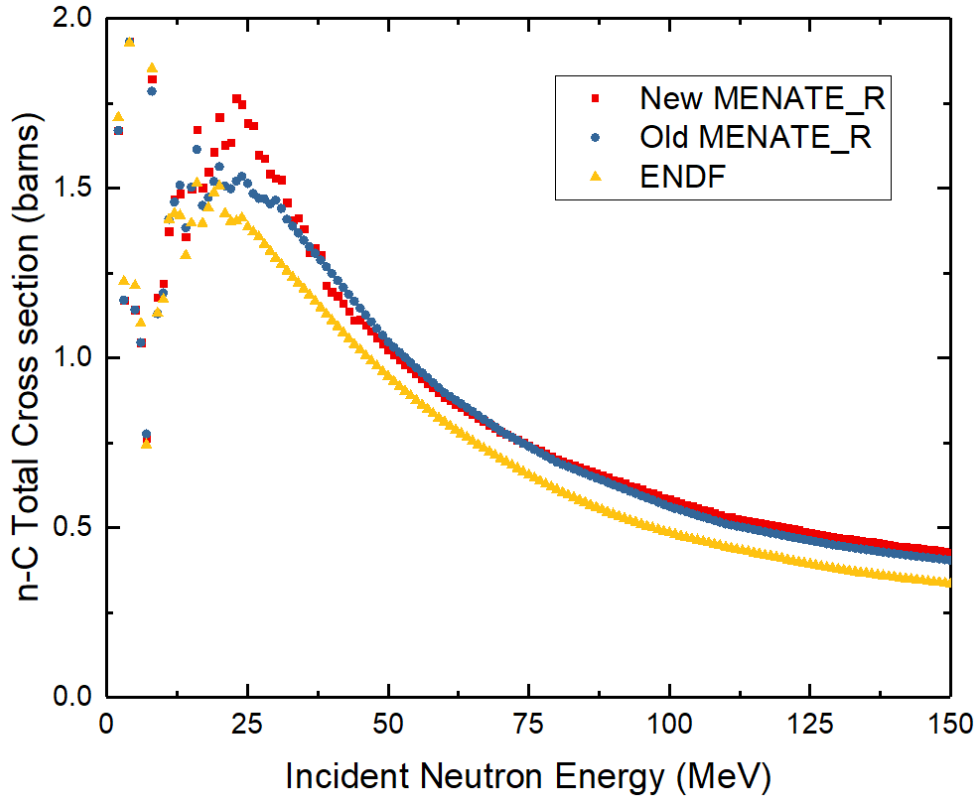


Figure 4.16: Comparison of the n-C total cross section in the old and new versions of MENATE_R with ENDF. For both versions of MENATE_R, a linear interpolation of every included n-C reaction cross section was summed to calculate the total n-C cross section. On the whole, the old version of MENATE_R agrees better. When measured cross sections are implemented for every new reaction channel added, the total cross section for the new version of MENATE_R will decrease significantly for $15 \leq E_n \leq 50$ MeV. Thus, the simulation will benefit from more accurate cross section information in addition to much more accurate kinematic information for the included channels. The deviation between MENATE_R and ENDF at the lowest energies is due to discrepancies in the carbon elastic cross sections, and the $(n,n'+\gamma)$ cross section above 4.4 MeV. This indicates that updating the (n,n) and $(n,n'+\gamma)$ cross sections are needed improvements to MENATE_R.

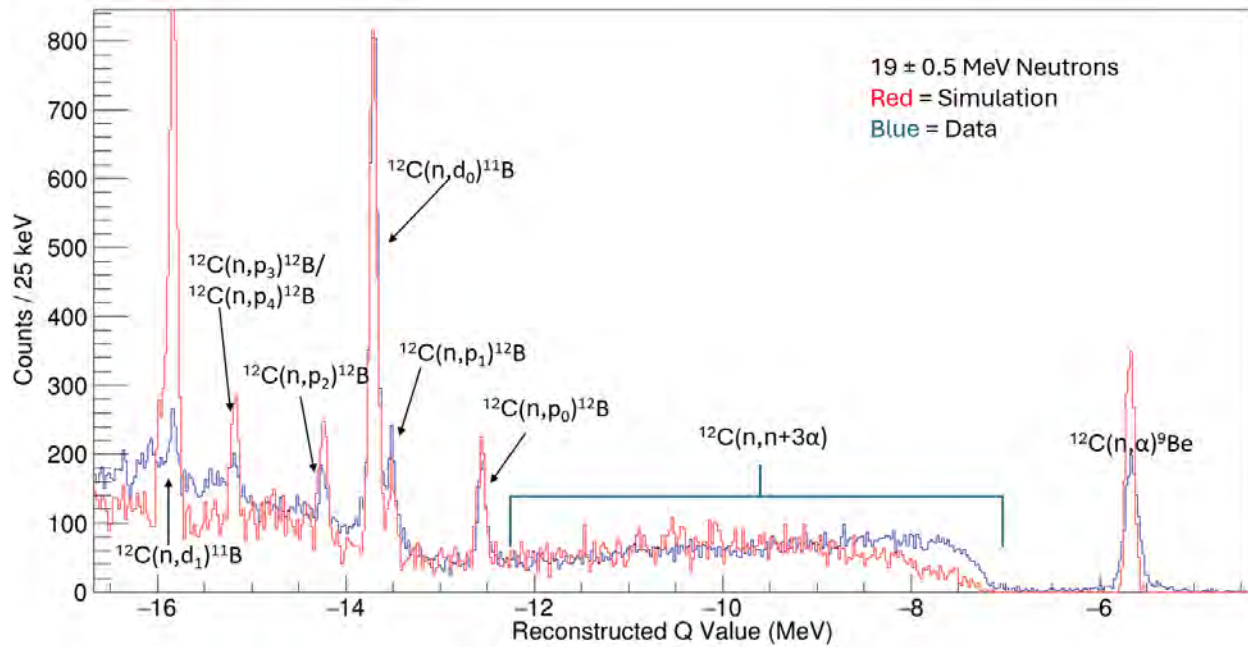


Figure 4.17: Reconstructed Q value spectrum for 19 MeV neutrons, comparing experimental data (blue) with the new MENATE_R simulation (red) for a diamond detector. Note the good agreement between simulation and experiment for the four peaks on the right, which have the new cross sections implemented, compared to the three peaks on the left, which do not yet have measured cross sections implemented. The simulation was scaled to achieve good agreement with data, instead of any more complex normalization procedure.

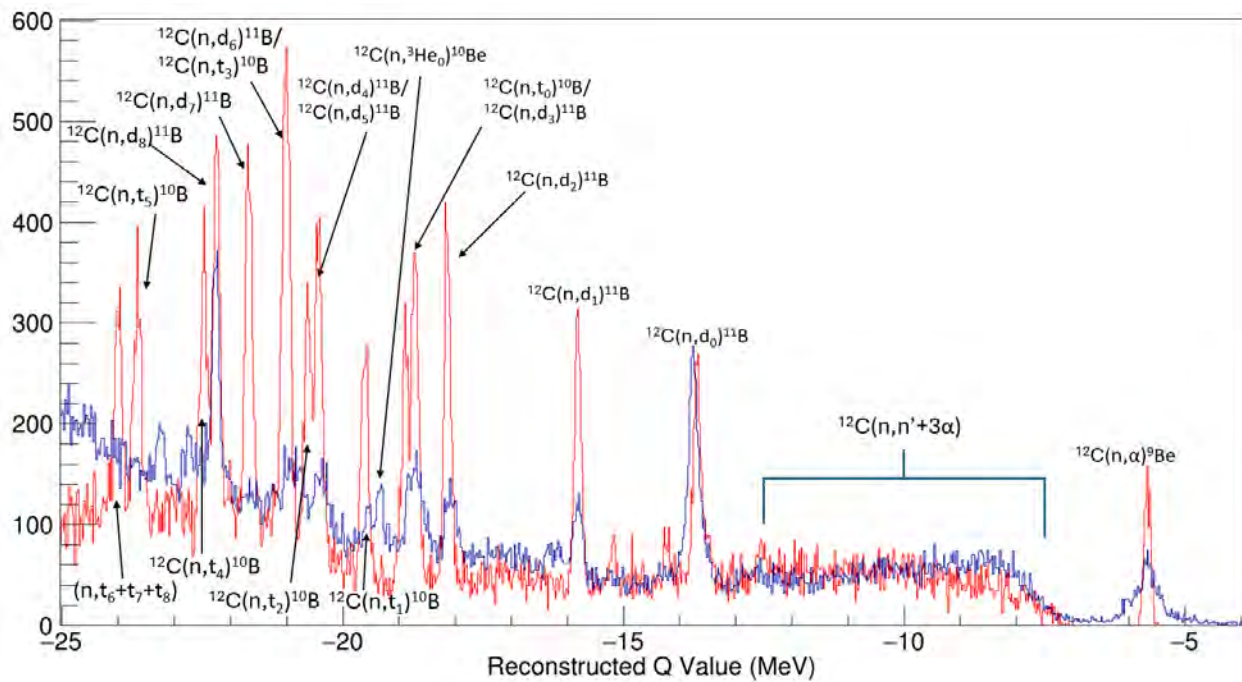


Figure 4.18: Reconstructed Q value spectrum for 27-30 MeV neutrons, comparing experimental data (blue) with the new MENATE_R simulation (red) for a diamond detector. The simulation was scaled to achieve good agreement for the (n, d_0) peak.

Chapter 5

SUMMARY AND CONCLUSIONS

Cross section measurements were performed for four channels: $^{12}\text{C}(\text{n}, \alpha)^9\text{Be}$, $^{12}\text{C}(\text{n}, \text{p}_0)^{12}\text{B}$, $^{12}\text{C}(\text{n}, \text{p}_1)^{12}\text{B}$, and $^{12}\text{C}(\text{n}, \text{d}_0)^{11}\text{B}$. These measurements extend the energy ranges over which the cross sections have been measured up to 55 MeV for $^{12}\text{C}(\text{n}, \alpha)^9\text{Be}$, up to 46 MeV for $^{12}\text{C}(\text{n}, \text{d}_0)^{11}\text{B}$, and up to 27 MeV for $^{12}\text{C}(\text{n}, \text{p}_0)^{12}\text{B}$ and $^{12}\text{C}(\text{n}, \text{p}_1)^{12}\text{B}$, while also providing higher granularity data than previous studies. These measurements can be used to improve simulation of neutron interactions with carbon, which is particularly beneficial for neutron detection with organic scintillators. These measurements can also improve our understanding of the ^{13}C compound nucleus. From the R-matrix fits performed, preliminary spectroscopic conclusions can be drawn regarding seven states – 16.152 MeV, 19.9 MeV, 21.05 MeV, 21.28 MeV, 22.2 MeV, 24 MeV, and 26 MeV – primarily providing clarity of uncertain spin-parity assignments. Further conclusions about these and other states should be possible when a full multichannel R-matrix fit is performed on the data presented in this thesis and other reaction channels.

5.1 Implications

These new cross section measurements help illustrate that the ENDF evaluations for these channels need significant improvement. The $^{12}\text{C}(\text{n}, \alpha)^9\text{Be}$ cross section evaluation (MT107) [65] should be updated with new data obtained with diamond detectors, and the energy range should be extended beyond 20 MeV. The data presented in this work would be crucial for this data extension and provide further evidence for the need for improvements below 20 MeV.

The evaluation for $^{12}\text{C}(\text{n}, \text{p})$ (MT103) [65] can be expanded by adding evaluations for exclusive cross sections: $^{12}\text{C}(\text{n}, \text{p}_0)^{12}\text{B}$, $^{12}\text{C}(\text{n}, \text{p}_1)^{12}\text{B}$, $^{12}\text{C}(\text{n}, \text{p}_2)^{12}\text{B}$, $^{12}\text{C}(\text{n}, \text{p}_3)^{12}\text{B}$, and $^{12}\text{C}(\text{n}, \text{p}_4)^{12}\text{B}$. The data presented in this work will be very beneficial for (n,p₀) and (n,p₁) and extending the evaluated cross section measurements to higher incident neutron energies. As more of the reaction channels in this work are analyzed, further input can be provided for the evaluations for (n,p₂), (n,p₃), and (n,p₄). Currently, the only data set that has published cross sections for (n,p₂), (n,p₃), and (n,p₄) is Pillon *et al.* (2017) [13], making a very precise measurement but over a limited incident energy range (18.9 to 20.7 MeV). Admittedly, the (n,p₃) and (n,p₄) channels are not distinguishable in

the current dataset, and Pillon *et al.* had to analyze the pulse height spectrum with software that, given the energy resolution of the detector and the expected peak branching, can deconvolve a combined peak and give a good estimate of the ratio of counts in the deconvolved peaks. Thus, the results for these channels are not as confident as the rest of his study. However, perhaps a combined evaluation could be made for the two peaks if it is not best to perform a separate evaluation.

Similarly, the inclusive $^{12}\text{C}(n,d)$ cross section (MT104) should be expanded with exclusive cross sections based on the excited states of the residual nucleus. Again, the works of Pillon *et al.* [12, 13] are beneficial, publishing cross sections for $^{12}\text{C}(n,d_0)^{11}\text{B}$ and $^{12}\text{C}(n,d_1)^{11}\text{B}$ over a small incident energy range. The present work extends the (n,d_0) cross section measurements significantly, and exclusive cross sections for (n,d_1) and (n,d_2) should be possible from this data set. Further analysis of (n,d_3) , (n,d_4) , (n,d_5) and higher excited states may be possible if a method similar to what Pillon used for (n,p_3) and (n,p_4) is used.

These improvements would be beneficial for detector and simulation benchmarking.

Bibliography

- [1] Nuclear Science Advisory Committee. A new era of discovery: The 2023 long range plan for nuclear science, 2023. NSAC was charged by the Department of Energy Office of Science and National Science Foundation to produce the long range plan.
- [2] National Nuclear Data Center. *Chart of the Nuclides*. Information extracted from the NuDat database, <https://www.nndc.bnl.gov/nudat/>.
- [3] A. Revel, O. Sorlin, F. M. Marqués, Y. Kondo, J. Kahlbow, T. Nakamura, N. A. Orr, F. Nowacki, J. A. Tostevin, C. X. Yuan, N. L. Achouri, H. Al Falou, L. Atar, T. Aumann, H. Baba, K. Boretzky, C. Caesar, D. Calvet, H. Chae, N. Chiga, A. Corsi, H. L. Crawford, F. Delaunay, A. Delbart, Q. Deshayes, Z. Dombrádi, C. A. Douma, Z. Elekes, P. Fallon, I. Gašparić, J.-M. Gheller, J. Gibelin, A. Gillibert, M. N. Harakeh, W. He, A. Hirayama, C. R. Hoffman, M. Holl, A. Horvat, Á. Horváth, J. W. Hwang, T. Isobe, N. Kalantar-Nayestanaki, S. Kawase, S. Kim, K. Kisamori, T. Kobayashi, D. Körper, S. Koyama, I. Kuti, V. Lapoux, S. Lindberg, S. Masuoka, J. Mayer, K. Miki, T. Murakami, M. Najafi, K. Nakano, N. Nakatsuka, T. Nilsson, A. Obertelli, F. de Oliveira Santos, H. Otsu, T. Ozaki, V. Panin, S. Paschalis, D. Rossi, A. T. Saito, T. Saito, M. Sasano, H. Sato, Y. Satou, H. Scheit, F. Schindler, P. Schrock, M. Shikata, Y. Shimizu, H. Simon, D. Sohler, L. Stuhl, S. Takeuchi, M. Tanaka, M. Thoennessen, H. Törnqvist, Y. Togano, T. Tomai, J. Tscheuschner, J. Tsubota, T. Uesaka, Z. Yang, M. Yasuda, and K. Yoneda. Extending the southern shore of the island of inversion to ^{28}F . *Phys. Rev. Lett.*, 124:152502, Apr 2020.
- [4] P. Doornenbal, H. Scheit, S. Takeuchi, Y. Utsuno, N. Aoi, K. Li, M. Matsushita, D. Stepenbeck, H. Wang, H. Baba, E. Ideguchi, N. Kobayashi, Y. Kondo, J. Lee, S. Michimasa, T. Motobayashi, T. Otsuka, H. Sakurai, M. Takechi, Y. Togano, and K. Yoneda. Low- z shore of the “island of inversion” and the reduced neutron magicity toward ^{28}O . *Phys. Rev. C*, 95:041301, Apr 2017.
- [5] M. Meister, L. V. Chulkov, H. Simon, T. Aumann, M. J. G. Borge, Th. W. Elze, H. Em-ling, H. Geissel, M. Hellström, B. Jonson, J. V. Kratz, R. Kulesa, Y. Leifels, K. Markenroth, G. Münzenberg, F. Nickel, T. Nilsson, G. Nyman, V. Pribora, A. Richter, K. Riisager, C. Scheidenberger, G. Schrieder, O. Tengblad, and M. V. Zhukov. The $t+n+n$ system and ^5H . *Phys. Rev. Lett.*, 91:162504, Oct 2003.

- [6] A. Spyrou, Z. Kohley, T. Baumann, D. Bazin, B. A. Brown, G. Christian, P. A. DeYoung, J. E. Finck, N. Frank, E. Lunderberg, S. Mosby, W. A. Peters, A. Schiller, J. K. Smith, J. Snyder, M. J. Strongman, M. Thoennessen, and A. Volya. First observation of ground state dineutron decay: ^{16}Be . *Phys. Rev. Lett.*, 108:102501, Mar 2012.
- [7] Z. Kohley, E. Lunderberg, P. A. DeYoung, A. Volya, T. Baumann, D. Bazin, G. Christian, N. L. Cooper, N. Frank, A. Gade, C. Hall, J. Hinnefeld, B. Luther, S. Mosby, W. A. Peters, J. K. Smith, J. Snyder, A. Spyrou, and M. Thoennessen. First observation of the ^{13}Li ground state. *Phys. Rev. C*, 87:011304, Jan 2013.
- [8] B Luther, T Baumann, M Thoennessen, J Brown, P DeYoung, J Finck, J Hinnefeld, R Howes, K Kemper, P Pancella, G Peaslee, W Rogers, and S Tabor. Mona—the modular neutron array. *Nuclear Instruments and Methods in Physics Research Section A: Accelerators, Spectrometers, Detectors and Associated Equipment*, 505(1):33–35, 2003. Proceedings of the tenth Symposium on Radiation Measurements and Applications.
- [9] T. Nakamura and Y. Kondo. Large acceptance spectrometers for invariant mass spectroscopy of exotic nuclei and future developments. *Nuclear Instruments and Methods in Physics Research Section B: Beam Interactions with Materials and Atoms*, 376:156–161, 2016. Proceedings of the XVIIth International Conference on Electromagnetic Isotope Separators and Related Topics (EMIS2015), Grand Rapids, MI, U.S.A., 11-15 May 2015.
- [10] K. Boretzky, I. Gaaparić, M. Heil, J. Mayer, A. Heinz, C. Caesar, D. Kresan, H. Simon, H.T. Tornqvist, D. Korper, G. Alkhazov, L. Atar, T. Aumann, D. Bemmerer, S.V. Bondarev, L.T. Bott, S. Chakraborty, M.I. Cherciu, L.V. Chulkov, M. Ciobanu, U. Datta, E. De Filippo, C.A. Douma, J. Dreyer, Z. Elekes, J. Enders, D. Galaviz, E. Geraci, B. Gnoffo, K. Gobel, V.L. Golovtsov, D. Gonzalez Diaz, N. Gruzinsky, T. Heftrich, H. Heggen, J. Hehner, T. Hensel, E. Hoemann, M. Holl, A. Horvat, Á. Horvath, G. Ickert, D. Jelavic Malenica, H.T. Johansson, B. Jonson, J. Kahlbow, N. Kalantar-Nayestanaki, A. Kelic-Heil, M. Kempe, K. Koch, N.G. Kozlenko, A.G. Krivshich, N. Kurz, V. Kuznetsov, C. Langer, Y. Leifels, I. Lihtar, B. Loher, J. Machado, N.S. Martorana, K. Miki, T. Nilsson, E.M. Orischin, E.V. Pagano, S. Pirrone, G. Politi, P.-M. Potlog, A. Rahaman, R. Reifarth, C. Rigollet, M. Roder, D.M. Rossi, P. Rusotto, D. Savran, H. Scheit, F. Schindler, D. Stach, E. Stan, J. Stomvall Gill, P. Teubig, M. Trimarchi, L. Uvarov, M. Volknaendt, S. Volkov, A. Wagner, V. Wagner, S. Wranne, D. Yakorev, L. Zanetti, A. Zilges, and K. Zuber. Neuland: The high-resolution neutron time-of-flight spectrometer for r3b at fair. *Nuclear Instruments and Methods in Physics Research Section A: Accelerators, Spectrometers, Detectors and Associated Equipment*, 1014:165701, 2021.
- [11] T Baumann, A Spyrou, and M Thoennessen. Nuclear structure experiments along the neutron drip line. *Reports on Progress in Physics*, 75(3):036301, feb 2012.

- [12] M. Pillon, M. Angelone, A. Krása, A. J. M. Plompen, P. Schillebeeckx, and M. L. Sergi. Measurement of Neutron Reaction Cross Sections in Carbon using a Single Crystal Diamond Detector. *AIP Conference Proceedings*, 1412(1):121–128, 12 2011.
- [13] Pillon, M., Angelone, M., Belloni, F., Geerts, W., Loreti, S., Milocco, A., and Plompen, A.J.M. High-resolution measurements of the excited states (n,pn), (n,dn) c-12 cross sections. *EPJ Web Conf.*, 146:11005, 2017.
- [14] M. Majerle, M. Angelone, A. Krása, J. Novák, M. Pillon, R. Pilotti, A. Plompen, E. Šimečková, and M. Štefánik. The response of single crystal diamond detectors to 17–34 mev neutrons. *Nuclear Instruments and Methods in Physics Research Section A: Accelerators, Spectrometers, Detectors and Associated Equipment*, 951:163014, 2020.
- [15] S. A. Kuvín, H. Y. Lee, B. DiGiovine, A. Georgiadou, S. Mosby, D. Votaw, M. White, and L. Zavorka. Validation of neutron-induced reactions on natural carbon using an active target at neutron energies up to 22 MeV at lansce. *Phys. Rev. C*, 104:014603, Jul 2021.
- [16] R. C. Haight, S. M. Grimes, R. G. Johnson and H. H. Barschall. The $^{12}\text{C}(n,\alpha)$ reaction and the kerma factor for carbon at $E_n = 14.1$ mev. *Nuclear Science and Engineering*, 87(1):41–47, 1984.
- [17] D. Schmidt, R. Böttger, H. Klein and R. Nolte. Investigation of the $^9\text{Be}(a,n)^{12}\text{C}$ reaction. pt. 2. differential cross sections for $E_a=7.02\text{-}15.70$ MeV and $E_{ex}(^{12}\text{C})=0.0, 4.439, 7.654, 9.641, 10.84, 11.83$ and 12.71 MeV. *Phys. Techn. Bundesanst, Neutronenphysik Reports*, Apr 1992.
- [18] Toshiya Sanami, Mamoru Baba, Keiichiro Saito, and Naohiro Hirakawa. (n,α) cross-section measurement using a gaseous sample and a gridded ionization chamber. *Nuclear Instruments and Methods in Physics Research Section A: Accelerators, Spectrometers, Detectors and Associated Equipment*, 440(2):403–408, 2000.
- [19] K. Kondo, I. Murate, K. Ochiai, N. Kubota, H. Miyamaru, C. Konno, and T. Nishitani. Measurement and analysis of neutron-induced alpha particle emission double-differential cross section of carbon at 14.2 mev. *Journal of Nuclear Science and Technology*, 45(2):103–115, 2008.
- [20] Z. Kohley, E. Lunderberg, P.A. DeYoung, B.T. Roeder, T. Baumann, G. Christian, S. Mosby, J.K. Smith, J. Snyder, A. Spyrou, and M. Thoennessen. Modeling interactions of intermediate-energy neutrons in a plastic scintillator array with geant4. *Nuclear Instruments and Methods in Physics Research Section A: Accelerators, Spectrometers, Detectors and Associated Equipment*, 682:59–65, 2012.
- [21] B. Roeder. Development and validation of neutron detection simulations for eurisol. *EURISOL Design Study*, pages 31–44, 2008.

- [22] S. Agostinelli, J. Allison, K. Amako, J. Apostolakis, H. Araujo, P. Arce, M. Asai, D. Axen, S. Banerjee, G. Barrand, F. Behner, L. Bellagamba, J. Boudreau, L. Broglia, A. Brunengo, H. Burkhardt, S. Chauvie, J. Chuma, R. Chytracsek, G. Cooperman, G. Cosmo, P. Degtyarenko, A. Dell'Acqua, G. Depaola, D. Dietrich, R. Enami, A. Feliciello, C. Ferguson, H. Fesefeldt, G. Folger, F. Foppiano, A. Forti, S. Garelli, S. Giani, R. Giannitrapani, D. Gibin, J.J. Gómez Cadenas, I. González, G. Gracia Abril, G. Greeniaus, W. Greiner, V. Grichine, A. Grossheim, S. Guatelli, P. Gumplinger, R. Hamatsu, K. Hashimoto, H. Hasui, A. Heikkinen, A. Howard, V. Ivanchenko, A. Johnson, F.W. Jones, J. Kallenbach, N. Kanaya, M. Kawabata, Y. Kawabata, M. Kawaguti, S. Kelner, P. Kent, A. Kimura, T. Kodama, R. Kokoulin, M. Kossov, H. Kurashige, E. Lamanna, T. Lampén, V. Lara, V. Lefebure, F. Lei, M. Liendl, W. Lockman, F. Longo, S. Magni, M. Maire, E. Medernach, K. Minamimoto, P. Mora de Freitas, Y. Morita, K. Murakami, M. Nagamatu, R. Nartallo, P. Nieminen, T. Nishimura, K. Ohtsubo, M. Okamura, S. O'Neale, Y. Oohata, K. Paech, J. Perl, A. Pfeiffer, M.G. Pia, F. Ranjard, A. Rybin, S. Sadilov, E. Di Salvo, G. Santin, T. Sasaki, N. Savvas, Y. Sawada, S. Scherer, S. Sei, V. Sirotenko, D. Smith, N. Starkov, H. Stoecker, J. Sulkimo, M. Takahata, S. Tanaka, E. Tcherniaev, E. Safai Tehrani, M. Tropeano, P. Truscott, H. Uno, L. Urban, P. Urban, M. Verderi, A. Walkden, W. Wander, H. Weber, J.P. Wellisch, T. Wenaus, D.C. Williams, D. Wright, T. Yamada, H. Yoshida, and D. Zschiesche. Geant4—a simulation toolkit. *Nuclear Instruments and Methods in Physics Research Section A: Accelerators, Spectrometers, Detectors and Associated Equipment*, 506(3):250–303, 2003.
- [23] J. Allison, K. Amako, J. Apostolakis, P. Arce, M. Asai, T. Aso, E. Bagli, A. Bagulya, S. Banerjee, G. Barrand, B.R. Beck, A.G. Bogdanov, D. Brandt, J.M.C. Brown, H. Burkhardt, Ph. Canal, D. Cano-Ott, S. Chauvie, K. Cho, G.A.P. Cirrone, G. Cooperman, M.A. Cortés-Giraldo, G. Cosmo, G. Cuttone, G. Depaola, L. Desorgher, X. Dong, A. Dotti, V.D. Elvira, G. Folger, Z. Francis, A. Galoyan, L. Garnier, M. Gayer, K.L. Genser, V.M. Grichine, S. Guatelli, P. Guèye, P. Gumplinger, A.S. Howard, I. Hřivnáčová, S. Hwang, S. Incerti, A. Ivanchenko, V.N. Ivanchenko, F.W. Jones, S.Y. Jun, P. Kaitaniemi, N. Karakatsanis, M. Karamitros, M. Kelsey, A. Kimura, T. Koi, H. Kurashige, A. Lechner, S.B. Lee, F. Longo, M. Maire, D. Mancusi, A. Mantero, E. Mendoza, B. Morgan, K. Murakami, T. Nikitina, L. Pandola, P. Paprocki, J. Perl, I. Petrović, M.G. Pia, W. Pokorski, J.M. Quesada, M. Raine, M.A. Reis, A. Ribon, A. Ristić Fira, F. Romano, G. Russo, G. Santin, T. Sasaki, D. Sawkey, J.I. Shin, I.I. Strakovsky, A. Taborda, S. Tanaka, B. Tomé, T. Toshito, H.N. Tran, P.R. Truscott, L. Urban, V. Uzhinsky, J.M. Verbeke, M. Verderi, B.L. Wendt, H. Wenzel, D.H. Wright, D.M. Wright, T. Yamashita, J. Yarba, and H. Yoshida. Recent developments in geant4. *Nuclear Instruments and Methods in Physics Research Section A: Accelerators, Spectrometers, Detectors and Associated Equipment*, 835:186–225, 2016.
- [24] J. Allison, K. Amako, John Apostolakis, H. Araujo, Pedro Arce, Makoto Asai, Guy Bar-

- rand, Riccardo Capra, Stephane Chauvie, Radovan Chytracsek, Pablo Cirrone, G. Cooperman, Gabriele Cosmo, Giacomo Cuttone, Giuseppe Daquino, M. Donszelmann, M. Dressel, G. Folger, Franca Foppiano, and H. Yoshida. Geant4 developments and applications. *IEEE Transactions on Nuclear Science*, 53:270–278, 02 2006.
- [25] Keiichi SHIBATA, Osamu IWAMOTO, Tsuneo NAKAGAWA, Nobuyuki IWAMOTO, Akira ICHIHARA, Satoshi KUNIEDA, Satoshi CHIBA, Kazuyoshi FURUTAKA, Naohiko OTUKA, Takaaki OHSAWA, Toru MURATA, Hiroyuki MATSUNOBU, Atsushi ZUKERAN, So KAMADA, and Jun ichi KATAKURA. Jendl-4.0: A new library for nuclear science and engineering. *Journal of Nuclear Science and Technology*, 48(1):1–30, 2011.
- [26] W.F. Rogers, A.N. Kuchera, J. Boone, N. Frank, S. Mosby, M. Thoennessen, and A. Wantz. Measurements of fast neutron scattering in plastic scintillator with energies from 20 to 200 MeV. *Nuclear Instruments and Methods in Physics Research Section A: Accelerators, Spectrometers, Detectors and Associated Equipment*, 943:162436, 2019.
- [27] M. D. Jones, N. Frank, T. Baumann, J. Brett, J. Bullaro, P. A. DeYoung, J. E. Finck, K. Hammerton, J. Hinnefeld, Z. Kohley, A. N. Kuchera, J. Pereira, A. Rabeh, W. F. Rogers, J. K. Smith, A. Spyrou, S. L. Stephenson, K. Stiefel, M. Tuttle-Timm, R. G. T. Zegers, and M. Thoennessen. Two-neutron sequential decay of ^{24}O . *Phys. Rev. C*, 92:051306, Nov 2015.
- [28] D. A. Kellogg. Cross sections for products of 90-mev neutrons on carbon. *Phys. Rev.*, 90:224–232, Apr 1953.
- [29] V V Bobyr, G I Primenko, K K Rev'yuk, V I Strizhak, Yu I Totiskii, and V T Tustanovskii. Excitation function for the reaction $^{12}\text{C}(n,p)^{12}\text{B}$ at neutron energies of 16 to 18 mev. *Izv. Akad. Nauk SSSR, Ser. Fiz., v. 36, no. 12, pp. 2621-2622*, 12 1972.
- [30] V.E. Ablesimov. The cross-section for the $^{12}\text{C}(n,p)^{12}\text{B}$ reaction near the threshold. *Neutron Physics Conf.*, 1:173, 1971.
- [31] E.M. Rimmer and P.S. Fisher. Resonances in the (n, p) reaction on ^{12}C . *Nuclear Physics A*, 108(3):567–576, 1968.
- [32] William E. Kreger and Bernard D. Kern. $^{12}\text{C}(n,p)^{12}\text{B}$ cross section for 14.9- to 17.5-mev neutrons. *Phys. Rev.*, 113:890–894, Feb 1959.
- [33] A. HUCK, G. WALTER and A. COCHE. Reactions induced on carbon by fast neutrons. *J. Phys. Conferences*, 27:88–89, 1966.
- [34] H. Kitazawa and N. Yamamuro. (n, p) reaction on ^{12}C induced by 14.1 mev neutrons. *Journal of the Physical Society of Japan*, 26(3):600–606, 1969.

- [35] A.P Stevens. *Neutron induced alpha production from carbon between 18 and 22 MeV*. PhD thesis, University of Capetown, 1976.
- [36] E.A. Davis, T.W. Bonner, D.W. Worley, and R. Bass. Disintegration of ^{16}O and ^{12}C by fast neutrons. *Nuclear Physics*, 48:169–175, 1963.
- [37] Stanley Kardonsky, Harmon L. Finston, and Evan T. Williams. $^{40}\text{Ar}(n, \alpha)^{37}\text{S}$ reaction at 14.4 mev. *Phys. Rev. C*, 4:840–846, Sep 1971.
- [38] G.Giorginis, V.Khryachkov, V.Corcalciuc, M.Kievets. The cross section of the $^{12}\text{C}(n, \alpha)^9\text{Be}$ reaction in the 7.5-9.6 mev energy range. *unpublished*, 1991.
- [39] R. A. Al-Kital and R. A. Peck. $^{12}\text{C}(n, \alpha)^9\text{Be}$ reaction induced by 14-mev neutrons. *Phys. Rev.*, 130:1500–1503, May 1963.
- [40] M.L. Chatterjee and B. Sen. The (n, α) reaction on ^{12}C at 14 mev. *Nuclear Physics*, 51:583–587, 1964.
- [41] D. Kopsch and S. Cierjacks. Alpha-proton discrimination with a ^{213}Ne liquid scintillator used for the measurement of the (n, α) -reaction on ^{12}C . *Nuclear Instruments and Methods*, 54(2):277–281, 1967.
- [42] G.Dietze, H.J.Brede, H.Klein and H.Schoelermann. Differential cross sections of the $^{12}\text{C}(n, \alpha)^9\text{Be}$ reaction in the energy range from 8 to 10 mev extracted from the ^{213}Ne scintillator response functions. *conference on nuclear data for Science and technology, Antwerp, 1982*, page 930, 1982.
- [43] B. Antolković, G. Dietze, and H. Klein. Reaction cross sections on carbon for neutron energies from 11.5 to 19 mev. *Nuclear Science and Engineering*, 107(1):1–21, 1991.
- [44] M. Brendle, M. Mörike, G. Staudt, and G. Steidle. The $^{12}\text{C}(n, 0)^9\text{Be}$ reaction at 13.9 and 15.6 mev. *Zeitschrift für Naturforschung A*, 23(8):1229–1230, 1968.
- [45] Jie Liu, Zengqi Cui, Yiwei Hu, Haofan Bai, Zhenpeng Chen, Cong Xia, Tieshuan Fan, Jinxiang Chen, Guohui Zhang, Xichao Ruan, Hanxiong Huang, Jie Ren, and Hongtao Chen. $^{12}\text{C}(n, n+3)$ and $^{12}\text{C}(n, 0)^9\text{Be}$ cross sections in the mev neutron energy region. *Physics Letters B*, 842:137985, 2023.
- [46] Yasushige Yano and Tohru Motobayashi and. Radioactive isotope beam factory at riken (ribf). *Nuclear Physics News*, 17(4):5–10, 2007.
- [47] A. Olivier, T. Cai, S. Akhter, Z. Ahmad Dar, V. Ansari, M. V. Ascencio, M. Sajjad Athar, A. Bashyal, A. Bercellie, M. Betancourt, J. L. Bonilla, A. Bravar, H. Budd, G. Caceres, G. A. Díaz, J. Felix, L. Fields, A. Filkins, R. Fine, A. M. Gago, P. K. Gaur, S. M. Gilligan, R. Gran,

- E. Granados, D. A. Harris, A. L. Hart, D. Jena, S. Jena, J. Kleykamp, A. Klustová, M. Kordosky, D. Last, A. Lozano, X.-G. Lu, S. Manly, W. A. Mann, C. Mauger, K. S. McFarland, B. Messerly, O. Moreno, J. G. Morfín, D. Naples, J. K. Nelson, C. Nguyen, V. Paolone, G. N. Perdue, C. Pernas, K.-J. Plows, M. A. Ramírez, H. Ray, N. Roy, D. Ruterbories, H. Schellman, C. J. Solano Salinas, M. Sultana, V. S. Syrotenko, E. Valencia, N. H. Vaughan, A. V. Waldron, B. Yaeggy, and L. Zazueta. Measurement of the multineutron $\bar{\nu}_\mu$ charged current differential cross section at low available energy on hydrocarbon. *Phys. Rev. D*, 108:112010, Dec 2023.
- [48] Michael Evan Rising, Jerawan Chudoung Armstrong, Simon R. Bolding, Forrest Brooks Brown, Jeffrey S. Bull, Timothy Patrick Burke, Alexander Rich Clark, David A. Dixon, Robert Arthur Forster, III, Jesse Frank Giron, Tristan Sumner Grieve, Henry Grady Hughes, III, Colin James Josey, Joel Aaron Kulesza, Roger Lee Martz, Austin P. McCartney, Gregg Walter McKinney, Scott William Mosher, Eric John Pearson, Clell Jeffrey Solomon, Jr., Sriram Swaminarayan, Jeremy Ed Sweezy, Stephen Christian Wilson, and Anthony J. Zukaitis. MCNP[®] Code Version 6.3.0 Release Notes. Technical Report LA-UR-22-33103, Rev. 1, Los Alamos National Laboratory, Los Alamos, NM, USA, January 2023.
- [49] Jeonghyeok Park, Fanurs Chi-En Teh, ManYee Betty Tsang, Kyle W. Brown, Zbigniew Chajcki, Byungsik Hong, Taras Lokotko, William G. Lynch, Joeseeph M. Wieske, and Kuan Zhu. neuSIM4: A comprehensive GEANT4 based neutron simulation code. *Nuclear Instruments and Methods in Physics Research Section A: Accelerators, Spectrometers, Detectors and Associated Equipment*, 1065:169475, 2024.
- [50] A. Koning, S. Hilaire, S. Goriely. Talys: modeling of nuclear reactions. *The European Physical Journal A*, 59, 2023.
- [51] P Descouvemont and D Baye. The r-matrix theory. *Reports on Progress in Physics*, 73(3):036301, feb 2010.
- [52] Ian J. Thompson and Filomena M. Nunes. *Nuclear Reactions for Astrophysics: Principles, Calculation and Applications of Low-Energy Reactions*. Cambridge University Press, 2009.
- [53] A. M. Lane and R. G. Thomas. R-matrix theory of nuclear reactions. *Rev. Mod. Phys.*, 30:257–353, Apr 1958.
- [54] lansce.lanl.gov/facilities/index.php.
- [55] www.cytivalifesciences.com/en/us.
- [56] www.cividec.at.
- [57] www.caen.it/products/compass/.

- [58] R. Brun and F. Rademakers. ROOT: An object oriented data analysis framework. *Nucl. Instrum. Meth. A*, 389:81–86, 1997. See also ROOT [software], Release v6.22/08, 12/03/2021.
- [59] A.D. Carlson, V.G. Pronyaev, R. Capote, G.M. Hale, Z.-P. Chen, I. Duran, F.-J. Hambesch, S. Kunieda, W. Mannhart, B. Marcinkevicius, R.O. Nelson, D. Neudecker, G. Noguere, M. Paris, S.P. Simakov, P. Schillebeeckx, D.L. Smith, X. Tao, A. Trkov, A. Wallner, and W. Wang. Evaluation of the neutron data standards. *Nuclear Data Sheets*, 148:143–188, 2018. Special Issue on Nuclear Reaction Data.
- [60] C. A. Schneider, W.S. Rasband and K.W. Eliceiri. NIH Image to ImageJ: 25 years of image analysis. *Nature Methods*, 9:671–675, 2012.
- [61] M. R. Bhat. Evaluated nuclear structure data file (ensdf). *Nuclear Data for Science and Technology*, page 817, 1992. Data extracted using the NNDC On-Line Data Service from the ENSDF database, file revised as of 06/2024.
- [62] <https://github.com/janmayer/hdtv>.
- [63] A Matta, P Morfouace, N de Sérévile, F Flavigny, M Labiche, and R Shearman. Nptool: a simulation and analysis framework for low-energy nuclear physics experiments. *Journal of Physics G: Nuclear and Particle Physics*, 43(4):045113, mar 2016.
- [64] T. N. Taddeucci. Mcnp flux simulation. Private communication.
- [65] D.A. Brown, M.B. Chadwick, R. Capote, A.C. Kahler, A. Trkov, M.W. Herman, A.A. Sonzogni, Y. Danon, A.D. Carlson, M. Dunn, D.L. Smith, G.M. Hale, G. Arbanas, R. Arcilla, C.R. Bates, B. Beck, B. Becker, F. Brown, R.J. Casperson and J. Conlin et al. ENDF/B-VIII.0: The 8th Major Release of the Nuclear Reaction Data Library with CIELO-project Cross Sections, New Standards and Thermal Scattering Data. *Nuclear Data Sheets*, 148:1–142, 2018. Special Issue on Nuclear Reaction Data.
- [66] N. Otuka, E. Dupont, V. Semkova, B. Pritychenko, A.I. Blokhin, M. Aikawa, S. Babykina, M. Bossant, G. Chen, S. Dunaeva, R.A. Forrest, T. Fukahori, N. Furutachi, S. Ganesan, Z. Ge, O.O. Gritzay, M. Herman, S. Hlavač, K. Katō, B. Lalremruata, Y.O. Lee, A. Makinaga, K. Matsumoto, M. Mikhaylyukova, G. Pikulina, V.G. Pronyaev, A. Saxena, O. Schwerer, S.P. Simakov, N. Soppera, R. Suzuki, S. Takács, X. Tao, S. Taova, F. Tárkányi, V.V. Varlamov, J. Wang, S.C. Yang, V. Zerkin, and Y. Zhuang. Towards a more complete and accurate experimental nuclear reaction data library (exfor): International collaboration between nuclear reaction data centres (nrdc). *Nuclear Data Sheets*, 120:272–276, 2014.
- [67] R. E. Azuma, E. Uberseder, E. C. Simpson, C. R. Brune, H. Costantini, R. J. de Boer, J. Görres, M. Heil, P. J. LeBlanc, C. Ugalde, and M. Wiescher. Azure: An r -matrix code for nuclear astrophysics. *Phys. Rev. C*, 81:045805, Apr 2010.

- [68] M.W. McNaughton, N.S.P. King, F.P. Brady, and J.L. Ullman. Improved predictions of neutron detection efficiency resulting from new measurements of $^{12}\text{C}(\text{n},\text{p})$ and $^{12}\text{C}(\text{n},\text{d})$ reactions at 56 mev. *Nuclear Instruments and Methods*, 129(1):241–245, 1975.
- [69] J.H. Kelley, C.G. Sheu and J. E. Purcell. Evaluated nuclear structure data file (ensdf). *Nucl. Data Sheets*, 198, 1, 2024. Data extracted using the NNDC On-Line Data Service from the ENSDF database, file revised as of 08/01/2024.
- [70] github.com/Andrew-Wantz/MENATE_R.

Appendices

Appendix A

Cross section data tables

Table A.1: $^{12}\text{C}(n,\alpha_0)^9\text{Be}$ data and uncertainty table. There was no background for this channel, so there is no statistical uncertainty due to the background. Additionally, because this channel had no background, the peaks were integrated instead of fit. Therefore, there are no fit uncertainties. The table contains the incident neutron energy (E_n), counts from $^{12}\text{C}(n,\alpha_0)^9\text{Be}$ (Counts: Peak), the charged particle detection efficiency correction for this channel (Corrections: Efficiency), the simulated neutron transmission correction for the flux distribution (Corrections: Trans.), the cross section for this channel (Cross section: σ (mb)), the statistical uncertainties due to the counts from $^{12}\text{C}(n,\alpha_0)^9\text{Be}$ at each energy (Statistical Uncertainty: σ_{Peak}), the total statistical uncertainties combining all statistical uncertainties (Statistical Uncertainties: $\sigma_{stat.total}$), and the relative flux distribution uncertainty (Systematic Uncertainties: σ_{Flux}). The total uncertainty, which includes both the statistical and systematic uncertainties, is also included, both as a percentage and in terms of millibarns. Uncertainties that are constant for every data point were not included in the table for simplicity, but are included in the total uncertainty. These include: the statistical uncertainty from the (n, α) counts at 14.1 MeV used for normalization (2.96%), and systematic uncertainties which include the charged particle detection efficiency correction uncertainty (4%), the incident neutron energy reconstruction uncertainty (0.49%), and the normalization uncertainty based on the weighted average uncertainty of previous data (4.87%).

E_n (MeV)	Counts Peak	Corrections Efficiency Trans.		Cross- section σ (mb)	Uncertainties				Error bar (mb)
					Statistical		Syst.	Total	
					σ_{Peak}	$\sigma_{stat.total}$	σ_{Flux}	σ_{Total}	
12.53	1627	99.3%	82.3%	93.9	2.48%	3.86%	5%	8.94%	8.4
12.61	1612	99.5%	82.1%	91.1	2.49%	3.87%	5%	8.94%	8.1
12.69	1641	99.2%	82.2%	91.0	2.47%	3.86%	5%	8.94%	8.1
12.78	1506	99.2%	81.8%	87.4	2.58%	3.93%	5%	8.97%	7.8
12.86	1330	99.1%	81.7%	78.2	2.74%	4.04%	5%	9.02%	7.0
12.94	1390	99.1%	81.5%	78.1	2.68%	4.00%	5%	9.00%	7.0

E_n (MeV)	Counts Peak	Corrections Efficiency Trans.		Cross- section σ (mb)	Uncertainties				Error bar (mb)
					Statistical σ_{Peak} $\sigma_{stat.total}$		Syst. σ_{Flux}	Total σ_{Total}	
13.03	1333	99.3%	81.9%	75.3	2.74%	4.04%	5%	9.02%	6.8
13.12	1132	99.3%	81.6%	66.7	2.97%	4.20%	5%	9.09%	6.1
13.20	1002	99.2%	81.6%	57.9	3.16%	4.33%	5%	9.15%	5.3
13.29	1084	99.3%	82.0%	61.2	3.04%	4.24%	5%	9.11%	5.6
13.38	1076	99.2%	82.2%	61.5	3.05%	4.25%	5%	9.11%	5.6
13.47	1068	99.0%	81.7%	60.6	3.06%	4.26%	5%	9.12%	5.5
13.56	1198	99.1%	82.3%	66.6	2.89%	4.14%	5%	9.06%	6.0
13.66	1119	99.1%	82.2%	64.7	2.99%	4.21%	5%	9.09%	5.9
13.75	1075	99.0%	82.1%	62.9	3.05%	4.25%	5%	9.11%	5.7
13.84	1056	99.2%	81.9%	60.7	3.08%	4.27%	5%	9.12%	5.5
13.94	1119	99.2%	83.1%	64.1	2.99%	4.21%	5%	9.09%	5.8
14.03	1088	99.1%	82.5%	61.8	3.03%	4.24%	5%	9.11%	5.6
14.13	1139	98.8%	82.6%	63.6	2.96%	4.19%	5%	9.09%	5.8
14.23	1224	99.0%	82.8%	68.7	2.86%	4.12%	5%	9.05%	6.2
14.33	1230	99.0%	83.0%	69.4	2.85%	4.11%	5%	9.05%	6.3
14.43	1247	99.0%	82.6%	71.6	2.83%	4.10%	5%	9.04%	6.5
14.53	1292	98.8%	82.7%	73.2	2.78%	4.06%	5%	9.03%	6.6
14.63	1370	98.9%	82.5%	76.7	2.70%	4.01%	5%	9.00%	6.9
14.74	1379	98.9%	81.6%	78.6	2.69%	4.00%	5%	9.00%	7.1
14.84	1289	98.7%	81.9%	73.8	2.79%	4.07%	5%	9.03%	6.7
14.95	1228	98.5%	81.6%	71.2	2.85%	4.11%	5%	9.05%	6.4
15.05	1138	98.4%	81.4%	65.3	2.96%	4.19%	5%	9.09%	5.9
15.16	1207	98.5%	80.7%	69.1	2.88%	4.13%	5%	9.06%	6.3
15.27	1153	98.5%	81.5%	66.0	2.95%	4.18%	5%	9.08%	6.0
15.38	1172	98.7%	80.5%	68.0	2.92%	4.16%	5%	9.07%	6.2
15.49	1026	98.7%	80.5%	59.1	3.12%	4.30%	5%	9.14%	5.4
15.60	1018	98.4%	80.6%	58.4	3.13%	4.31%	5%	9.14%	5.3
15.72	948	98.5%	80.7%	54.1	3.25%	4.40%	5%	9.18%	5.0
15.83	890	98.2%	80.6%	50.7	3.35%	4.47%	5%	9.22%	4.7
15.95	893	98.2%	80.1%	50.9	3.35%	4.47%	5%	9.22%	4.7
16.07	851	98.3%	80.3%	48.5	3.43%	4.53%	5%	9.25%	4.5
16.19	901	98.0%	80.4%	51.8	3.33%	4.46%	5%	9.21%	4.8
16.31	960	98.2%	81.1%	54.8	3.23%	4.38%	5%	9.18%	5.0
16.43	918	98.0%	81.5%	51.8	3.3%	4.44%	5%	9.20%	4.8
16.55	931	98.2%	81.5%	51.9	3.28%	4.42%	5%	9.19%	4.8

E_n (MeV)	Counts Peak	Corrections		Cross- section σ (mb)	Uncertainties				Error bar (mb)
		Efficiency	Trans.		Statistical		Syst.	Total	
					σ_{Peak}	$\sigma_{stat.total}$	σ_{Flux}	σ_{Total}	
16.68	917	98.0%	81.7%	50.8	3.3%	4.44%	5%	9.20%	4.7
16.80	898	98.0%	81.6%	49.3	3.34%	4.46%	5%	9.21%	4.5
16.93	1022	97.9%	81.7%	56.1	3.13%	4.31%	5%	9.14%	5.1
17.06	949	98.0%	82.1%	52.4	3.25%	4.40%	5%	9.18%	4.8
17.19	891	98.0%	82.2%	49.7	3.35%	4.47%	5%	9.22%	4.6
17.32	839	97.9%	82.2%	46.2	3.45%	4.55%	5.11%	9.32%	4.3
17.45	812	97.6%	82.5%	43.9	3.51%	4.59%	5.75%	9.70%	4.3
17.59	712	97.7%	81.9%	38.8	3.75%	4.78%	6.42%	10.20%	4.0
17.73	652	97.8%	82.1%	35.7	3.92%	4.91%	6.98%	10.62%	3.8
17.86	616	97.9%	81.8%	33.3	4.03%	5.00%	7.54%	11.04%	3.7
18.00	531	97.8%	81.9%	28.3	4.34%	5.25%	7.59%	11.19%	3.2
18.15	431	97.5%	81.7%	23.3	4.82%	5.66%	7.50%	11.32%	2.6
18.29	384	97.1%	81.4%	21.0	5.1%	5.90%	7.41%	11.39%	2.4
18.43	407	97.7%	81.7%	21.7	4.96%	5.77%	7.27%	11.24%	2.4
18.58	395	97.3%	81.8%	21.0	5.03%	5.84%	7.00%	11.09%	2.3
18.73	406	97.2%	81.7%	21.7	4.96%	5.78%	6.71%	10.88%	2.4
18.88	387	97.0%	81.8%	20.7	5.08%	5.88%	6.39%	10.75%	2.2
19.03	388	96.8%	81.6%	20.9	5.08%	5.88%	6.04%	10.54%	2.2
19.19	407	97.0%	81.1%	22.1	4.96%	5.77%	5.68%	10.28%	2.3
19.34	375	97.1%	81.0%	20.4	5.16%	5.95%	5.43%	10.24%	2.1
19.50	462	96.6%	80.9%	25.1	4.65%	5.52%	5.46%	10.01%	2.5
19.66	518	96.9%	80.6%	28.2	4.39%	5.30%	5.49%	9.91%	2.8
19.82	557	97.1%	81.0%	29.8	4.24%	5.17%	5.46%	9.82%	2.9
19.98	577	96.7%	81.1%	30.5	4.16%	5.11%	5.41%	9.76%	3.0
20.15	575	96.3%	81.2%	30.3	4.17%	5.12%	5.35%	9.74%	3.0
20.32	523	96.5%	81.5%	27.5	4.37%	5.28%	5.47%	9.89%	2.7
20.49	502	96.4%	81.7%	26.3	4.46%	5.36%	5.65%	10.03%	2.6
20.66	433	96.2%	81.9%	22.4	4.81%	5.65%	5.84%	10.29%	2.3
20.83	418	96.3%	82.0%	21.4	4.89%	5.72%	5.60%	10.20%	2.2
21.01	422	95.7%	81.9%	21.7	4.87%	5.70%	5.22%	9.98%	2.2
21.19	460	95.8%	82.2%	23.3	4.66%	5.52%	5.19%	9.87%	2.3
21.37	419	96.2%	82.1%	20.7	4.89%	5.71%	5.55%	10.17%	2.1
21.56	404	96.2%	81.9%	19.6	4.98%	5.79%	5.92%	10.42%	2.0
21.75	411	96.0%	82.6%	19.7	4.93%	5.75%	6.04%	10.47%	2.1
21.95	419	95.8%	82.2%	20.1	4.89%	5.71%	6.10%	10.48%	2.1

E_n (MeV)	Counts Peak	Corrections Efficiency Trans.		Cross- section σ (mb)	Uncertainties				Error bar (mb)
					Statistical		Syst.	Total	
					σ_{Peak}	$\sigma_{stat.total}$	σ_{Flux}	σ_{Total}	
22.15	358	95.6%	82.6%	17.0	5.29%	6.06%	6.12%	10.69%	1.8
22.35	361	95.9%	82.0%	17.2	5.26%	6.04%	6.00%	10.60%	1.8
22.55	347	95.6%	82.0%	16.6	5.37%	6.13%	5.87%	10.58%	1.8
22.75	361	95.7%	82.3%	17.0	5.26%	6.04%	6.09%	10.66%	1.8
22.96	339	95.4%	81.9%	15.9	5.43%	6.19%	6.45%	10.95%	1.7
23.17	340	94.9%	82.2%	15.8	5.42%	6.18%	6.81%	11.16%	1.8
23.39	334	94.9%	82.1%	15.3	5.47%	6.22%	7.44%	11.58%	1.8
23.60	324	94.7%	82.0%	14.6	5.56%	6.30%	8.12%	12.06%	1.8
23.83	324	95.1%	81.9%	14.4	5.56%	6.30%	8.61%	12.40%	1.8
24.05	284	94.5%	82.1%	12.5	5.93%	6.63%	8.95%	12.81%	1.6
24.28	269	94.8%	81.9%	11.7	6.10%	6.78%	9.30%	13.13%	1.5
24.51	271	94.3%	82.0%	11.8	6.07%	6.76%	9.27%	13.10%	1.5
24.74	234	94.4%	82.7%	10.1	6.54%	7.18%	9.20%	13.27%	1.3
24.98	229	94.0%	82.2%	9.9	6.61%	7.24%	9.34%	13.41%	1.3
25.22	215	93.7%	82.7%	9.2	6.82%	7.44%	9.57%	13.67%	1.3
25.46	215	93.8%	82.4%	9.2	6.82%	7.44%	9.78%	13.82%	1.3
25.71	209	94.0%	82.6%	8.8	6.92%	7.53%	9.91%	13.96%	1.2
25.96	207	93.9%	82.6%	8.7	6.95%	7.56%	10.05%	14.07%	1.2
26.21	183	93.3%	82.6%	7.7	7.39%	7.96%	10.17%	14.38%	1.1
26.47	195	93.0%	82.9%	8.2	7.16%	7.75%	10.29%	14.35%	1.2
26.73	189	92.8%	83.2%	7.8	7.27%	7.85%	10.89%	14.84%	1.2
27.00	200	92.5%	83.2%	8.1	7.07%	7.67%	11.98%	15.56%	1.3
27.27	218	92.8%	83.4%	8.7	6.77%	7.39%	12.71%	16.01%	1.4
27.54	186	92.4%	83.4%	7.5	7.33%	7.91%	12.35%	15.97%	1.2
27.82	200	92.5%	83.3%	8.1	7.07%	7.67%	11.97%	15.56%	1.3
28.11	179	92.6%	83.3%	7.2	7.47%	8.04%	12.58%	16.21%	1.2
28.39	160	91.8%	83.3%	6.3	7.91%	8.44%	13.58%	17.20%	1.1
28.69	157	91.4%	83.8%	6.1	7.98%	8.51%	13.86%	17.45%	1.1
28.98	160	91.2%	83.6%	6.2	7.91%	8.44%	13.98%	17.51%	1.1
29.28	183	91.3%	83.6%	7.0	7.39%	7.96%	14.04%	17.34%	1.2
29.59	152	91.5%	83.8%	5.8	8.11%	8.64%	13.96%	17.59%	1.0
29.90	135	91.1%	83.7%	5.1	8.61%	9.10%	13.88%	17.76%	0.9
30.22	138	90.6%	83.7%	5.2	8.51%	9.01%	13.73%	17.60%	0.9
30.54	138	90.6%	84.1%	5.2	8.51%	9.01%	13.57%	17.48%	0.9
30.86	161	90.0%	83.8%	6.1	7.88%	8.42%	13.70%	17.28%	1.0

E_n (MeV)	Counts Peak	Corrections Efficiency Trans.		Cross- section σ (mb)	Uncertainties				Error bar (mb)
					Statistical		Syst.	Total	
					σ_{Peak}	$\sigma_{stat.total}$	σ_{Flux}	σ_{Total}	
31.20	139	90.1%	84.1%	5.1	8.48%	8.98%	13.91%	17.72%	0.9
31.53	164	89.9%	84.2%	6.0	7.81%	8.35%	14.03%	17.51%	1.1
31.88	136	89.5%	84.3%	5.0	8.57%	9.07%	14.12%	17.94%	0.9
32.22	111	89.7%	84.3%	4.0	9.49%	9.94%	14.49%	18.68%	0.7
32.58	132	89.1%	84.3%	4.7	8.70%	9.19%	15.02%	18.72%	0.9
32.94	112	89.0%	84.7%	3.9	9.45%	9.90%	15.24%	19.25%	0.8
33.30	113	88.7%	84.5%	3.9	9.41%	9.86%	15.30%	19.27%	0.8
33.68	99	88.2%	84.7%	3.4	10.05%	10.48%	15.55%	19.79%	0.7
34.06	97	87.7%	84.8%	3.3	10.15%	10.58%	16.04%	20.23%	0.7
34.44	111	87.8%	85.0%	3.7	9.49%	9.94%	16.59%	20.35%	0.8
34.83	125	87.8%	85.0%	4.1	8.94%	9.42%	17.24%	20.64%	0.8
35.23	118	87.4%	84.9%	3.8	9.21%	9.67%	17.68%	21.13%	0.8
35.64	100	86.6%	85.2%	3.3	10.00%	10.43%	17.72%	21.51%	0.7
36.05	72	86.3%	85.2%	2.3	11.79%	12.15%	17.73%	22.41%	0.5
36.47	90	85.4%	85.4%	2.9	10.54%	10.95%	17.97%	21.98%	0.6
36.90	64	85.6%	85.2%	2.0	12.50%	12.85%	18.49%	23.39%	0.5
37.34	69	85.3%	85.5%	2.1	12.04%	12.40%	19.32%	23.81%	0.5
37.78	54	85.0%	85.4%	1.6	13.61%	13.93%	19.86%	25.07%	0.4
38.23	50	84.3%	85.7%	1.5	14.14%	14.45%	19.97%	25.45%	0.4
38.70	67	84.0%	85.7%	2.0	12.22%	12.57%	19.84%	24.32%	0.5
39.16	63	84.0%	85.7%	1.9	12.6%	12.94%	19.37%	24.14%	0.5
39.64	50	83.2%	85.8%	1.5	14.14%	14.45%	19.24%	24.88%	0.4
40.13	53	82.6%	86.1%	1.6	13.74%	14.05%	19.47%	24.83%	0.4
40.62	30	82.9%	86.1%	0.9	18.26%	18.50%	19.83%	27.85%	0.2
41.13	43	82.0%	86.1%	1.3	15.25%	15.54%	20.27%	26.31%	0.3
41.65	44	81.4%	86.4%	1.3	15.08%	15.36%	20.35%	26.27%	0.3
42.17	40	80.7%	86.2%	1.2	15.81%	16.09%	20.37%	26.72%	0.3
42.71	49	79.7%	86.5%	1.4	14.29%	14.59%	20.76%	26.15%	0.4
43.25	26	79.2%	86.7%	0.7	19.61%	19.83%	21.17%	29.69%	0.2
43.81	21	78.8%	86.8%	0.6	21.82%	22.02%	21.51%	31.42%	0.2
44.38	27	78.6%	86.9%	0.8	19.25%	19.47%	21.82%	29.92%	0.2
44.95	19	78.0%	86.9%	0.5	22.94%	23.13%	22.11%	32.62%	0.2
45.55	26	77.5%	87.2%	0.7	19.61%	19.83%	22.08%	30.35%	0.2
46.15	29	76.6%	87.1%	0.8	18.57%	18.80%	21.99%	29.62%	0.2
46.76	18	76.3%	87.3%	0.5	23.57%	23.76%	22.27%	33.17%	0.2

E_n (MeV)	Counts Peak	Corrections Efficiency Trans.		Cross- section σ (mb)	Uncertainties				Error bar (mb)
					Statistical σ_{Peak} $\sigma_{stat.total}$		Syst. σ_{Flux}	Total σ_{Total}	
47.39	18	76.1%	87.4%	0.5	23.57%	23.76%	22.61%	33.40%	0.2
48.03	14	74.7%	87.6%	0.4	26.73%	26.89%	22.74%	35.78%	0.1
48.69	15	74.4%	87.7%	0.4	25.82%	25.99%	22.84%	35.17%	0.1
49.35	15	73.2%	87.6%	0.4	25.82%	25.99%	22.88%	35.20%	0.1
50.04	6	72.5%	87.9%	0.2	40.82%	40.93%	23.18%	47.46%	0.1
50.73	10	71.9%	88.2%	0.3	31.62%	31.76%	23.57%	40.06%	0.1
51.44	7	71.1%	88.2%	0.2	37.80%	37.91%	23.45%	45.02%	0.1
52.17	7	70.0%	88.3%	0.2	37.80%	37.91%	23.65%	45.13%	0.1
52.92	6	69.2%	88.5%	0.2	40.82%	40.93%	24.39%	48.07%	0.1
53.67	3	68.1%	88.6%	0.1	57.74%	57.81%	24.54%	63.12%	0
54.45	3	67.4%	88.6%	0.1	57.74%	57.81%	24.48%	63.10%	0.1
55.25	4	65.6%	88.7%	0.1	50.00%	50.09%	24.29%	56.02%	0.1

Table A.2: $^{12}\text{C}(n,p_0)^{12}\text{B}$ data table. The table contains the incident neutron energy (E_n), counts from $^{12}\text{C}(n,p_0)^{12}\text{B}$ (Counts: Peak), total counts in the fitting region (peak and background, Counts: Total), the charged particle detection efficiency correction for this channel (Corrections: Efficiency), and the simulated neutron transmission correction for the flux distribution (Corrections: Trans.)

E_n (MeV)	Counts Peak Total		Corrections Efficiency Trans.		E_n (MeV)	Counts Peak Total		Corrections Efficiency Trans.	
15.71	399	1268	98.4%	80.6%	20.60	201	369	83.2%	81.8%
16.02	485	1231	97.1%	80.2%	21.06	142	309	81.4%	81.9%
16.34	467	1054	96.4%	81.2%	21.55	133	313	79.4%	81.9%
16.67	327	776	96.9%	81.6%	22.05	127	329	76.6%	82.4%
17.01	360	657	95.2%	81.9%	22.57	137	301	73.4%	82.0%
17.36	505	880	94.8%	82.2%	23.11	147	314	70.7%	82.1%
17.72	443	761	93.6%	82.0%	23.66	189	351	68.1%	81.9%
18.09	315	505	92.2%	81.7%	24.24	163	338	65.3%	81.8%
18.48	314	485	90.9%	81.7%	24.84	128	314	59.9%	82.4%
18.87	246	426	89.0%	81.7%	25.47	78	268	57.2%	82.4%
19.28	275	481	89.2%	81.0%	26.11	89	259	53.2%	82.6%
19.71	220	377	86.0%	80.7%	26.79	66	224	49.5%	83.2%
20.14	235	401	84.4%	81.1%	27.49	59	245	45.0%	83.4%

Table A.3: $^{12}\text{C}(n,p_0)^{12}\text{B}$ uncertainty table. The table contains the cross section for this channel (Cross section: σ (mb)); the statistical uncertainties, broken into separate contributions from the counts from (n,p₀) at each energy (Uncertainty: Statistical: σ_{Peak}) and from the the background counts at each energy (Uncertainty: Statistical: σ_{Bkg}), and the total statistical uncertainties combining all statistical uncertainties (Uncertainty: Statistical: $\sigma_{stat.total}$); systematic uncertainties, which include the relative flux distribution uncertainty (Uncertainties: Systematic: σ_{Flux}), and the fit/integration uncertainties (Uncertainties: Systematic: σ_{Fit}). The total uncertainty, which includes both statistical and systematic uncertainties, is also included, both as a percentage and in terms of millibarns. Uncertainties that are constant for every data point were not included in the table for simplicity, but are included in the total uncertainty. These include: statistical uncertainty from the (n, α) counts at 14.1 MeV used for normalization (2.96%), and systematic uncertainties which include the charged particle detection efficiency correction uncertainty (4%), the incident neutron energy reconstruction uncertainty (0.49%), and the normalization uncertainty based on the weighted average uncertainty of previous data (4.87%).

E_n (MeV)	Cross- section σ (mb)	Uncertainties						Error bar (mb)
		Statistical			Systematic		Total	
		σ_{Peak}	σ_{Bkg}	$\sigma_{stat.total}$	σ_{Flux}	σ_{Fit}	σ_{Total}	
15.71	16.7	5.0%	8.9%	10.6%	5%	4.5%	13.16%	2.2
16.02	20.6	4.5%	7.2%	9.0%	5%	4.3%	12.02%	2.5
16.34	19.6	4.6%	7.0%	8.9%	5%	3.8%	11.68%	2.3
16.67	13.3	5.5%	8.5%	10.6%	5%	3.8%	12.67%	1.7
17.01	14.9	5.3%	7.1%	9.3%	5%	2.9%	11.50%	1.7
17.36	20.8	4.5%	5.9%	7.9%	5.3%	3.6%	11.12%	2.3
17.72	18.2	4.8%	6.2%	8.4%	6.9%	3.5%	12.16%	2.2
18.09	13.1	5.6%	7.1%	9.6%	7.5%	3.1%	12.86%	1.7
18.48	13.1	5.6%	7.0%	9.5%	7.2%	3.1%	12.61%	1.7
18.87	10.5	6.4%	8.4%	11.0%	6.4%	3.8%	13.21%	1.4
19.28	11.8	6.0%	8.0%	10.4%	5.5%	3.6%	12.49%	1.5
19.71	9.7	6.7%	8.8%	11.5%	5.5%	3.5%	12.99%	1.3
20.14	10.4	6.5%	8.5%	11.1%	5.4%	4.0%	12.89%	1.3
20.6	8.7	7.1%	9.6%	12.3%	5.8%	3.9%	13.73%	1.2
21.06	6.3	8.4%	12.4%	15.2%	5.2%	7.0%	16.68%	1.0
21.55	5.9	8.7%	13.3%	16.2%	5.9%	6.0%	17.22%	1.0
22.05	5.7	8.9%	14.3%	17.1%	6.1%	6.3%	18.15%	1.0
22.57	6.4	8.5%	12.7%	15.6%	5.9%	7.3%	17.23%	1.1
23.11	6.9	8.2%	12.0%	14.9%	6.7%	4.9%	16.19%	1.1
23.66	8.9	7.3%	9.9%	12.7%	8.3%	3.8%	15.15%	1.3

E_n	Cross-section	Uncertainties						Error bar
		Statistical			Systematic		Total	
(MeV)	σ (mb)	σ_{Peak}	σ_{Bkg}	$\sigma_{stat.total}$	σ_{Flux}	σ_{Fit}	σ_{Total}	(mb)
24.24	7.7	7.8%	11.3%	14.0%	9.3%	5.0%	16.93%	1.3
24.84	6.5	8.8%	13.8%	16.7%	9.3%	5.9%	18.97%	1.2
25.47	4.1	11.4%	21.1%	24.2%	9.8%	14.9%	28.50%	1.2
26.11	5.0	10.6%	18.0%	21.1%	10.1%	6.5%	22.74%	1.1
26.79	3.8	12.3%	22.5%	25.8%	11.1%	7.8%	27.20%	1.0
27.49	3.7	13.0%	26.5%	29.6%	12.4%	11.8%	32.27%	1.2

Table A.4: $^{12}\text{C}(n,p_1)^{12}\text{B}$ data table. The table contains the incident neutron energy (E_n), counts from $^{12}\text{C}(n,p_1)^{12}\text{B}$ (Counts: Peak), total counts in the fitting region (peak and background, Counts: Total), the charged particle detection efficiency correction for this channel (Corrections: Efficiency), and the simulated neutron transmission correction for the flux distribution (Corrections: Trans.)

E_n	Counts		Corrections		E_n	Counts		Corrections	
(MeV)	Peak	Total	Efficiency	Trans.	(MeV)	Peak	Total	Efficiency	Trans.
16.5	134	745	98.5%	81.5%	21.30	112	207	84.9%	82.1%
16.73	133	488	98.5%	81.7%	21.63	189	324	83.1%	82.2%
16.95	79	298	97.9%	81.8%	21.96	170	212	82.2%	82.3%
17.18	161	587	97.6%	82.2%	22.31	186	235	79.0%	82.1%
17.42	80	230	95.7%	82.4%	22.66	181	250	79.9%	82.2%
17.66	247	787	96.6%	82.0%	23.01	170	219	77.1%	82.0%
17.90	187	699	96.1%	81.8%	23.38	167	284	75.6%	82.1%
18.15	154	374	95.4%	81.7%	23.76	156	253	73.0%	81.9%
18.41	118	344	95.3%	81.6%	24.14	127	257	70.4%	82.0%
18.67	116	351	93.6%	81.7%	24.54	140	324	68.5%	82.1%
18.94	206	673	93.3%	81.7%	24.94	105	180	66.8%	82.2%
19.21	126	261	93.0%	81.1%	25.36	62	107	62.5%	82.5%
19.49	156	296	92.7%	80.9%	25.79	71	122	60.0%	82.6%
19.78	215	483	91.2%	80.9%	26.22	89	283	57.3%	82.6%
20.07	221	569	88.6%	81.1%	26.67	144	397	55.1%	83.1%
20.37	231	412	90.4%	81.5%	27.13	133	361	53.0%	83.3%
20.67	201	346	87.6%	81.9%	27.60	49	95	50.6%	83.4%
20.98	184	444	85.5%	81.9%					

Table A.5: $^{12}\text{C}(n,p_1)^{12}\text{B}$ uncertainty table. The table contains the cross section for this channel (Cross section: σ (mb)); the statistical uncertainties, broken into separate contributions from the counts from (n,p_1) at each energy (Uncertainty: Statistical: σ_{Peak}) and from the the background counts at each energy (Uncertainty: Statistical: σ_{Bkg}), and the total statistical uncertainties combining all statistical uncertainties (Uncertainty: Statistical: $\sigma_{stat.total}$); systematic uncertainties, which include the relative flux distribution uncertainty (Uncertainties: Systematic: σ_{Flux}), and the fit/integration uncertainties (Uncertainties: Systematic: σ_{Fit}). The total uncertainty, which includes both statistical and systematic uncertainties, is also included, both as a percentage and in terms of millibarns. Uncertainties that are constant for every data point were not included in the table for simplicity, but are included in the total uncertainty. These include: statistical uncertainty from the (n,α) counts at 14.1 MeV used for normalization (2.96%), and systematic uncertainties which include the charged particle detection efficiency correction uncertainty (4%), the incident neutron energy reconstruction uncertainty (0.49%), and the normalization uncertainty based on the weighted average uncertainty of previous data (4.87%).

E_n (MeV)	Cross-section σ (mb)	Uncertainties						Error bar (mb)
		Statistical			Systematic		Total	
		σ_{Peak}	σ_{Bkg}	$\sigma_{stat.total}$	σ_{Flux}	σ_{Fit}	σ_{Total}	
15.71	16.7	5.0%	8.9%	10.6%	5%	4.5%	13.16%	2.2
16.02	20.6	4.5%	7.2%	9.0%	5%	4.3%	12.02%	2.5
16.34	19.6	4.6%	7.0%	8.9%	5%	3.8%	11.68%	2.3
16.67	13.3	5.5%	8.5%	10.6%	5%	3.8%	12.67%	1.7
17.01	14.9	5.3%	7.1%	9.3%	5%	2.9%	11.00%	1.7
17.36	20.8	4.5%	5.9%	7.9%	5.3%	3.6%	11.12%	2.3
17.72	18.2	4.8%	6.2%	8.4%	6.9%	3.5%	12.16%	2.2
18.09	13.1	5.6%	7.1%	9.6%	7.5%	3.1%	12.86%	1.7
18.48	13.1	5.6%	7.0%	9.5%	7.2%	3.1%	12.61%	1.7
18.87	10.5	6.4%	8.4%	11.0%	6.4%	3.8%	13.21%	1.4
19.28	11.8	6.0%	8.0%	10.4%	5.5%	3.6%	12.49%	1.5
19.71	9.7	6.7%	8.8%	11.5%	5.5%	3.5%	12.99%	1.3
20.14	10.4	6.5%	8.5%	11.1%	5.4%	4.0%	12.89%	1.3
20.60	8.7	7.1%	9.6%	12.3%	5.8%	3.9%	13.73%	1.2
21.06	6.3	8.4%	12.4%	15.2%	5.2%	7.0%	16.68%	1.0
21.55	5.9	8.7%	13.3%	16.2%	5.9%	6.0%	17.22%	1.0
22.05	5.7	8.9%	14.3%	17.1%	6.1%	6.3%	18.15%	1.0
22.57	6.4	8.5%	12.7%	15.6%	5.9%	7.3%	17.23%	1.1
23.11	6.9	8.2%	12.0%	14.9%	6.7%	4.9%	16.19%	1.1
23.66	8.9	7.3%	9.9%	12.7%	8.3%	3.8%	15.15%	1.3

E_n (MeV)	Cross-section σ (mb)	Uncertainties						Error bar (mb)
		Statistical			Systematic		Total	
		σ_{Peak}	σ_{Bkg}	$\sigma_{stat.total}$	σ_{Flux}	σ_{Fit}	σ_{Total}	
24.24	7.7	7.8%	11.3%	14.0%	9.3%	5.0%	16.93%	1.3
24.84	6.5	8.8%	13.8%	16.7%	9.3%	5.9%	18.97%	1.2
25.47	4.1	11.4%	21.1%	24.2%	9.8%	14.9%	28.50%	1.2
26.11	5.0	10.6%	18.0%	21.1%	10.1%	6.5%	22.74%	1.1
26.79	3.8	12.3%	22.5%	25.8%	11.1%	7.8%	27.20%	1.0
27.49	3.7	13.0%	26.5%	29.6%	12.4%	11.8%	32.27%	1.2

Table A.6: $^{12}\text{C}(n,d_0)^{11}\text{B}$ data table. The table contains the incident neutron energy (E_n), counts from $^{12}\text{C}(n,d_0)^{11}\text{B}$ (Counts: Peak), total counts in the fitting region (peak and background, Counts: Total), the charged particle detection efficiency correction for this channel (Corrections: Efficiency), and the simulated neutron transmission correction for the flux distribution (Corrections: Trans.)

E_n	Counts		Corrections		E_n	Counts		Corrections	
(MeV)	Peak	Total	Efficiency	Trans.	(MeV)	Peak	Total	Efficiency	Trans.
15.87	379	753	99.8%	80.5%	25.36	445	597	84.1%	82.5%
16.07	596	966	100%	80.3%	25.79	481	623	83.3%	82.6%
16.29	683	1067	99.8%	81.0%	26.22	407	596	81.8%	82.6%
16.50	699	1119	99.9%	81.5%	26.67	332	521	79.3%	83.1%
16.73	675	1077	99.9%	81.7%	27.13	285	463	77.8%	83.3%
16.95	706	1122	99.9%	81.8%	27.60	350	499	76.7%	83.4%
17.18	723	1043	99.8%	82.2%	28.09	303	471	75.6%	83.3%
17.42	691	1025	99.6%	82.4%	28.59	305	458	73.1%	83.6%
17.66	803	1134	99.5%	82.0%	29.10	299	448	70.9%	83.6%
17.90	739	1073	99.2%	81.8%	29.62	265	426	70.0%	83.7%
18.15	765	1063	99.0%	81.7%	30.16	306	441	66.7%	83.7%
18.41	827	1113	98.8%	81.6%	30.72	289	464	63.5%	84.0%
18.67	972	1245	98.5%	81.7%	31.29	324	517	61.5%	84.2%
18.94	871	1101	98.0%	81.7%	31.88	242	433	57.9%	84.3%
19.21	774	971	97.8%	81.1%	32.48	244	417	55.5%	84.3%
19.49	697	891	97.2%	80.9%	33.10	190	313	53.5%	84.6%
19.78	703	880	96.7%	80.9%	33.75	229	409	50.8%	84.7%
20.07	697	861	96.4%	81.1%	34.41	202	393	48.4%	85.0%
20.37	693	845	96.0%	81.5%	35.08	198	365	46.8%	84.9%
20.67	652	806	95.2%	81.9%	35.79	170	300	45.5%	85.2%
20.98	576	709	95.0%	81.9%	36.51	169	318	43.5%	85.4%
21.30	533	685	93.9%	82.1%	37.25	170	312	41.8%	85.4%
21.63	565	691	93.0%	82.2%	38.02	143	296	40.2%	85.5%
21.96	574	711	92.3%	82.3%	38.81	84	254	39.9%	85.7%
22.31	571	728	92.0%	82.1%	39.63	66	149	38.2%	85.8%
22.66	650	827	91.3%	82.2%	40.47	91	278	36.7%	86.1%
23.01	612	775	90.9%	82.0%	41.35	78	206	35.1%	86.2%
23.38	513	706	89.8%	82.1%	42.25	80	200	34.1%	86.2%
23.76	498	692	87.9%	81.9%	43.18	72	226	33.1%	86.7%
24.14	448	617	87.5%	82.0%	44.14	62	163	30.8%	86.8%
24.54	411	583	86.5%	82.1%	45.14	87	195	30.0%	87.0%

24.94	415	592	85.0%	82.2%					
-------	-----	-----	-------	-------	--	--	--	--	--

Table A.7: $^{12}\text{C}(n,d_0)^{11}\text{B}$ uncertainty table. The table contains the cross section for this channel (Cross section: σ (mb)); the statistical uncertainties, broken into separate contributions from the counts from (n,d₀) at each energy (Uncertainty: Statistical: σ_{Peak}) and from the the background counts at each energy (Uncertainty: Statistical: σ_{Bkg}), and the total statistical uncertainties combining all statistical uncertainties (Uncertainty: Statistical: $\sigma_{stat.total}$); systematic uncertainties, which include the relative flux distribution uncertainty (Uncertainties: Systematic: σ_{Flux}), and the fit/integration uncertainties (Uncertainties: Systematic: σ_{Fit}). The total uncertainty, which includes both statistical and systematic uncertainties, is also included, both as a percentage and in terms of millibarns. Uncertainties that are constant for every data point were not included in the table for simplicity, but are included in the total uncertainty. These include: statistical uncertainty from the (n, α) counts at 14.1 MeV used for normalization (2.96%), and systematic uncertainties which include the charged particle detection efficiency correction uncertainty (4%), the incident neutron energy reconstruction uncertainty (0.49%), and the normalization uncertainty based on the weighted average uncertainty of previous data (4.87%).

E_n (MeV)	Cross-section σ (mb)	Uncertainties						Error bar (mb)
		Statistical			Systematic		Total	
		σ_{Peak}	σ_{Bkg}	$\sigma_{stat.total}$	σ_{Flux}	σ_{Fit}	σ_{Total}	
15.87	23.6	5.1%	5.1%	7.8%	5%	4.1%	11.99%	2.8
16.07	37.0	4.1%	3.2%	6.0%	5%	2.2%	10.34%	3.8
16.29	41.9	3.8%	2.9%	5.6%	5%	2.4%	10.16%	4.3
16.50	42.1	3.8%	2.9%	5.6%	5%	2.4%	10.17%	4.3
16.73	40.1	3.8%	3.0%	5.7%	5%	2.2%	10.17%	4.1
16.95	41.9	3.8%	2.9%	5.6%	5%	2.3%	10.13%	4.2
17.18	43.1	3.7%	2.5%	5.4%	5%	1.9%	9.93%	4.3
17.42	40.8	3.8%	2.6%	5.5%	5.6%	2.0%	10.31%	4.2
17.66	47.2	3.5%	2.3%	5.1%	6.7%	2.1%	10.80%	5.1
17.90	43.4	3.7%	2.5%	5.3%	7.6%	2.0%	11.43%	5.0
18.15	44.7	3.6%	2.3%	5.2%	7.5%	2.0%	11.32%	5.1
18.41	48.1	3.5%	2.0%	5.0%	7.3%	1.8%	11.06%	5.3
18.67	56.5	3.2%	1.7%	4.7%	6.8%	1.4%	10.56%	6.0
18.94	50.9	3.4%	1.7%	4.8%	6.3%	1.8%	10.33%	5.3
19.21	45.8	3.6%	1.8%	5.0%	5.6%	1.8%	10.05%	4.6
19.49	41.3	3.8%	2.0%	5.2%	5.5%	1.7%	10.03%	4.1
19.78	41.5	3.8%	1.9%	5.2%	5.5%	1.9%	10.06%	4.2

E_n (MeV)	Cross-section σ (mb)	Uncertainties						Error bar (mb)
		Statistical			Systematic		Total	
		σ_{Peak}	σ_{Bkg}	$\sigma_{stat.total}$	σ_{Flux}	σ_{Fit}	σ_{Total}	
20.07	40.8	3.8%	1.8%	5.1%	5.4%	2.0%	10.02%	4.1
20.37	40.1	3.8%	1.8%	5.1%	5.5%	1.8%	10.04%	4.0
20.67	37.2	3.9%	1.9%	5.3%	5.8%	2.0%	10.33%	3.8
20.98	33.0	4.2%	2.0%	5.5%	5.3%	2.2%	10.19%	3.4
21.30	30.5	4.3%	2.3%	5.7%	5.4%	2.2%	10.39%	3.2
21.63	32.0	4.2%	2.0%	5.5%	6.0%	2.1%	10.56%	3.4
21.96	32.3	4.2%	2.0%	5.5%	6.1%	2.3%	10.68%	3.5
22.31	32.1	4.2%	2.2%	5.6%	6.0%	2.2%	10.65%	3.4
22.66	36.6	3.9%	2.0%	5.3%	6.0%	2.1%	10.47%	3.8
23.01	34.0	4.0%	2.1%	5.4%	6.5%	2.2%	10.86%	3.7
23.38	28.1	4.4%	2.7%	6.0%	7.4%	3.0%	11.87%	3.3
23.76	27.2	4.5%	2.8%	6.1%	8.5%	3.1%	12.60%	3.4
24.14	24.1	4.7%	2.9%	6.3%	9.1%	3.3%	13.20%	3.2
24.54	22.1	4.9%	3.2%	6.6%	9.3%	3.4%	13.48%	3.0
24.94	22.5	4.9%	3.2%	6.6%	9.3%	3.8%	13.61%	3.1
25.36	24.0	4.7%	2.8%	6.2%	9.7%	2.7%	13.46%	3.2
25.79	26.0	4.6%	2.5%	6.0%	10.0%	2.9%	13.57%	3.5
26.22	22.2	5.0%	3.4%	6.7%	10.2%	3.7%	14.24%	3.2
26.67	18.3	5.5%	4.1%	7.5%	10.8%	3.7%	15.03%	2.7
27.13	15.4	5.9%	4.7%	8.1%	12.3%	5.3%	16.94%	2.6
27.60	19.2	5.3%	3.5%	7.0%	12.3%	3.0%	15.81%	3.0
28.09	16.9	5.7%	4.3%	7.7%	12.5%	5.7%	17.06%	2.9
28.59	17.0	5.7%	4.0%	7.6%	13.8%	4.4%	17.55%	3.0
29.10	16.8	5.8%	4.1%	7.7%	14.0%	4.9%	17.89%	3.0
29.62	14.9	6.1%	4.8%	8.3%	14.0%	3.2%	17.77%	2.6
30.16	17.9	5.7%	3.8%	7.5%	13.8%	3.3%	17.24%	3.1
30.72	17.5	5.9%	4.6%	8.0%	13.6%	3.8%	17.5%	3.1
31.29	19.8	5.6%	4.3%	7.6%	13.9%	3.0%	17.4%	3.4
31.88	15.4	6.4%	5.7%	9.1%	14.1%	3.9%	18.41%	2.8
32.48	15.8	6.4%	5.4%	8.9%	14.9%	3.8%	18.85%	3.0
33.10	12.5	7.3%	5.8%	9.8%	15.3%	4.5%	19.74%	2.5
33.75	15.5	6.6%	5.8%	9.3%	15.6%	3.9%	19.67%	3.1
34.41	13.9	7.0%	6.9%	10.3%	16.5%	5.7%	21.27%	3.0
35.08	13.7	7.1%	6.5%	10.1%	17.5%	4.5%	21.68%	3.0
35.79	11.9	7.7%	6.7%	10.6%	17.7%	7.1%	22.77%	2.7

E_n (MeV)	Cross-section σ (mb)	Uncertainties						Error bar (mb)
		Statistical			Systematic		Total	
		σ_{Peak}	σ_{Bkg}	$\sigma_{stat.total}$	σ_{Flux}	σ_{Fit}	σ_{Total}	
36.51	12.1	7.7%	7.2%	10.9%	18.0%	5.1%	22.6%	2.7
37.25	12.1	7.7%	7.0%	10.8%	19.2%	6.3%	23.78%	2.9
38.02	10.3	8.4%	8.6%	12.4%	19.9%	10.0%	26.29%	2.7
38.81	6.0	10.9%	15.5%	19.2%	19.7%	9.2%	29.71%	1.8
39.63	4.9	12.3%	13.8%	18.8%	19.2%	12.8%	30.46%	1.5
40.47	6.8	10.5%	15.1%	18.7%	19.7%	9.1%	29.34%	2.0
41.35	6.0	11.3%	14.4%	18.5%	20.3%	6.7%	29.01%	1.7
42.25	6.2	11.2%	13.6%	17.9%	20.4%	14.2%	31.29%	2.0
43.18	5.6	11.8%	17.1%	21.0%	21.1%	7.2%	31.3%	1.8
44.14	5.1	12.7%	16.3%	20.8%	21.7%	11.6%	32.87%	1.7
45.14	7.2	10.7%	11.9%	16.3%	22.1%	9.2%	29.64%	2.1

Appendix B

digiTES configuration file

Abbreviated version of the digiTES configuration file that controlled the data acquisition for the experiment. The diamond detector signals are in Board 1, Channel 1 for the upstream detector and Board 1, Channel 3 for the downstream detector. Parameters for each detector were adjusted to minimize noise and maximize neutron events.

```
# Config File Template

# Board Connection Parameters:

[BOARD 0]  Open PCI 0 0 0          # direct optical link
[BOARD 1]  Open PCI 0 1 0          # direct optical link
[BOARD 2]  Open PCI 0 2 0          # direct optical link

# Acquisition Modes
AcquisitionMode          LIST          # options: LIST (timestamp,
energy, psd), MIXED (list + waveform), OFF_LINE (read data from file),
EMULATOR_LIST, EMULATOR_MIXED
EventBuildMode           NONE          # options: NONE (no channel
correlation), CHREF_AND_ANYOTHER (one ref. ch. in coinc. with at least
another ch.), CLOVER N M (Majority of M ch over N within time correl. win
.)
WaveformProcessor        0            # Apply simple DPP algorithms
in the software (using waveforms); 0=disabled, 3=calculate charge and
tstamp
RecordLength             500          # num of samples in the waveform;
this variable affects all channels
PreTrigger               40           # num of point before trigger
EventBuffering           1            # num of events in each memory
buffer (aggregate); 0=automatic. Use 1 for low rate (< 10 Hz)

# Sync and Trigger
FPIOtype                 NIM          # NIM or TTL (applies to the 3
LEMO connectors on the front panel)
StartMode                 TRGIN_1SW    # options: INDEP_SW,
```

```

    SYNCIN_1ST_SW, SYNCIN_1ST_HW, TRGIN_1ST_SW, TRGIN_1ST_HW
SyncinMode          TSTAMP_RESET      # options: DISABLED,
    TSTAMP_RESET, RUN_CTRL
TrginMode           DISABLED          # options: DISABLED,
    COMMON_TRG, COMMON_TRG_START, VETO, GATE, COINC
VetoWindow          0                 # 0 = as long as veto signal,
    otherwise width in ns
TrgoutMode          CHANNEL_TRIGGERS  # options: DISABLED,
    CHANNEL_TRIGGERS, SYNC_OUT, SQR_WAVE_1KHZ, PULSES_1KHZ, SQR_WAVE_10KHZ,
    PULSES_10KHZ, CLOCK
TrgoutMask          FF                # enable mask of the channels
    participating to generate TRGOUT

# Coincidence Logic in hardware
CoincMode           DISABLED          # options: DISABLED, MAJORITY,
    MINORITY, PAIRED_AND, PAIRED_OR, ANTI_PAIRED_AND, COMMON_REFCH,
    ANTI_COMMON_REFCH, CH0_TO_ALL, AND_ALL, OR_ALL
MajorityLevel       3                 # Number of fired channels for
    MAJORITY/MINORITY
CoincWindow         100               # Coinc window (default unit =
    ns)

# Input Settings
EnableInput         1                 # channels all enabled by
    default (can be individually disabled in [CHANNEL n] sections)
PulsePolarity       NEGATIVE          # options: NEGATIVE, POSITIVE
BaselineDCoffset    10                # baseline position in percent
    of full scale
ZeroVoltLevel       14800             # for non DPP firmware (StdFw)
    , the baseline is not calculated by the FPGA and must be set by the user
    with this param. Ignored in DPP firmware
InputDynamicRange   0                 # for x730: 0=2Vpp, 1=0.5Vpp

# Discriminator
DiscrMode           CFD               # Discriminator type: DISABLED
    , LED, CFD (for PSD), RCCR2_PHA, CFD_PHA, LED_PHA (for PHA)
TriggerThreshold    10                # threshold in ADC channels
TrgHoldOff          32                # Trigger hold off (minumum
    time after a trigger for a new trigger to be accepted)
TTFsmoothing        4                 # smoothing: 0=disabled, 1, 2,
    3, 4 => 2, 4, 8, 16 samples
TTFdelay            200               # for PHA only: typically
    TTDdealy = rising edge of the pulses (in ns)

```

```

CFDdelay          4          # CFD delay in ns
CFDfraction       0          # CFD fraction: 0=25%, 1=50%,
    2=75%, 3=100%

# Charge Integration (DPP-PSD/CI)
GateWidth        60          # gate width (long gate for the
    PSD). (default unit = ns)
ShortGateWidth   20          # short gate width (default
    unit = ns)
PreGate          78          # was 150 portion of the gate
    before the trigger (default unit = ns)
PileUpMode       0          # 0=DISABLED, 1=ENABLED (
    discard pile-up events)
PurGap           4000        # threshold for the pile-up
    identification
NSBaseline       2          # 0=fixed, 1, 2, 3, 4 options
    depending on the board type (see manual)
FixedBaseline    0          # imposed baseline (when
    NSBaseline=0)
ChargeLLD        0          # suppress events with total
    charge < ChargeLLD (0=disabled)
EnablePedestal   0          # add a fixed offset = 1024 (
    pedestal) to the integrated charge in order to see small negative charges

# Energy Spectra
EHnbin           1K          # num of channels in energy
    spectrum (256, 512, 1K, 2K, 4K, 8K, 16K, 32K)
EnergyCoarseGain 2          # energy coarse gain (1/16, 1/8,
    1/4, 1/2, 1, 2, 4, 8, 16, 32). Note: fractions can be expressed either as
    text (1/2) or float (0.5)
EnergyFineGain   1.0000     # energy fine gain
EnergyLCut       1000        # lower energy cut
EnergyUCut       1500        # upper energy cut
EnableEnergyFilter 0        # enable energy cut in the SW
    (energy gating)
AddBackFullScale 10000.0    # Full scale of the Add Back
    energy spectrum (in keV)
ECalibration     0 1.0 0 0   # energy calibration coeff. c0
    , c1, c2, c3 (c2 and c3 optional). E(keV) = c0 + c1*E(ch) + c2*(E(ch)^2) +
    c3*(E(ch)^3)

# Timing Spectra
THmin            -50        # min value for the time

```

```

    spectrum
THmax          50          # max value for the time
    spectrum
THnbin         1K          # num of channels in time
    spectrum (256, 512, 1K, 2K, 4K, 8K, 16K, 32K)
TspectrumMode  START_STOP  # Timing Spectrum Mode:
    START_STOP (time from a common ref channel), INTERVALS (time between
    consecutive events)
TOFstartChannel 0          # Tref (start): channel number
TOFstartBoard  0          # Tref (start): board number
TstampOffset   0          # fixed value added to the
    time stamp read from the board
TimeCorrelWindow 100      # window for the timing
    correlation filter (coincidences in the SW)

# PSD Spectra
PsdLCut        0.00       # lower PSD cut
PsdUCut        1.00       # upper PSD cut
EnablePSDFilter 0         # enable PSD cut
ScatterPlotMode PSD_HORIZONTAL # PSD_HORIZONTAL, PSD_DIAGONAL
    or E_VS_DELTAE

# MCS Spectra (Counting)
MCSHnbin       1K         # number of channels in the
    MCS spectrum
DwellTime      100000     # time interval (in us) for
    the counting (each interval generates a channel in the MCS spectrum)

[BOARD 1]

[CHANNEL 0]
EnableInput 1 # disable channel 1 only (the others are enabled by default
)

[CHANNEL 1]
EnableInput 1 # disable channel 1 only (the others are enabled by default)
PulsePolarity    POSITIVE
PreGate          240      # was 150 portion of the
    gate before the trigger (default unit = ns)
GateWidth        500
ShortGateWidth   200
TriggerThreshold 20
PreTrigger       56

```

```

DiscrMode          CFD          # Discriminator type: DISABLED
, LED, CFD (for PSD), RCCR2_PHA, CFD_PHA, LED_PHA (for PHA)
TrgHoldOff         544          # Trigger hold off (minumum
time after a trigger for a new trigger to be accepted)
TTFsmoothing       0           # smoothing: 0=disabled, 1, 2,
3, 4 => 2, 4, 8, 16 samples
TTFdelay           200         # for PHA only: typically
TTDdealy = rising edge of the pulses (in ns)
CFDdelay           80          # CFD delay in ns
CFDfraction        1           # CFD fraction: 0=25%, 1=50%,
2=75%, 3=100%
InputDynamicRange  0           # for x730: 0=2Vpp, 1=0.5Vpp
EnergyCoarseGain   2           # energy coarse gain (1/16, 1/8,
1/4, 1/2, 1, 2, 4, 8, 16, 32). Note: fractions can be expressed either as
text (1/2) or float (0.5)
#EHnbin            4K          # num of channels in energy
spectrum (256, 512, 1K, 2K, 4K, 8K, 16K, 32K)

```

[CHANNEL 2]

```

EnableInput 1      # disable channel 1 only (the others are enabled by default)

```

[CHANNEL 3]

```

EnableInput 1      # disable channel 1 only (the others are enabled by default
)

```

```

PulsePolarity      POSITIVE
PreGate            70          # was 150 portion of the gate
before the trigger (default unit = ns)
GateWidth          100
ShortGateWidth     36
TriggerThreshold   26
PreTrigger         56
DiscrMode          CFD          # Discriminator type: DISABLED
, LED, CFD (for PSD), RCCR2_PHA, CFD_PHA, LED_PHA (for PHA)
TrgHoldOff         544          # Trigger hold off (minumum
time after a trigger for a new trigger to be accepted)
TTFsmoothing       2           # smoothing: 0=disabled, 1, 2,
3, 4 => 2, 4, 8, 16 samples
TTFdelay           200         # for PHA only: typically
TTDdealy = rising edge of the pulses (in ns)
CFDdelay           4           # CFD delay in ns
CFDfraction        0           # CFD fraction: 0=25%, 1=50%,
2=75%, 3=100%
InputDynamicRange  0           # for x730: 0=2Vpp, 1=0.5Vpp

```

```
EnergyCoarseGain      2          # energy coarse gain (1/16, 1/8,  
1/4, 1/2, 1, 2, 4, 8, 16, 32). Note: fractions can be expressed either as  
text (1/2) or float (0.5)
```